Cellular Crosstalk in Pancreas Cancer Microenvironment: Mechanisms of Tumor Immune Evasion and Immune Suppression

by

Padma Kadiyala

A dissertation submitted in partial fulfillment
of the requirements for the degree of
Doctor of Philosophy
(Immunology)
in the University of Michigan
2024

Doctoral Committee:

Professor Marina Pasca Di Magliano, Chair
Assistant Professor Filip Bednar
Assistant Professor Eileen Carpenter
Professor Kathleen Collins
Assistant Professor Kyoung Lee

Padma Kadiyala

pkadiyal@umich.edu

ORCID iD: 0000-0002-3273-9905

© Padma Kadiyala 2024

Table of Contents

List of Tables iv

List of Figures v

Abstract vii

Chapter 1 Introduction 1

1.1 Pancreas Cancer Overview 1

1.2 Pancreas Cancer Inniation and Progression 1

1.3 Pancreas Cancer Tumor Microenvironment 2

1.4 Transcription Characterization of Pancreas Cancer Microenvironment 6

1.5 JAK/STAT3 Signaling Regulates Tumorigenesis 7

1.6 Scope of the Dissertation 7

Chapter 2 Analysis of Donor Pancreata Defines the Transcriptomic Signature and Microenvironment of Early Neoplastic Lesions 9

2.1 Abstract 9

2.2 Introduction 9

2.3 Results 11

2.4 Discussion 22

2.5 Methods 26

2.6 Acknodwledgements and Author Contributions 32

2.7 Figures 34

2.8 Tables 70

Chapter 3 JAK/STAT3 Signaling in Myeloid Cells Drives Immunoregulation in Pancreatic Cancer 72

3.1 Abstract 72
3.2 Introduction 73
3.3 Results 74
3.4 Discussion 77
3.5 Methods 78
3.6 Acknwledgemets and Author Contributions 80
3.7 Figures 81
Chapter 4 Crosstalk between Cancer Associated Fibroblasts and T helper 2 cells in Pancreas Cancer 89
4.1 Abstract 89
4.2 Introduction 90
4.3 Results 91
4.4 Discussion 94
4.5 Methods 95
4.6 Acknwledgemets and Author Contributions 98
4.7 Figures 99
Chapter 5 Conclusions and Future Directions 107
5.1 Summary 107
5.2 Major Findings and Implications from Chapter 2 107
5.3 Major Findings and Implications from Chapter 3 108
5.4 Major Findings and Implications from Chapter 4 110
5.5 Final Remarks 112
5.6 Figures 113
Bibliography 119

List of Tables

Table 1: Demographics and clinical data for donor samples 70

Table 2: Kras mutational profiling on select donor samples 70

Table 3: Multiplex IF antibodies 71

Table 4: Immunofluorescence Primary, Secondary Antibodies Used for co-IF and RNA FISH probes 71

List of Figures

Figure 1.1: Scheme depicting progression of PanIN to PDAC 2

Figure 1.2: The tumor microenvironment in PDAC 3

Figure 1.3: Workflow of Single-Cell RNA-sequencing PDAC tissue 6

Figure 2.1: The adult human pancreas harbors frequent PanIN lesions 34

Figure 2.2: Distinct Lesions in adult Pancreas 36

Figure 2.3: PanIN lesions in healthy pancreata is surrounded by a unique microenvironment 37

Figure 2.4: Multiplex immunohistochemistry staining of donor pancreata 39

Figure 2.5: Healthy pancreata contain several non-epithelial populations, including myeloid, lymphocyte, fibroblast, and endothelial cells 41

Figure 2.6: Cell linage markers and genes being expressed by myeloid cells 43

Figure 2.7: Markers and genes being expressed by lymphocytes 44

Figure 2.8: Markers and genes being expressed by Endothelial, Fibroblast and pericyte populations 45

Figure 2.9: Comparison of the microenvironment in healthy pancreata and pancreatic tumors reveals distinct stromal features 47

Figure 2.10: Cell abundance in Healthy, Adjacent Normal, and Tumor Samples 49

Figure 2.11: Myeloid and fibroblast populations from tumor-bearing pancreata display distinct transcriptomic signatures compared to their non-tumor counterparts 51

Figure 2.12: Myeloid and Fibroblast cell abundance in Healthy, Adjacent Normal, and Tumor Samples 53

Figure 2.13: Activated pathways in T cells from Healthy and Tumor samples 55

Figure 2.14: Distinct Epithelial cells in Healthy, Adjacent normal, and Tumor samples 57

Figure 2.15: Spatial transcriptomics reveals a unique epithelial gene signature of PanIN lesions which aligns closely with tumor epithelium 59

Figure 2.16: Classification of the epithelial cells 61

Figure 2.17: Immunofluorescence staining of Epithelial markers-Donor 24 63

Figure 2.18: Immunofluorescence staining of Epithelial markers-Donor 8 64

Figure 2.19: Immunofluorescence staining of Epithelial markers-Donor 23 65

Figure 2.20: Immunofluorescence staining of Epithelial markers-Donor 5 67

Figure 2.21: Claudin 18, MUC5AC/B, and AQP1/3 distinguish normal Ducts, ADM, and PanIN in healthy pancreas 68

Figure 3.1: STAT3 activation in myeloid cells is required for tumorigenesis.....81

Figure 3.2: STAT3 signaling in myeloid cells regulates macrophage immunosuppressive phenotype 83

Figure 3.3: Single cell RNA-sequencing Data of KFC and KFCS mice 85

Figure 3.4: Loss of STAT3 signaling in myeloid cells results in fibroblast reprograming 86

Figure 3.5: Loss of STAT3 signaling in myeloid reduces expression of T cell exhaustion markers in CD8 T cells 88

Figure 4.1: CD8 T cells in Treg depleted mice have an exhausted transcriptional signature 99

Figure 4.2: Single cell RNA-sequencing data of KC and KC;Foxp3^{DTR} mice 100

Figure 4.3: Depletion of Tregs results in increase in Th2 T cells and fibroblast reprogramming.....101

Figure 4.4: CD4 T cells from Treg depleted tumor microenvironment reprogram pancreatic fibroblasts.....103

Figure 4.5: Type 2 cytokines reprogram pancreatic fibroblasts.....105

Figure 4.6: CD4 T cells and fibroblast crosstalk schematic.....106

Figure 5.1: Fibroblast-Orgnaoid Co-culture system recapitulates features of primary tumor.....113

Figure 5.2: STAT3 activation in fibroblasts is required for lesion formation.....115

Figure 5.3: Fibroblasts express high *Ccl8* when co-cultured with Th2 T cells 117

Figure 5.4: Levels of type 2 cytokines in PDAC patient serum.....118

Abstract

Pancreatic ductal adenocarcinoma (PDAC) is a dismal disease with a 5-year survival rate of 12.5%. The advanced stage of disease at the time of diagnosis limits the effectiveness of treatment modalities. Although immune checkpoint blockade therapy has provided robust and durable clinical benefit in multiple solid tumors, it has failed to improve PDAC patients' survival. This is partially due to the immunosuppressive effects of the PDAC tumor microenvironment (TME), which is established at the earliest stages of tumorigenesis alongside the formation of the PDAC precursor lesions, pancreatic intraepithelial neoplasia (PanIN). A hallmark feature of PDAC is the presence of an inflammatory stroma comprised of immune cells and fibroblasts, but the mechanisms that regulate cellular reprogramming and crosstalk between fibroblasts and immune cells during the onset and progression of tumorigenesis are not fully understood.

The mechanisms underlying the onset and pathogenesis of neoplastic lesions in humans have remained elusive due to the inability to study tissue from pathologically normal pancreata. Due to its abundance of digestive enzymes, the pancreas degrades shortly after death, making autopsy samples unsuitable for research. Through a collaboration with the Gift of Life Organ and Tissue donation program, we performed histological and transcriptomic analysis on normal pancreata declined for transplant. Surprisingly, our initial analysis of a group of 30 pancreata revealed that the majority of organs, irrespective of donor age, contained neoplastic lesions. Interestingly, the epithelial cells lining the lesions were transcriptionally similar to pancreatic cancer and presented with KRAS mutations, the key oncogenic driver of pancreatic cancer. However, we noted distinct transcriptomic signature of fibroblasts and macrophages surrounding healthy pancreata relative to tumor. These results indicate that the microenvironment surrounding the lesions is distinct from that of tumors.

To study cellular reprogramming in the early stages of disease we utilized genetically engineered mouse models that mimic the progression of human disease. Building on

previous work from our lab, we discovered that activation of the Signal and Transducer of Activation 3 (STAT3) transcription factor mediates myeloid cell reprogramming in pancreatic cancer. While the role of the JAK/STAT3 pathway in tumor epithelial cells has been well characterized, its role in myeloid cells is less well understood. We noted that loss of STAT3 activity in myeloid cells reversed tumor associated macrophage polarization to an immune stimulatory phenotype, indicating a cell specific signaling role in the TME. Similarly, our previous work has demonstrated that depletion of immunosuppressive regulatory T cells (Tregs) from a mouse model of PDAC reprograms fibroblasts in the TME to an inflammatory phenotype through upregulation of cytokines that contribute to the recruitment of immunosuppressive myeloid cells and tumor progression. In the current study, single-cell RNA sequencing analysis of pancreatic neoplastic lesions upon Treg depletion revealed that the majority of infiltrating CD4 T cells were Gata3+ T helper 2 (Th2) cells. We explored whether Th2 cells impact the biology of fibroblasts in the TME. Co-culturing of normal pancreatic fibroblasts with CD4 T cells derived from the PDAC TME of Treg depleted mice or Th2 T cells led to an upregulation of myeloid cell recruiting cytokines, consistent with in vivo results. These data suggest that pancreatic fibroblasts respond to Th2 cytokines and that Tregs are key regulators of type-2 immune responses in the pancreas.

This work has identified that crosstalk between myeloid cells, Tregs, Th2 cells, and fibroblasts promotes pancreatic tumorigenesis and that targeting the JAK/STAT3 pathway in myeloid cells could be clinically promising.

Chapter 1 Introduction

Portions of this chapter have been published.

Kadiyala, P., Elhossiny, A. M., & Carpenter, E. S. (2022). Using Single Cell Transcriptomics to Elucidate the Myeloid Compartment in Pancreatic Cancer. *Frontiers in oncology*, *12*, 881871. PubMed PMID: 35664793

1.1 Pancreas Cancer Overview

Pancreatic ductal adenocarcinoma (PDAC) is a deadly malignancy with a five-year survival rate of 12.5% (1). With no reliable early detection approaches currently available, patients often present with locally advanced or metastatic disease. Current standard of care for patients includes FOLFIRINOX (combination of 5-fluorouracil, irinotecan, leucovorin and oxaliplatin) or gemcitabine combined with Abraxane (albumin bound paclitaxel particles) (1-3). Less than 20% of cases qualify for surgical resection, which often does not result in cure (1-3). Furthermore, clinical trial efforts for both neoadjuvant and adjuvant interventions have shown only slight survival improvement relative to palliative care. Currently, PDAC is the third leading cause of cancer deaths in the United States, and with over 60,000 new cases each year, it is projected to become the second leading cause of cancer deaths by 2030 (1-3). Given the limited therapeutic options currently available to treat the disease, there is a paramount need to characterize PDAC biology to develop novel treatment strategies.

1.2 Pancreas Cancer Initiation and Progression

Higher incidence of PDAC has been observed in the aging population, which may be a function of several risk factors including obesity, diabetes, smoking, alcohol consumption, and chronic pancreatitis (4). Due to late-stage clinical diagnosis of human PDAC, identifying early events of disease progression has been challenging. Based on studies with genetically engineered mouse models, it has been established that PDAC originates from precursor lesions that progress in a stepwise manner (5). Lesions develop as a result

of genetic predispositions or pancreatic injury caused by environmental insults (5). The most prevalent lesion subtype is pancreatic intraepithelial neoplasia (PanINs); others include intraductal papillary mucinous lesions (IPMNs) and mucinous cysts (MCNs), which progress to PDAC, but at lower frequencies than PanINs (6, 7). High-grade PanIN precedes invasive malignancy and could be a target for treatment intervention (**Fig. 1.1**). However, detecting them with currently available imaging modalities is not possible, given their small size (6, 7). In more than 90% of PanINs, mutations in KRAS initiate pancreatic tumorigenesis (8). The progression of PanIN to PDAC is orchestrated KRAS mutations as well as by additional genomic events including inactivation of tumor suppressors TP53, p16/CDKN2A and SMAD4 (8). Microenvironmental factors that influence PanIN progression remain elusive. There is an unmet need to non-invasively detect PanINs prior to disease progression for early treatment intervention.

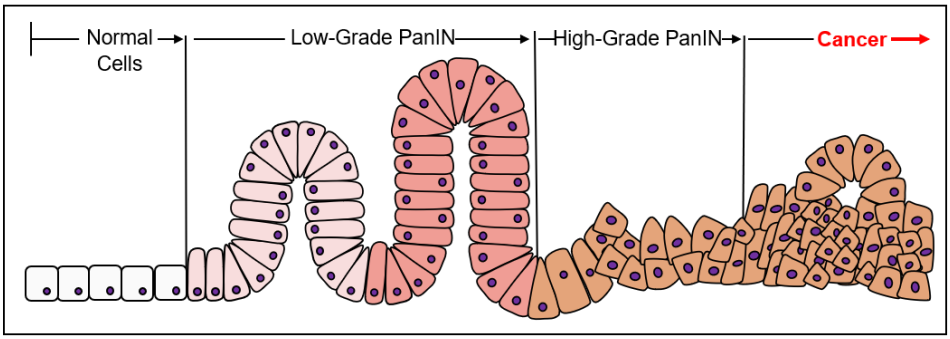


Figure 1.1 Scheme depicting progression of PanIN to PDAC.
Transformation of normal epithelium to low-grade PanIN, followed by high-grade PanIN to invasive malignancy (left to right).

1.3 Pancreas Cancer Tumor Microenvironment

A hallmark feature of PDAC is the desmoplastic stroma that accounts for 80% of the tumor composition (9) and plays an important role in promoting tumor growth and immune evasion. The interactions between tumor cells and stromal cells limit treatment efficacy (9). The primary components of the microenvironment include cancer associated fibroblasts, myeloid cells, CD4 T cells, and CD8 T cells. The crosstalk among these microenvironmental components and their contribution to disease pathogenesis is an area of active investigation and is the focus of this thesis (**Fig. 1.2**).

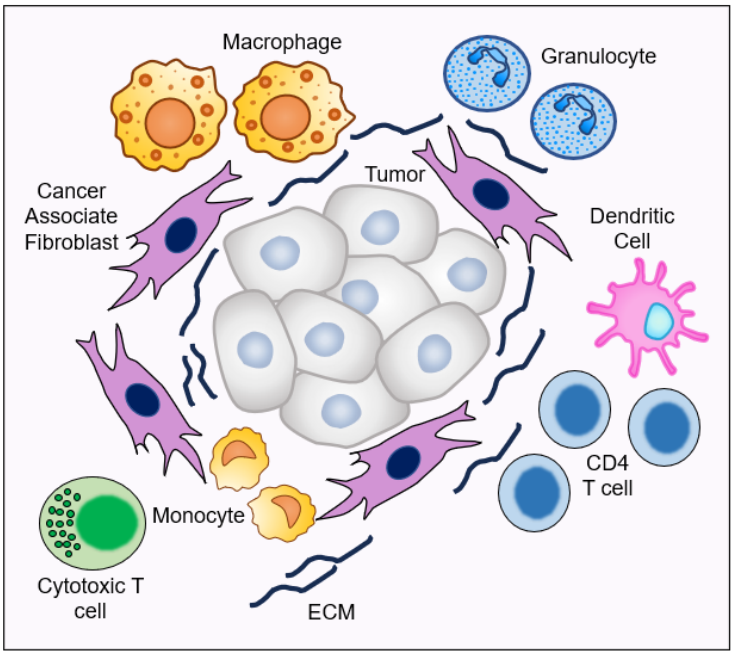


Figure 1.2 The tumor microenvironment in PDAC.
The primary cell types in the microenvironment include myeloid cells (macrophages, granulocytes, dendritic cells), monocytes, cancer associated fibroblasts, CD4 T cells, and CD8 T cells, as well as extracellular matrix (ECM).

Cancer Associated Fibroblasts

Cancer associated fibroblasts (CAFs) are a predominant cell type in the PDAC microenvironment that modulate desmoplasia-a major barrier that precludes therapeutic delivery and infiltration of anti-tumor T cells (10). The rich stroma develops because of secretion of extracellular matrix proteins including collagens, growth factors, matrix metalloproteinases, proteoglycans, proteolytic enzymes, and cytokines/chemokines (10), factors that contribute to pro-tumorigenic signaling. The function of CAFs at different stages of tumorigenesis is not well understood. Previous work in genetically engineered mouse models suggests that pancreas resident stellate cells (11), malignant cells that have undergone epithelial to mesenchymal transition (12), monocytes, and/or bone marrow derived mesenchymal stem cells (13) may be sources of CAFs (14). These studies highlight that heterogeneous origin and function of CAFs in PDAC microenvironment. There is also evidence of heterogeneity of CAF subtypes with specific tumor-promoting or tumor-restricting roles (10). For instance, myofibroblasts (myCAFs) exist in close proximity to malignant cells and express high levels of αSMA and Col1a1 in response to TGFβ, restricting tumor growth (15), while CAFs with complement-secreting

phenotype (csCAFs) are located adjacent to malignant cells and regulate immune responses (16). Inflammatory CAFs (iCAFs) are located further from malignant cells and exhibit Cxcl1 and Il6 expression in response to IL1/JAK/STAT3 signaling, promote tumor growth (17). Finally, CAFs capable of presenting antigens to T cells via MHC class II are classified as apCAFs (18). Several strategies aimed at targeting CAFs have failed clinically (14), highlighting the need for expanding our understanding of CAF heterogeneity in PDAC microenvironment.

Myeloid Cells

Within the immune compartment of the PDAC microenvironment, myeloid cells have been shown to be key regulators of immunosuppression and strong correlates to poor clinical outcomes (19, 20). Myeloid cell types found in the TME include dendritic cells, monocytes, myeloid derived suppressor cells, granulocytes, and macrophages (21). Macrophages are the most abundant in the TME and secrete cytokines such as CSF-1 and CCL-2 (22, 23). Myeloid cells' most well-known role in PDAC is their ability to mitigate anti-tumor effector T cell function through the release of immunosuppressive cytokines that in turn recruit other cells known to further dampen cytotoxic immune responses, such as T regulatory cells (24). Myeloid cells also mediate the expression of immune checkpoint ligands on tumor cells as another mechanism of immune evasion (21). In addition to their role in T cell response, tumor infiltration by myeloid cells is critical for PDAC initiation, as they directly promote the formation and maintenance of preneoplastic lesions through factors including EGF ligand and PDGF in murine models of PDAC (25, 26).

CD4 T cells

CD4 T cells play an important role in shaping an immune response (27). They regulate macrophage function, B cell antibody production, and CD8 T cell priming (28). When naive CD4 T cells encounter an antigen, they differentiate into specialized subsets that are dependent on the cytokines and co-stimulatory molecules present in the milieu (29). The distinct CD4 subsets including T helper (Th)1, Th2, Th17 or regulatory T cells (Tregs) (29). Conventionally, Th1 cells are induced by IL-12 and IFNy cytokines, which signal through Stat4 and Tbet transcription factors to produce IL2, IFNy, and TNFa (30, 31).

These factors activate intracellular cytolytic mechanisms in macrophages. On the other hand, activation of Th2 cells is induced by IL4, which signals through Gata3 and Stat5 to produce IL4, IL5, and IL13; these in turn promote macrophage mediated tissue repair (30, 31). Th17 differentiation is induced by IL1, IL6, IL21, IL23, and Tgfb, which signal through RORγt to produce IL17, IL21, IL22, IL26 and TNFa to promote recruitment and activation of neutrophils (30, 31). Tregs differentiation is induced by Tgfb and IL2, which signal through FOXP3 to produce IL10, which regulates immunosuppressive macrophage responses (30, 31).

In PDAC, increased abundance of Th2 over Th1 cells within the stroma corresponds with reduced patient survival (32). Similarly, it has been noted that IL17 promotes tumor growth through the recruitment of granulocytes (33). In contrast, depletion of Tregs strikingly reprogramed fibroblasts to secrete factors for myeloid recruitment, which accelerated tumor growth in a spontaneous mouse model (34). Together, these studies illustrate that the balance of CD4 T cell subsets play complicit roles in the PDAC microenvironment.

CD8 T cells

The abundance of CD8 T cells and their proximity to PDAC tumor cells is an important determinant of clinical outcomes (35-37). Generally, CD8 T cell activity is regulated by three sequential steps: expansion, survival, and memory formation (38, 39). During expansion, naive CD8 T cells are primed in the lymph nodes, where antigen presenting cells present cognate tumor antigens in the context of MHC class I and engage co-stimulatory molecules including CD28, CD27, OX40 and 41BB (38, 39). Once activated, CD8 T cells undergo clonal expansion and migrate to the tumor site to exert cytotoxic activity. Effector CD8 T cells release IFNy, granzymes, and TNFa or induce FasL apoptosis to eliminate tumor cells (38, 39). Post cytotoxic activity, a small portion of effector CD8 T cells survive to differentiate into long-lived memory T cells (38, 39). Cues in the tumor microenvironment impact effector CD8 T cell function; for instance, the presence of pro-inflammatory cytokines IL2, IL12, and IFNy promote CD8 T cell activation, while IL7 and IL15 promote memory formation (38, 39). Interestingly, localization of effector CD8 T cells in the stroma reduces their cytotoxic function (35-37).

Furthermore, it has been noted that CD8 T cells in the PDAC microenvironment exhibit an exhaustion phenotype with high expression of markers including LAG-3, PD-1 and TIGIT (40, 41). Although immune checkpoint blockade targeting PD-1 has been successful in preclinical mouse models, it has failed to benefit patients clinically (42). In summary, gaining mechanistic insight into how the different factors in the microenvironment regulate anti-tumor CD8 T cell responses are needed to improve therapeutic outcomes for PDAC.

1.4 Transcriptomic Characterization of PDAC Microenvironment

Strategies to molecularly profile human pancreatic tumors are crucial to help unravel the complexities of human disease. Single-cell RNA sequencing (scRNA-seq) has emerged as a powerful analytical method for defining cell-specific molecular signatures and mapping out the interactions of cell types within the tumor microenvironment (43-48). Through scRNA-seq, cell types and states can be characterized in an unbiased manner, making this strategy key to elucidating the behavior of cells within the PDAC TME (**Fig. 1.3**). We now understand that patient tumors exhibit intratumoral heterogeneity, with several transcriptomic states of cell types coexisting within the tumor, which is why no two patients respond to therapies similarly (43-48). Ultimately, harnessing the power of scRNA-seq technology will help unravel the intricacies of these cell-cell interactions in human PDAC and lead to the development of novel therapies targeting the microenvironment to improve outcomes for this dismal disease.

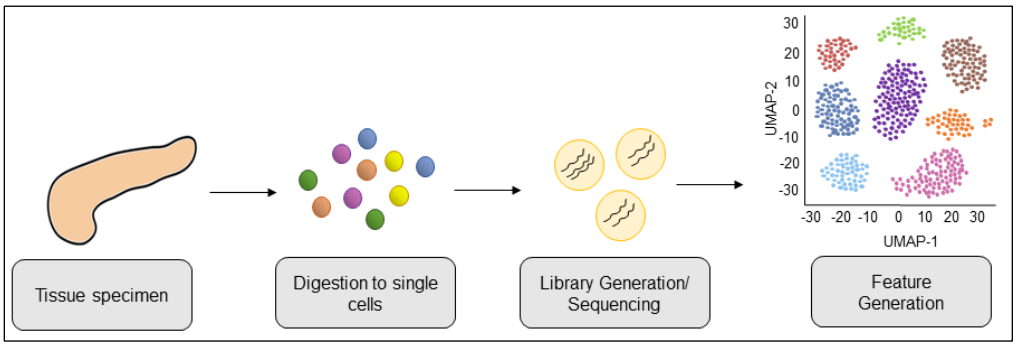


Figure 1.3 Workflow of Single-Cell RNA-sequencing PDAC tissue
PDAC tissue is collected from patient donors and digested into single cell suspension of live cells. Cells are lysed, cellular mRNA captured, and cDNA libraries are generated and subjected to high-throughput sequencing. This is followed by bioinformatics analysis, including downstream feature generation and visualization of cell clusters by Uniform Manifold Approximation and Projection (UMAP).

JAK/STAT3 Signaling Regulates Tumorigenesis

The Janus kinase/signal transducer and activator of transcription (JAK/STAT) signaling pathway has been identified as a mediator of tumor progression and immune evasion (49-52). Pathway activation is initiated by growth factors and cytokines including hormones, colony-stimulating factors, interferons and interleukins (53, 54). Upon the binding of these factors to the extracellular domain of cell surface receptors, signals are transduced intracellularly. Jak family members (JAK1, JAK2, JAK3, and TyK2) promote the phosphorylation of STAT members (STAT1, STAT2, STAT3, STAT4, STAT5a, STAT5b, and STAT6) located in the cytoplasm, which translocate to the nucleus to regulate gene expression (54). STAT3 signaling has been implicated in pancreas cancer (55-57), though its exact role remains unclear. Immunohistochemical analysis has revealed elevated levels of phosphorylated STAT3 in tumor tissue, but not in normal pancreas (55-57). STAT3 is activated by members of the IL6, IL121, IFN-I, G-CSF, and leptin families (54). Several studies have reported the functional importance of STAT3 in KRAS driven tumorigenesis and fibroblast reprogramming in PDAC (49, 52, 58). Furthermore, targeting the JAK/STAT3 pathway enhanced gemcitabine-induced cell apoptosis in a preclinical mouse model of PDAC (59). However, the role of JAK/STAT3 signaling in immune cells in the PDAC microenvironment has not been explored. Since STAT3 is ubiquitously expressed within immune cells, particularly in immunosuppressive myeloid cells, understanding the contribution of the signaling pathway in PDAC immune evasion will be important to developing targeted therapies.

Scope of the Dissertation

This dissertation addresses how crosstalk between distinct cell types in the pancreas cancer microenvironment modulates mechanisms of tumor immune evasion and immune suppression. Chapter 2 presents a comprehensive comparison of the neoplastic lesion microenvironment and the PDAC microenvironment in humans. The healthy human pancreas is rarely studied as it degrades shortly after death. In addition, no indications exist to biopsy the healthy pancreas. Our work was the first to comprehensively evaluate the transcriptomic states of cells in the healthy pancreas relative to PDAC (60). Analysis of an initial group of 30 pancreata surprisingly revealed that the majority of healthy

pancreata, irrespective of donor age, gender, or racial and ethnic backgrounds, contained neoplastic lesions with a microenvironment distinct from those in PDAC. Intriguingly, fibroblasts surrounding lesions were transcriptionally different from PDAC fibroblasts, while myeloid cells in healthy samples had a transcriptional profile similar to tumor associated macrophages. Given that pancreatic cancer is relatively rare, a vast majority of lesions do not progress to malignancy, and our work provides insight into potential factors in the microenvironment that promote malignant transformation.

Chapter 3 focuses on whether JAK/STAT3 signaling in myeloid cells regulates tumorigenesis. Although JAK/STAT pathway emerged as a good clinical target for PDAC (55-57), with the efficacy of several inhibitors currently being examined, no promising outcomes have been observed. The impact of JAK/STAT3 signaling in distinct cell compartments in the PDAC microenvironment remains to be explored. Since myeloid cells contribute to tumor progression, we evaluated the role of JAK/STAT3 signaling in myeloid function. We found that loss of STAT3 in myeloid cells reduces tumor progression, providing insight into therapeutic resistance mechanisms.

Chapter 4 examines whether crosstalk between Type 2 helper T cells and fibroblasts promotes tumorigenesis. The PDAC microenvironment is characterized by an abundance of CD4 T cells, and Tregs and Th2 subsets in particular play an important role in regulating inflammatory processes (32). Previously, we showed that depletion of Tregs accelerates tumorigenesis (34). Our data surprisingly showed that in the absence of Tregs, CD4s polarize to Th2 cells. Remarkably, we noted that fibroblasts respond to type 2 cytokines, suggesting potential crosstalk between Th2 cells and fibroblasts. Results from our study will provide insight into the contribution of the Treg/Th2 axis in PDAC development and disease progression.

A discussion of the broader implications of this work and future directions for chapters 2-4 is presented in Chapter 5.

Chapter 2 -Analysis of Donor Pancreata Defines the Transcriptomic Signature and Microenvironment of Early Neoplastic Lesions

This chapter has been published.
Carpenter, E. S*., Elhossiny, A. M*., Kadiyala, P*., Li, J., McGue, J., Griffith, B. D., Zhang, Y., Edwards, J., Nelson, S., Lima, F…Frankel, L. T., [#] Pasca di Magliano, M[#]. Cancer Discovery. 2023; *13*(6), 1324–1345.PMID: 10236159 *Authors contributed equally, [#]Co-corrosponding authors

Abstract

The adult healthy human pancreas has been poorly studied given lack of indication to obtain tissue from the pancreas in the absence of disease and rapid postmortem degradation. We obtained pancreata from brain dead donors thus avoiding any warm ischemia time. The 30 donors were diverse in age and race and had no known pancreas disease. Histopathological analysis of the samples revealed PanIN lesions in most individuals irrespective of age. Using a combination of multiplex immunohistochemistry, single cell RNA sequencing, and spatial transcriptomics, we provide the first ever characterization of the unique microenvironment of the adult human pancreas and of sporadic PanIN lesions. We compared healthy pancreata to pancreatic cancer and peritumoral tissue and observed distinct transcriptomic signatures in fibroblasts, and, to a lesser extent, macrophages. PanIN epithelial cells from healthy pancreata were remarkably transcriptionally similar to cancer cells, suggesting that neoplastic pathways are initiated early in tumorigenesis.

Introduction

The pancreas, a main source of digestive enzymes, is uniquely susceptible to degradation *post mortem*(61-64). As there is no indication to sample the human pancreas in absence of a pathology, our understanding of this organ is limited, and has so far not benefited from advances in technology such as the single cell revolution of the last

decade. Pancreatic ductal adenocarcinoma, the most common and deadly form of pancreatic cancer, arises from the exocrine pancreas(65, 66). Different precursor lesions precede overt malignancy including mucinous lesions which can be seen on imaging and surgically treated as indicated(67-70). In contrast, pancreatic intraepithelial neoplasia (PanIN) is microscopic and typically only encountered following resection of other pancreatic pathologies, including overt cancer(71-73). Autopsy studies -mostly in an older patient population- indicate that PanIN is common in older individuals, however poor preservation of the pancreas due to prolonged warm ischemic time severely limits molecular analysis of autopsy samples(74-78). The prevalence of PanIN in the general healthy population remains unknown.

Pancreatic cancer is characterized by the accumulation of an extensive fibroinflammatory microenvironment, rich in extracellular matrix and including cellular components such as fibroblasts and immune cells. Genomic studies have characterized the mutation profiles of primary and metastatic tumors and reinforced the notion that the KRAS gene is almost invariably mutated in pancreatic cancer, together with common loss of tumor suppressor genes(79-82). Over the past several years, the advent of single cell technologies has given us unprecedented insight into the cellular composition of the tumor microenvironment, the heterogeneity across and within populations, and the signaling pathways driving cellular crosstalk(43-46). Pancreatic cancer is also characterized by accumulation of immune cells, including myeloid and lymphoid components; myeloid cells are largely immunosuppressive while T cells are exhausted in the majority of cancer patients(19, 36, 83, 84). Whether corresponding populations of fibroblasts, myeloid cells, and T cells are present in the healthy human pancreas is unknown. A key limitation is that control samples are largely constituted by adjacent normal pancreas; while lacking malignant tumor cells, these samples are often not histologically normal and present with extensive inflammation and other alterations. PanIN studies, while revealing that these lesions share a similar mutation profile as cancer samples(70, 85-89) (bioRxiv 2023.01.27.525553), are largely conducted in tissue from cancer patients or patients with different pancreatic pathologies, based on paraffin-stored samples. Thus, our understanding of the microenvironment of the human pancreas and of early lesions is extremely limited. While mouse models have been instrumental to

understand the early stages of pancreas carcinogenesis and to study the healthy organ(90-93), they are a poor substitute for human samples. Mice are short-lived; laboratory mice spend their life in a highly controlled environment with specified diet, activity levels, light/dark cycle and none of the environmental and lifestyle stressors that characterize human life.

Here, we describe a unique partnership between the Pancreatic Disease Initiative at the University of Michigan and Gift of Life Michigan, a centralized organ procurement and allocation center located less than 6 miles from the University Hospital and its laboratories. While efforts are made to offer every organ to potential recipients in need, confounding factors often exist, including underlying disease of the donor (ie. diabetes and obesity) or, commonly, exhaustion of the recipient list which preclude transplantation, rendering organs available for research. This is particularly true for organs procured in donation after brain death (DBD). Unlike traditional organ donation where death occurs following cardiovascular decline and subsequent hypotension and hypoxia, DBD maintains blood flow to organs until they can be rapidly flushed with physiologic solution and immediately cooled to just above freezing. We posit these organs to be ideal for research analysis where limitation of hypoxia, electrolyte imbalance and rapid cooling will maximally preserve the cellular and transcriptomic profile of the normal pancreas. Our partnership with Gift of Life Michigan and close physical proximity has allowed for analysis of pancreata from 30 DBD donors of varied age, race and sex, resulting in a first ever comprehensive map of the microenvironment of the organ in humans. Additionally, because donors are brought to the Gift of Life Donor Care Center from across the state of Michigan, there is a broad range of ethnicity, socioeconomic status and environmental exposure magnifying the applicability of these findings.

Results

The adult human pancreas harbors frequent PanIN lesions

Through a collaboration with the Gift of Life Michigan Organ and Tissue program, we collected 30 pancreata from healthy adult organ donors, for whom no suitable recipient was identified. Of note, all donors were pre-screened via cross-sectional imaging and lab values (amylase and lipase) prior to organ recovery and were found to have no identifiable

pathology in the pancreas. The organs were dissected from surrounding tissue and superior mesenteric and celiac arteries isolated. The arteries were cross-clamped and a cooled, isotonic physiologic solution was infused for 15 minutes. The organ was then rapidly removed and placed in sterile solution at 4°C and transported to the University of Michigan for processing within 90 minutes of cross clamp time (**Fig. 2.1A**). This method allows for no warm ischemic time, preserving the transcriptomic profile of the pancreas. As a pilot, we compared cell viability in samples from donation following brain death (DBD) with donation after circulatory death (DCD). In the latter, the heart and lungs are allowed to stop typically after a period of hypoxia and hypotension. This method is associated with a warm ischemic time of approximately 30-90 minutes resulting in a dramatic decrease in pancreatic cell viability of less than 20%; we thus discontinued the DCD program (**Fig. 2.2A**). Patient age spanned from the third to eighth decade of life and included 20 males and 10 females. Our patient cohort included about 2/3 white donors, 1/3 African American donors, one Asian donor, and one donor of unknown race, closely reflecting the demographic makeup of the State of Michigan (**Fig. 2.1B** ,Table 1). For each sample, we collected 15 tissue blocks from multiple regions along the head-tail axis **(Fig. 2.2B)**. Histopathological analysis of each block revealed PanINs in 18 of 30 donor specimens (**Fig. 2.1B** and **2.1C,** refer to data availability statement for access to full slide scans) as well as normal acinar parenchyma, normal ducts and areas of acinar-to-ductal metaplasia (ADM) (**Fig. 2.2C**). PanIN distribution ranged from isolated lesions in one region of the pancreas to multifocal. PanINs were surrounded by an area of fibrosis with interspersed cellular components (**Fig. 2.1C**).

PanINs from healthy individuals are surrounded by a unique microenvironment

To characterize the immune and stromal composition of the PanIN microenvironment, we performed multiplex fluorescent immunohistochemistry on formalin-fixed, paraffin-embedded tissue. We used a previously described immune panel (46) (**Fig. 2.3A, Fig. 2.4A**) and a newly optimized fibroblast panel (**Fig. 2.2B, Fig2.4B**). We then quantified cellular composition in areas including PanIN compared with areas including normal acini, ducts or ADM. Myeloid cells were enriched in ADM and PanIN areas compared to areas surrounding normal acini and ducts; CD4 T cells (but not Treg) were notably detected around PanINs and ADM when compared to acinar cells and normal ducts (**Fig. 2.3A,C**).

Abundant fibroblasts surrounded both normal ducts and PanINs, although the latter showed more heterogeneous staining for vimentin, αSMA, PDGFRb, and FAP (**Fig. 2.3 B,D**), possibly indicating higher complexity of subtypes. Thus, PanIN formation is accompanied by the establishment of a unique microenvironment rich in fibroblasts, myeloid and T cells, distinct from the histologically normal pancreas.

To gather further insight in the composition of PanIN and its microenvironment, we performed single cell RNA sequencing of 6 donor organs, for a total of 44,068 cells (**Fig. 2.5A**). For five of the pancreata, we sequenced head and tail samples separately **(**Table 1**,** last column**).** On histological analysis, 4 of the pancreata had PanIN lesions while no lesions were detected in the remaining two. We used uniform manifold approximation and projection (UMAP) for visualization of cell populations and identified each population based on published lineage markers, detecting epithelial cells (acini and ducts) as well as non-epithelial cells (myeloid cells, lymphocytes, fibroblasts, and endothelial cells) (**Fig. 2.5A**, **Fig. 2.6A**). The cellular composition was variable across samples, with no significant trend based on whether individual pancreata harbored lesions (**Fig. 2.5B**).

To evaluate the spectrum of myeloid populations in the human pancreas, we subsetted the myeloid cells from the single cell dataset (**Fig. 2.5C**) and identified subclusters based on previously published signatures (**Fig. 2.6B**) (43). Myeloid populations were largely dominated by alternatively activated, resident and classical macrophages, while granulocytes were rare to undetectable (**Fig. 2.5C, Fig. 2.5D).** Alternatively activated macrophages expressed the expected markers of *MARCO* (scavenging receptor), *APOE*, and *SPP1*; resident macrophages were high in complement component encoding genes; classical macrophages expressed *CCR2, LYZ,* and, *FCN1;* finally, *a* very small population of nonclassical ($CD14^{Low}$) macrophages expressed *FCGR3A* and *LILRA5* (**Fig. 2.5B-C**).

Pancreata also harbored lymphocytes, including $CD4^+$ and $CD8^+$T cells, B cells, and NK cells (**Fig. 2.5E, Fig. 2.5F**). We did not readily capture any regulatory T cells. We detected both cytotoxic and exhausted $CD8^+$ T cells, the former identified by *KLRC* and *XCL1* expression; the latter by *GZMK* and *KLRG1* expression (**Fig. 2.7A, Fig. 2.7B**). Analysis of B lymphocytes showed a large population of memory B cells expressing *IGHM* and *IGHD*, germinal B cells marked by *RGS13* expression, and plasma cells characterized by lack of *HLA-DRA* and presence of *IGHG4, SDC1, and IGHG1* (**Fig. 2.7A, Fig. 2.7C**).

Thus, the human pancreas houses a variety of innate and adaptive immune cells. Of note, the dissociation step, required for single cell RNA sequencing, precludes determination of whether any of the immune cells were derived from normal pancreas parenchyma, or from areas surrounding PanIN lesions; however, our multiplex immunostaining data shows that macrophages are present throughout the tissue while T cells are more likely to localize near PanIN (**Fig. 2.3)**.

We then analyzed fibroblasts, endothelial cells, and pericytes together, as these cells share several markers. We identified 3 distinct populations of fibroblasts, Fibro1 (*DPT* low), Fibro 2 (*DPT* high), and Fibro3 (expressing *FBLN2* and *CFD*) (**Fig. 2.5G-H, Fig. 2.8A**). Notably, *DPT* was recently described as a pan-fibroblast marker across multiple organs and diseases states in mouse tissues(94); based on our data, *DPT* is expressed across fibroblast populations in the adult human pancreas, albeit at variable levels (**Fig. 2.8B)**. Fibroblasts also had universally high expression of *PDGFRB/A,* and, to a lesser extent, *PDPN* (**Fig. 2.8B-C**). *PDGFRB* was also expressed by pericytes while *PDGFRA* was only expressed in fibroblasts (**Fig. 2.8B-C**). In contrast, *ACTA2* was expressed by a small subset of fibroblasts only (**Fig. 2.8B**). *LRRC15*, a marker recently associated with tumor promoting pancreatic CAFs (95), was not expressed in normal pancreas fibroblasts, but was detected in a few cells in the Endo5 endothelial cell cluster(**Fig. 2.8B**). Lastly, FABP4, which labels pancreatic stellate cells in mice (96), only labeled a few fibroblasts but was widely expressed by pericytes and endothelial cells, possibly highlighting a mouse/human difference or reflecting the age of the donors (**Fig. 2.8B**). We then compared our fibroblast populations to fibroblasts described in the healthy mouse pancreas (95, 97). We did not observe a 1:1 correlation between any of those previously described mouse populations and our human fibroblast populations, but, broadly, the mouse gene signatures were expressed in human fibroblasts, highlighting some common aspects but also possible species-specific differences (**Fig. 2.8D**). We identified 5 endothelial cell populations (Endo1-5, **Fig. 2.5G-H, Fig. 2.8A and 2.85E**), expressing varying levels of *VWF, CDH5, FABP5*, and *CD74* (**Fig. 2.8A**), and two pericyte populations, expressing RGS5 (**Fig. 2.8A**). The Endo5 population was notable given its elevated expression of angiogenic factors *IL33, TFF3, CXCL2,* and *KRT18* (**Fig. 2.8A,**

Fig 2.8E). The prevalence of each cell type, both for immune and non-immune components of the microenvironment was variable across donor samples.

Overall, the normal pancreas includes a heterogeneous set of structural cells, such as fibroblasts, pericytes, and endothelial cells, as well as immune cells. The normal human pancreas also presents with histological heterogeneity, reflecting age and the complexities of human lifestyle and genetics.

Comparison of the microenvironment in healthy pancreata and pancreatic tumors reveals distinct stromal features.

We next sought to investigate the differences in the microenvironment of the normal pancreas and pancreatic cancer. For this purpose, we integrated single cell RNA sequencing data from healthy donor samples (6 pancreata; 11 samples total) with our previously published dataset(98) of tumor (n=16) and adjacent normal (n=3) samples. The latter were obtained from patients undergoing surgery for duodenal adenoma, ampullary carcinoma or PDA, respectively, and tissue was confirmed to be free of cancer by pathologic evaluation. UMAP two-dimensional visualization showed a wide variety of epithelial and non-epithelial cells (**Fig. 2.9A**). In terms of cell type composition, each sample was unique (**Fig. 2.10A**); however, some common themes emerged. As expected, acinar cells were captured in abundance in the normal samples and, to an extent, in adjacent normal, while they were rarely captured in tumor samples (**Fig. 2.9B** and **Fig. 2.10B**). Conversely, tumor samples had a higher proportion of macrophages and $CD4^+$ T cells. Granulocytes were rarely detected in normal samples and only observed in 1 out of 3 adjacent normal samples, but they were abundant in most tumor samples. The proportion of $CD8^+$ T cells was variable across each group of samples. Endothelial cells were generally more abundant in healthy pancreata and adjacent normal, although occasionally detected in individual tumors. Using differential abundance analysis to generate a neighborhood graph differential abundance plot (99) between healthy and tumor samples, we defined cell populations with significant shifts in abundance between tumor and normal states (**Fig. 2.9C)**. We generated a beeswarm differential abundance plot(99) and found that across all samples, comparing tumors vs. normal showed loss of acinar cells and endothelial cells, and an increase in myeloid cells and non-acinar epithelial cells, likely cancer cells, in the tumor samples (**Fig. 2.9D)**.

To determine whether gene expression alone could distinguish between tumor samples and normal pancreas, we aggregated sequencing data from all of the cells in each sample (pseudo-bulk) and applied correlation and principal component analysis (PCA) on normalized gene-sample count matrices. Both plots showed that tumor samples largely clustered separately from healthy samples; adjacent normal samples were variable (**Fig. 2.9E, 2.9F**). The classification of adjacent normal is to be interpreted with caution given the relatively small sample size. As pseudobulk analysis of total cells is affected by cellular composition in each sample, we then repeated analysis on a population-specific basis, initially focusing on broad stromal cell populations, namely myeloid cells, T cells and fibroblasts. The PCA plots revealed clear clustering of tumor vs normal samples, while adjacent normal were variable, and at times interspersed with the healthy and/or tumor samples (**Fig. 2.9F**). Lastly, we plotted predicted Ligand-Receptor interactions(100) between cell populations that were increased in tumors compared with normal samples. Epithelial signals enriched in tumor samples included *EGFR* ligands, consistent with activation of this pathway in pancreatic cancer (101, 102). *SAA1*, a factor linked to promotion of pancreatic carcinogenesis (103), was also elevated in tumors (**Fig. 2.9G**). Signaling from fibroblasts (as well as from pericytes and endothelial cells) was prominently increased in tumor samples when all possible interactions were measured (**Fig. 2.10C, 2.10D**); specific findings includes an increase in extracellular matrix signaling driven by collagen and fibronectin (**Fig. 2.9G**), consistent with the fibrotic microenvironment of pancreatic cancer(104). Macrophages showed an increased production of *CCL* and *CXCL* family cytokines, linked to tumor-promoting and immunosuppressive pathways (34, 105).

To further investigate changes in cellular composition and in gene expression patterns, we further analyzed specific cell populations. For this comparison, we focused on myeloid cells and fibroblasts, cell types that were present in abundance both in tumor and normal samples. Myeloid cells included granulocytes, derived largely from tumors, and several populations of macrophages detected across samples (**Fig. 2.11A, Fig. 2.12A**). Dendritic cells (including FCER1A^{+}, CLEC9A^{+}, and LAMP3^{+} DCs) were detected in a few of the samples, but not abundant enough for meaningful gene expression comparisons. In contrast, alternatively activated, classical, nonclassical and resident macrophages

(defined based on the markers shown in **Fig. 2.12B**) were abundant both in the healthy pancreas and in pancreatic cancer. PCA analysis of each of these populations revealed distinct gene expression patterns in tumors vs healthy organs; adjacent normal samples were again variable and interspersed with healthy and tumor samples (**Fig. 2.11B**). Pathway annotation revealed an increase in chemotaxis pathways in tumors vs healthy pancreata, indicating that signaling programs in myeloid migration as largely responsible for the transcriptomic differences between tumor and healthy states (**Fig. 2.12C**). Performing differential expression analysis between macrophages from the healthy organs versus tumors, interestingly, did not reveal any signature markers of tumor associated macrophages (106) (**Fig. 2.11C**). We then individually plotted known TAM markers. Among those, *APOE, MRC1, C1QA, C1QB* and *SPP1,* described by our group and others as TAM-specific in mouse models (106-108), were unexpectedly expressed at similar levels in healthy pancreas-associated macrophages and TAMs (**Fig. 2.11D)**. The only exception was *CXCL8* which was only detected in TAMs (**Fig. 2.11C** and **2.11D**). This finding was surprising and differentiated our human data from mouse model findings, where these factors are lowly expressed or undetectable in healthy organ macrophages.

Fibroblast and pericyte clustering identified two distinct fibroblast and two distinct pericyte populations (**Fig. 2.11E-F** and **Fig. 2.12D-E**). Fibroblast cluster Fibro2 was almost entirely derived from tumor samples, while fibroblast cluster Fibro1 was derived from both healthy and tumor samples, predominantly the former. Interestingly, fibroblast cluster Fibro2 expressed relatively high levels of the myCAF(43) marker *ACTA2* and decreased expression of the iCAF(43) marker *CXCL12*, in addition to increased expression of FAP (a cancer-associated fibroblast marker known to mediate immunosuppression(109) and exclusive expression of CD55 and LRRC15. These data show that healthy pancreas fibroblasts are altogether distinct from cancer-associated fibroblasts, a notion supported by distinct clustering on PCA analysis (**Fig. 2.11G**). Differential expression analysis again revealed an increase in activation markers and markers of tumor promoting fibroblasts in tumor samples, such as ACTA2, FAP and LRRC15 (**Fig. 2.11H** shows top 20 differentially expressed genes; **Fig. 2.11I** shows selected additional fibroblast-specific genes).

Of note, we also captured several lymphocyte and NK populations, although this group was mostly derived from tumor samples, with the exception of naïve T cells, which were largely detected in healthy organs (**Fig. 2.13A** and **2.13B**). PCA plots revealed a spectrum, with some tumor T cells clustering within the normal T cell populations, and others quite distinct (**Fig. 2.13C**); pathway analysis showed tumor samples were enriched for genes in negative regulation of T cell proliferation (**Fig. 2.13D**). However, overall these T cells were less distinct between tumor and normal, an interesting finding given the hallmarks of poor immunogenicity, immune exhaustion, and impaired cytotoxic activity of T cells in pancreatic cancer (46, 110).

Overall, our analysis of human pancreata shows frequent PanINs in organs from healthy individuals. Comparison with PanINs with tumors samples identified shared inflammatory gene expression profiles of macrophages. In contrast, fibroblasts were clearly divergent in tumors compared to PanIN. Finally, T cells were rare to undetectable in normal areas of the pancreas, present in small numbers in PanINs and common in pancreatic cancer, although subsets such as Tregs were almost uniquely present only in tumors. Thus, comparative analysis reveals both similarities and differences in the components of the microenvironment.

Spatial transcriptomics reveals a unique epithelial gene signature of PanIN lesions which aligns closely with tumor epithelium.

We next focused on the epithelial population in our single cell RNA sequnecing dataset to determine if we could identify transitory cell populations, including cells undergoing acinar to ductal metaplasia and cells from PanIN lesions. Analysis of the epithelial and acinar populations revealed 16 distinct subclusters (**Fig. 2.14A, B**), with clusters 4, 5, and 6 derived mainly from tumor samples(**Fig. 2.14C**). These clusters had high expression of *S100* genes, encoding for a family of proteins often elevated in cancer cells (111), and linked to pancreatic cancer metastasis (112) (**Fig. 2.14D**). In the quest to identify any PanIN cells in donor samples, we investigated previously reported transcriptomic signatures specific to acinar, ductal, PanIN, and cancer cells (113) in our sequencing

data. Using enrichment analysis, we defined clusters enriched for the acinar, ductal, and cancer cell signatures. As expected, the acinar signature marked cells largely derived from healthy and adjacent normal samples, while tumor signature marked cells from PDAC samples (**Fig. 2.14E**). We also identified cell populations enriched for the previously described Duct-like1 (expressing normal ductal genes) and Duct-like2 (with increased expression of mucus and trefoil factor genes) signatures. In our dataset, the former mapped to cells from normal and adjacent normal samples, the latter mapping within tumor-derived cells **(Fig. 2.14E)**. In contrast, we were unable to map the PanIN signature in our single cell dataset (**Fig. 2.14E**). Interestingly, utilizing genes for *HALLMARK_KRAS_SIGNALING_UP* and *_DOWN(114)*, we observed tumor-derived epithelial cells were relatively enriched for genes upregulated with KRAS activation and relatively depleted from genes downregulated with KRAS activation (**Fig. 2.14F**). We hypothesized that PanIN cells, a relatively rare population, were not captured in our single cell dataset; another possibility is that the PanIN signature derived from tumor adjacent PanIN, as in previous studies (113), is distinct from sporadic PanIN in healthy pancreata.

To directly evaluate the gene expression pattern of PanIN, we utilized the GeoMx Nanostring spatial transcriptomics platform. After careful review of tissue slides with a clinical pathologist (JS, who specializes in pancreatic histopathology), acinar, normal duct, ADM, and PanIN regions of interest (ROIs) were selected from the donor pancreata, while tumor-associated PanINs, glandular tumors, and poorly differentiated tumor ROIs were selected from malignant samples (**Fig. 2.15A, B**). In addition, we collected ROIs from acini and normal ducts adjacent to tumors for comparison. To avoid confounding transcripts from the stroma, samples from each region were segmented using pancytokeratin (PanCK) and CD45 to select $PanCK^{+}/CD45^{-}$ cells in all ROIs, with the exception of acinar ROIs, where we selected $PanCK^{-}/CD45^{-}$ (as acinar cells do not express PanCK, and can be easily identified histologically). Following quality control and data normalization, we performed PCA analysis, and detected a prominent batch effect. Upon correction, we obtained acinar and PanIN ROIs that clustered separately, while ADM and normal duct ROIs were interspersed with each other, indicating transcriptional similarity, which is expected (**Fig. 2.16A**). To extract gene signatures specific to each cell

type, we applied linear mixed model differential expression analysis comparing each cell type to all other remaining cell types (**Fig 2.16B, Fig. 2.15C**). We thus identified expected digestive enzymes in acinar ROIs (*CEL, CPA1, CELA2B, PRSS3*), and genes encoding for mucins in ductal ROIs (*MUC5B, MUC20*). Ductal ROIs also expressed *AQP3* —encoding for a water channel protein typically found on the basolateral membrane of ducts(115) —, *MUC5B* — expressed in noncancerous pancreatic ductal epithelium(116) — and *MUC20*, which expression has not been previously reported in the pancreas. PanIN ROIs were enriched for the previously described marker *CLDN18(113, 117)*. We also detected expression of trefoil factor genes *TFF1* and *TFF2*, secretory proteins expressed in PanINs and, to a lesser degree, in early PDAC(118, 119). Interestingly, *MUC5AC*, a known PanIN marker(120), was not specifically enriched in PanIN, as its expression was also higher in glandular tumors and ducts (**Fig. 2.16C)**. ADM ROIs included *AQP1* (in contrast to normal ducts marked by *AQP3*), as well as serpin family genes (*SERPING1)* and complement (*C6*), an interesting combination as serpins regulate the complement cascade(121). While the complement system has been implicated in the pathogenesis of pancreatic cancer(122, 123), this is the first report of its upregulation in ADM from healthy pancreas, suggesting that complement dysregulation may be an early pre-neoplastic event. Lastly, glandular and poorly differentiated tumor ROIs were distinct, with glandular tumors more similar to PanIN, as expected. While healthy samples and tumor-bearing samples had a high degree of concordance in marker features for acinar, ductal, and PanIN marker features (as ADM was only captured in healthy samples), we noted that PanINs from tumor-bearing samples had higher expression of genes seen common in tumor ROIs, suggesting closer association with malignancy.

Using Gene Set Variation Analysis (GSVA), we investigated the enrichment of the previously reported PDAC subtype-specific signatures (124-126). While acinar and ADM ROIs showed relative enrichment of ADEX and exocrine-like subtypes signatures, PanIN ROIs were enriched to classical signature, and the poorly differentiated tumor ROIs displayed basal signature enrichment. Interestingly, PanIN ROIs corresponded more closely to the classical signature than glandular tumors, as the latter showed expression of basal-like genes as well, consistent with recent reports on intermediary states between

classical and basal in most human tumors at the single cell level(45, 127) (**Fig. 2.16D**). In concordance with our prior differential expression analysis showing differences between PanINs from different sources (**Fig. 2.15C**), we noted that PanINs from tumor-bearing samples expressed some basal-like genes whereas PanINs from healthy samples showed did not. Thus, sporadic PanINs from otherwise healthy pancreata are similar, but distinct, from tumor adjacent PanINs.

We then integrated spatial transcriptomics with single cell RNA sequencing data. Using the top 20 genes from each ROI class, we defined cell-type specific gene signatures for acinar, ductal, ADM, PanIN and tumor cells and mapped these signatures to the epithelial cluster from the single cell epithelial sequencing data (**Fig. 2.15D-F**). Our aim was to map cell populations relatively enriched for each defined signature. As expected, the spatial-transcriptomic derived signatures identified distinct acinar, ADM, and ductal populations (**Fig. 2.15E**). The glandular and poorly differentiated tumor signatures were, as expected, enriched in cells derived from tumor samples (**Fig. 2.15F**). While the glandular tumor signature mapped to cells spanning most of the epithelial population, consistent with its heterogeneous subtype scoring, the poorly differentiated tumor signature was confined to tumor-derived epithelial cells. Interestingly, the ADM signature was enriched in the donor-derived epithelial cells, while the PanIN and normal ductal signatures from both healthy and tumor-bearing samples only mapped to specific clusters derived from tumor samples, an unexpected finding. We thus queried whether these lesions harbored mutations in the *KRAS* gene, as previously described in human tumor associated PanIN(128). Droplet PCR analysis revealed the presence of multiple *KRAS* mutations in the samples queried **(**Table 2**)**, a finding which concords with the described polyclonality of PanINs with associated distinct KRAS mutational profiles (bioRxiv 2023.01.27.525553).

PanINs from tumors notably marked a slightly larger population of cells within the tumor-derived epithelial population than PanINs from healthy samples. This supported the differential expression analysis, which showed more shared features of tumor-bearing PanINs ROIs with tumor ROIs, compared with PanINs from healthy samples. Overall, while differences between cancer cells, tumor associated PanINs and sporadic PanINs

from healthy organs existed, similarities far outweighed any difference, suggesting that these neoplastic lesions have already acquired many, albeit not all, features of malignant cells.

Claudin 18, MUC5AC/B, and AQP1/3 distinguish normal Ducts, ADM, and PanIN in healthy pancreas.

We next endeavored to validate our gene signatures in donor tissue to determine whether they accurately identified different epithelial populations, as suggested by our transcriptomic data. We selected markers that distinguished each epithelial cell type (**Fig. 2.15C**). Our list included AQP1 (ADM-specific), MUC5B and AQP3 (normal-duct-specific), and CLDN18 and and *in situ* hybridization probe for *TFF1*(PanIN-specific), for which antibodies were readily available. We included MUC5AC as a PanIN marker, as our data supports its exclusive expression in PanINs in non-tumor bearing samples (compared to normal ducts, ADM, and acinar cells) **(Fig. 2.16C)**. For each of these markers, we performed co-immunofluorescent staining on sections obtained from 4 different donor pancreata, including E-cadherin as a common epithelial lineage marker (**Fig. 2.17-2.20)**. We also stained for p-ERK to assess the status of ERK activation in normal pancreas within acinar cells, ADM, normal ducts, and PanINs. In sections containing both PanIN and normal duct, MUC5B only stained normal ducts, while MUC5AC was specific for PanIN (**Fig. 2.21A**, **B**). CLDN18 staining was elevated in PanIN but also was positive in ADM to a lesser degree (**Fig. 2.21C**). AQP3 only stained normal ducts, while AQP1 was specific to ADM (**Fig. 2.21D, E**). *TFF1* was co-expressed with CLDN18 in PanIN (**Fig. 2.21F)**. Lastly, PanIN lesions expressed high levels of p-ERK, while areas of ADM were also positive for p-ERK (**Fig. 2.21G)**. The expression pattern held thru across samples (**Fig. 2.17-2.20**, each showing consecutive serial sections). Thus, spatial transcriptomics-derived signatures defined individual epithelial cell populations and correctly predicted protein expression of unique lineage markers.

Discussion

The pancreas and its constitutive acinar cells possess high metabolic activity and undergo rapid cell death under hypoxic conditions(61-64). During this process, granules containing proteolytic and hydrolyzing enzymes are released resulting in rapid destruction of cellular

components and nucleic acids. As such a true transcriptomic profile of the physiologically normal pancreas has remained elusive. Due to rapid degradation postmortem, autopsy samples are not suitable for techniques requiring intact RNA, including single cell RNA sequencing, and are often difficult to examine by immunostaining as well. The mouse pancreas, while histologically similar to the human counterpart, does not recapitulate the effects of age and environmental stressors that characterize human life.

As a result, single cell studies of the human pancreas have included very few samples(129, 130) or embryonic samples(131) and have focused on endocrine cells less susceptible to degradation. Previous autopsy studies on pancreata of patients deceased with no known pancreas pathology revealed frequent PanINs and KRAS mutations(70, 74-77, 85-89, 132)(bioRxiv 2023.01.27.525553), but the samples mainly represented older individuals with limited transcriptional profiling performed. In recent years, the advent of single cell technologies has led to in-depth characterization of human pancreatic cancer and its accompanied tumor microenvironment(45-47, 113, 133). In those studies, tumor specific changes are assessed in comparison with adjacent “normal” pancreas which is often desmoplastic and inflamed. Thus, the characteristics of the human pancreas, and specifically its complement of non-epithelial cells, have largely remained unexplored.

Organ donation provides a unique opportunity to collect human tissue in a controlled manner in which conditions can be optimized to suspend cellular function in a physiologic state, allowing for virtually no warm ischemic time. Histopathology analysis revealed that the majority of our cohort of donor pancreata (slightly over half) presented with PanIN, neoplastic lesions considered progenitors to pancreatic cancer. While a similar prevalence was observed before, it was in the context of autopsy studies with patients in the 7^{th} and 8^{th} decades of life(74-77, 132). Other investigators have detected a high prevalence of PanINs in the pancreas, but their studies were based on tumor adjacent normal areas (bioRxiv 2023.01.27.525553). In contrast, our study indicate that PanIN are common in the pancreas of individual with no known pancreas pathology and occur early in life. While there was a slight increase in prevalence in the elderly, the broad distribution of ages counters prior beliefs that PanINs accumulate over time. To ensure accurate assessment of PanIN burden, multiple samples were taken from the head, body and tail

of each donor organ for histologic analysis. We observed no overt difference in prevalence by anatomic region; PanINs, when present, were typically multi-focal and widely dispersed throughout the gland; based on limited sampling, individual PanINs co-expressed multiple *KRAS* mutations, consistent with recent reports (bioRxiv 2023.01.27.525553).

In mice, spontaneous PanIN is virtually never observed; the lack of PanIN in mice might reflect the age difference (mice rarely live to two years of age, and most studies are conducted on animals of less than a year old). Further, laboratory mice live in a highly controlled environment, with predictable schedules and diet and no risk factors such as environmental pollution and tobacco use. In addition to PanIN, we observed frequent areas of acinar ductal metaplasia (ADM), dedifferentiation to acinar cells to duct-like cells. In mouse, acinar cells are the prevalent source of PanIN, and PanIN is preceded by ADM(134). Duct cells can also give rise to pancreatic cancer but they appear to do so bypassing the PanIN stage(135, 136). The origin of PanIN and pancreatic cancer is still under debate, and the presence of ADM in human samples has been questioned; analysis of donor organs showed common ADM and PanIN, but no clear continuality between the two; PanINs were more often contiguous with ducts, consistent with a ductal origin as in previous reports(137-139). However, ADM associated PanINs were also detected, suggesting that both cell types might serve as the cell of origin(134, 140, 141). To better understand PanIN lesions in the context of a non-diseased pancreas, we performed multiparametric analysis of donor pancreatic tissue, pancreatic adenocarcinoma and adjacent uninvolved tissue. We determined that PanIN lesions and their surrounding microenvironment had a desmoplastic stroma which was vastly different from normal pancreatic acinar tissue including acinar to ductal metaplasia. PanIN stroma had a unique inflammatory infiltrate that included myeloid cells as well as T helper and cytotoxic T cells. In contrast to tumors, where regulatory T cells (Tregs) are prevalent(34), we detected few or no Tregs in PanINs. This is also in contrast to murine models (and possibly tumor associated PanINs) which harbor regulatory T cells adjacent to ADM and PanIN(34). Similar to pancreatic ducts, human PanIN lesions were surrounded an array of collagen and fibroblasts. While both expressed fibroblast activation protein (FAP), fibroblasts surrounding PanIN lesions also expressed vimentin and smooth muscle actin

(SMA), the latter a marker of fibroblast activation. Whether this stroma's main function is to restrain PanIN progression, as shown in experimental models(142, 143) or whether it promotes PanIN progression remains to be determined.

We sought to understand the transcriptional signature of epithelial and stromal cells in the normal pancreas. Our analysis revealed heterogeneous populations of fibroblasts and other mesenchymal cells, such as endothelial cells and pericytes, as well as abundant myeloid cells. As these same cell populations are common in pancreatic cancer stroma, we compared their characteristics in the normal organ compared to tumors. Interestingly, non-epithelial cell populations were largely distinct based on their origin, with gene expression signatures depending on their origin from the normal pancreas or from tumors. Differences in gene expression were most notable in fibroblasts, with markers of cancer associated fibroblasts (CAFs), such as the recently described *LRRC15 (144)* exclusively expressed in the latter. Of note, our fibroblast populations only partially reflected those described in the healthy mouse pancreas, a finding that might reflect species specificity. In contrast, myeloid cells were less distinct; further analysis revealed that myeloid cells in the normal pancreas displayed a gene signature reminiscent of tumor associated macrophages (TAMs); whether the TAM-like status was present originally or is a byproduct of time on life support is unfortunately impossible to determine. Fibroblasts in pancreatic cancer have been described as heterogeneous, with smooth muscle actin high, myofibroblast-like myCAFs existing in parallel with inflammatory fibroblasts (iCAFs) and antigen presenting CAFs (apCAFs)(43); additional heterogeneity is due to cell of origin and expression of other specific markers(145) Interestingly, in our cohort fibroblast populations showed a distinct shift in tumors compared to normal pancreas, the latter not clearly reflecting this CAF classification but showing a similar level of heterogeneity.

Lastly, we interrogated the transcriptional signature of PanINs from the healthy pancreas compares with normal acinar and ductal cells, tumor associated PanINs and tumor cells. Of note, tissue dissociation during processing of single cell RNA sequencing samples makes it impossible to identify PanIN cells within the samples, as spatial and histological information is lost. To bypass this limitation, we leveraged spatial transcriptomics, then integrated transcriptomic signatures from spatial data with single cell RNA sequencing data. Interestingly, we observed that PanINs in the normal pancreas and in the tumor

transcriptionally have a high degree of concordance, although do have some distinct features. Additionally, PanINs are transcriptionally distinct from ducts, and are markedly different from ADM. Surprisingly, integration of PanIN signatures with our single cell data revealed that PanINs are transcriptionally closely related to malignant tumors. This finding raises multiple questions; key among those are why PanINs, found frequently in the population, rarely progress to invasive disease given the relatively low incidence of pancreatic cancer. Notably, pancreas transplant patients do not have an increased incidence of pancreatic cancer, indicating that progression remains unlikely even upon induced immunosuppression (146). An intriguing possibility is that the PanIN microenvironment restrains malignant transformation; a direction we plan to pursue in future studies. The endeavor to identify mechanisms that inhibit or promote PanIN progression to malignancy bears important clinical significance, as results may have the possibility to be leveraged for early detection and therapeutic strategies.

Methods

Donor Sample Procurement

Donor pancreata not eligible for transplant or for whom there were no eligible recipients were collected at the Gift of Life Michigan Donor Care Center. While maintaining blood flow, the superior mesenteric arteries and celiac arteries were cross clamped and pancreas was recovered and immediately placed in physiologic organ preservation solution on ice and transported to the University of Michigan, approximately 6 miles away. Acquisition of donor pancreata for research purposes was approved by the Gift of Life research review group. Acquisition of patient tumor samples through formal written or phone consent was described previously(46) and approved by the University of Michigan Institutional Review Board (HUM00025339).

Tissue processing

Upon arrival to the laboratory, the donor pancreas was dissected by a clinically-trained pancreatobiliary surgeon. The organ was dissected into head, body, and tail, with portions of each placed into DMEM media with 1%BSA/10μM Y27632 or 10% formalin for single cell sequencing or paraffin embedding, respectively. For single cell processing, tissue was minced into 1mm^3 pieces, then digested with 1 mg/mL collagenase P for 20-30 min

at 37°C with gentle agitation. Digested tissue was rinsed three times with DMEM/1%BSA/10μM Y27632, then filtered through a 40μm mesh. Resulting cells were submitted to the University of Michigan Advanced Genomics Core for single cell sequencing using the 10x Genomics Platform.

Multiplex Fluorescent Immunohistochemistry (mfIHC)

Formalin-fixed, paraffin embedded (FFPE) tissue slides were rehydrated in triplicate with xylene, followed by a single submersion in 100% ethanol, 95% ethanol, and 70% ethanol, respectively. Rehydrated slides are then washed in neutral buffered formalin and rinsed with deionized water. Antigen retrieval was performed with sodium citrate, pH 6.0 buffer for membrane and cytoplasmic epitopes and tris-EDTA, pH 9.0 buffer for nuclear epitopes. Tissue was blocked using endogenous peroxidase at room temperature, followed by 10% donkey serum overnight at 4°C. Primary antibodies were diluted in 5% donkey serum in TBST and incubated overnight at 4°C. Subsequent multiplex staining was completed using a 1% BSA block. Upon completion of the multiplex, tissue samples were rinsed in deionized water and mounted with DAPI ProLong™ Diamond Antifade Mountant (Thermo Fisher Scientific). Images were taken using the Vectra® Polaris™ Work Station (Akoya Biosciences). Antibodies/dilutions used are listed in Table 3.

Multiplex Immunofluoresence Quantification

Images were acquired using the Mantra™ Quantitative Pathology Work Station (Akoya Biosciences). A minimum of ten images were acquired from each tissue seciton. All cube filters were used for each image capture (DAPI, CY3, CY5, CY7, Texas Red, Qdot) and the saturation protection feature was utilized. After all images were acquired, images were analyzed using inForm® Cell Analysis™ software (Akoya Biosciences). Using this software, acinar, ductal, acinar to ductal metaplasia and PanIN samples were batch analyzed by their separate diagnoses which was confirmed by a pathologist. Cell segmentation was completed using DAPI as a basis of cell location and nuclear size and all cells segmented into the following subsets (nucleus, cytoplasm, and membrane). Using the automated training software, basic phenotypes were created. For the fibroblast panel, this included Vimentin$^+$, smooth muscle actin (SMA$^+$) and PDGFR$^+$. For the immune based panel, this included CD3$^+$, CD8$^+$, CD163$^+$, PanCK$^+$ and FoxP3$^+$.

Software output consisting of mean fluorescent intensity (mfi) of each antibody-fluorophore pair, basic phenotypes, and x and y coordinates were acquired for further processing to determine relative population of each cell type.

RNA scope Multiplex Fluorescent Detection with Immunofluorescence

RNA scope Multiplex Fluorescent Detection was performed according to instructions provided by the manufacture (Advance Cell Diagnostics; ACD). Briefly, 5µm thick formalin fixed paraffin embedded normal pancreas tissue sections were mounted on charged slides and baked at 60°C for 1 hour, deparaffinized, dehydrated, and washed with 0.1% Tween-20 RNAse-free 1x phosphate-buffered saline (PBST) three times. This was followed by incubation with hydrogen peroxide for 10 minutes at room temperature and target retrieval for 15 minutes at 98°C. Slides were then blocked with Co-Detection antibody diluent (ACD) for 30 minutes prior to incubation with Claudin 18 primary antibody (1:100 in co-detection antibody diluent) for 24 hours at 4°C. The next day the tissue sections were fixed with formalin and treated with ProteasePlus Reagent (Advanced Cell Diagnostics) for 13 minutes at 40°C. Amplification and signal enhancement (AMP) were performed for two different probes/channels (C1, C2). The TFF1-C1 probe was 1x concentration, while the CCL2-C2 probe was at 50x concentration. The probes were diluted as per manufacturer's instructions and slides were incubated with them at 40°C for 2 hours. Then the slides were washed with RNA scope washing buffer (ACD) twice. Signal for each of the probes was amplified with AMP reagents, horseradish peroxidase, and tyramide signal amplification kit (ACD) at 40°C. Slides were then washed with PBST (PBS with 0.1% Tween20) three times, incubated with anti-rabbit secondary Alexa Fluor IgG (H + L) antibody (1:400 in co-detection antibody diluent) for 1 hour at room temperature. Finally, slides were incubated with DAPI for 15 minutes and washed three times with PBST prior to being mounted with ProLong Diamond Antifade. Antibodies and RNAScope probes are listed in Table 4.

Immunofluorescence Assessment with Tyramide Signal Amplification

5µm thick formalin fixed paraffin embedded normal pancreas tissue sections were mounted on charged slides and baked at 60°C for 1 hour, deparaffinized and dehydrated. Slides were then washed with deionized water for 2 minutes followed by antigen retrieval at 96 °C with 10 mM sodium citrate (pH 6) for 8 min. Once the slides cooled down to room

temperature, they were washed three times (2min per wash) with PBS and endogenous peroxides were quenched with 3% hydrogen peroxide for 15min. Tyramide signal amplification (TSA) kit (Invitrogen) was used according to manufacture's instructions. Briefly, slides were incubated with blocking serum provided in the kit and stained with antigen-specific primary antibodies overnight at 4°C: Claudin 18 (1:100), Aqp1 (1:500), Aqp3 (1:200), Muc5ac (1:200), or Muc5b (1:200). The next day slides were washed three times with PBS and incubated in anti-rabbit secondary antibody for 1 hour. This was followed by an additional three washes with PBS. TSA conjugated to 488 or 555 fluorophores was applied for 10 minutes, followed by incubation with reaction stop solution for 5 minutes. Finally, slides were incubated with DAPI for 5 minutes and washed three times with PBS prior to being mounted with ProLong Diamond Antifade. High magnification images were obtained using confocal microscopy (Leica Stellaris 8). Antibodies used are listed in Table 4.

Single-cell RNA sequencing

Samples were run using 50-cycle paired-end reads on the NovaSeq 6000 (Illumina) to a depth of 100,000 reads. Cell Ranger count version 6.0 was used with default settings, with an initial expected cell count of 10,000. The GCH38 refererence genome was used for aligment.Ambient RNA correction was done for each sample independently using SoupX(147). Briefly, SoupX estimates the ambient RNA profile from the cell-free RNA, then it estimates the cell-specific contamination fraction using a set of user-specified negative markers. Then, we used Seurat's(148) recommended workflow for scRNASeq data processing and integration. Briefly, we removed low-quality cells with more than a 15% fraction of mitochondrial genes expression or less than 200 features (genes) detected. Expression was then log-normalized to the library size, the top 2000 highly variable features were extracted and scaled for downstream analysis. For samples integration, we used reciprocal principal component analysis (rPCA), as it is preferred for datasets with several mutually exclusive cell populations, and it scales better with a larger number of samples. Count matrices were integrated to account for batch effects. Using the integrated feature matrix, we ran PCA analysis to collapse gene expression to fewer principal components (35 principal components), then Louvain clustering was done to

define different cell clusters. We used UMAP dimension reduction to create two-dimensional embedding for the cells. For cell-type annotation, we used a panel of previously known markers for different cell types in pancreatic tissue to define different cell populations. Differential cell-cell communication was performed using CellChat(149). Briefly, cell-cell communication was calculated between each cell-type pairs using the manually curated interaction database (CellChatDB) separately on tumor and healthy donor samples. Then differential cell-cell communication weight of tumor versus healthy was calculated for each cell-type pairs.

Pseudobulk RNA Differential Gene Expression (DGE)

We aggregated the counts from different samples for all (or a subset of) cells. We used DESeq2 for normalization and DGE analysis of the samples. We used PCAtools (https://www.bioconductor.org/packages/release/bioc/html/PCAtools.html) to perform and visualize PCA analysis on the samples and Pearson correlation to determine the correlation between the samples. Gene Ontology (GO) analysis was done using ClusterProfiler(150) package on the upregulated genes.

Differential Abundance

We used miloR to define differentially abundant cell populations (99). MiloR defines neighborhoods of cells using KNN graphs, after that, it uses negative-binomial regression to determine neighborhoods with differential abundance in one condition compared to the other. We set the K parameter for constructing the KNN graph to 60 as it yielded neighborhoods with a mean of 150 cells which is roughly equal 3*Number of samples as recommended by miloR authors.

Gene set scoring

For scoring different gene sets, we used AUCell(151) package. AUCell gives a score of a specific gene set for each cell using its raw counts, which makes it invariant to any downstream normalization or integration. Acinar, ductal, and tumor cell gene signatures were utilized from literature(113). We used MSigDB(152) Hallmark gene sets for KRAS activity score.

Spatial Transcriptomics Data Analysis

We used the GeoMxWorkflows package [https://bioconductor.org/packages/release/workflows/html/GeoMxWorkflows.html] for quality control and processing of Nanostring GeoMx data. Briefly, Quality control was performed to exclude the ROIs with less than 10% genes detection rate (less than 10% of the original WTA panel genes were detected) and exclude genes detected in less than 10% of the ROIs. Q3-normalization was performed for each ROI in the gene expression matrix followed by log normalization. For visualization purposes, we performed PCA analysis which clearly showed a batch effect. We used limma package(153) batch correction function to regress out the batch effect which showed clustering of ROIs from the same cell type together. To define cell-type-specific markers, we used a linear mixed model to perform DGE between each cell type and the rest of the ROIs, similar to how we define markers in single cells data. The top 20 significantly upregulated marker genes were then used as a geneset for scoring using AUCell(151). The scores are then scaled and visualized on the UMAPs of the acinar/ductal cells subset. To score different PDAC subtypes (Classical, basal, exocrine-like, ADEX) for each ROI, we used Gene Set Variation Analysis (GSVA)(154).

gDNA Isolation from pre-neoplastic lesion

Ten slides of 5 micron thickness were sectioned from two formalin-fixed paraffin embedded tissue blocks (AIFR291_C1, AII1271_C1). One slide from both cases was stained with hematoxylin & eosin and reviewed by a pathologist to identify the location of the pre-neoplastic lesion for macrodissection on the remaining nine slides. gDNA for each sample was extracted using Qiagen's QIAamp DNA FFPE Tissue kit (Qiagen, Cat # 56404).

Detection of KRAS mutations by digital droplet PCR (06745_T)

Assays specific for the detection of G12D, G12R, and G12V in KRAS were ordered through Bio-Rad (assay IDs: G12D-dHsaCP2000001, G12R-dHsaMDS615795490, G12V-dHsaCP2000005). Cycling conditions were tested to ensure optimal

annealing/extension temperature as well as optimal separation of positive from empty droplets. Optimization was done with a known positive control.

After PicoGreen quantification, 9 ng gDNA was combined with locus-specific primers, FAM- and HEX-labeled probes, MseI, and digital PCR Supermix for probes (no dUTP). All reactions were performed on a QX200 ddPCR system (Bio-Rad catalog # 1864001) and each sample was evaluated in technical triplicates. Reactions were partitioned into an average of ~20,000 droplets per well using the QX200 droplet generator. Emulsified PCRs were run on a 96-well thermal cycler using cycling conditions identified during the optimization step (95°C 10'; 40 cycles of 94°C 30' and 55°C 1'; 98°C 10'; 4°C hold). Plates were read and analyzed with the QuantaSoft sotware to assess the number of droplets positive for mutant DNA, wild-type DNA, both, or neither.

Data Availability

Raw human data from the Steele, et. al. study (98) are available at the National Institutes of Health (NIH) dbGaP database under the accession phs002071.v1.p1. Raw single cell sequencing data from donor pancreata are available at the National Institutes of Health (NIH) dbGaP database under the accession phs003229. Nanostring GeoMX data is available from the NIH Gene Expression Omnibus database under the ascension number GSE226829 and feature matrices of single-cell RNA data are available at accession number GES229413. Whole slide scans of H&E sections from the head (A), body (B), and tail (C) of all donor pancreata, taken at 1:4 magnification are available at the Zenodo image repository: https://zenodo.org/deposit/7683038.

Code Availability

All code used for this study is publicily available at the following GitHub: https://github.com/PascaDiMagliano-Lab/GoL_public_repo

Acknowledgements and Author Contributions

M.P.d.M. and T.L.F directed the study, developed the study concept and were responsible for the study design. E.S.C, P.K., B.G., J.E., S.N., J.M., F.L., K.D., W.D., D.A., C.E., M.M. and T.F performed tissue dissection and processing. A.M.E. and E.S.C performed single cell sequencing and spatial analysis. S.T. and A.B. assisted with interactome analysis.

J.M., J.E., and T.F. performed multiplex immunofluoresence and analysis. P.K., J.L., and H.W. stained and imaged tissue for ISH/IF. J.S performed clinical pathological examination and annotation of all tissue samples. E.S.C performed ROI acquisition for spatial transcriptomics. N.O. assisted with coordination of acquiring organ donor tissue. C.C. performed the Kras mutation profiling. A.R., V.S., N.P., V. G., F.B., and V.S. provided study guidance and feedback on the manuscript. E.S.C., A.M.E., T.L.F., and M.P.d.M. wrote the manuscript, which was then edited by all of the co-authors. All of the co-authors approved the final version of the manuscript before submission.

We sincerely thank Gift of Life Michigan and donors and their families who have generously provided organs for this research. We thank T. Tamsen, M. Hogan and J. Opp from the University of Michigan Advanced Genomics Core for their assistance with single cell RNA sequencing and spatial transcriptomics. We acknowledge the use of the Integrated Genomics Operation Core at the Memorial Sloan Kettering Cancer Center, funded by the NCI Cancer Center Support Grant (CCSG, P30 CA08748), Cycle for Survival, and the Marie-Josée and Henry R. Kravis Center for Molecular Oncology.

This work was supported by R01-CA268426 to M.P.d.M. and T.L.F. Work in the M.P.d.M. laboratory was also supported by NIH/NCI grants, R01-CA260752, R01-CA271510, U01-CA224145, U01-CA274154, and U54CA274371. Work in the T.L.F laboratory was supported by NIH/NCI grant U01CA274154, NIH NIDDK 5R01DK128102, and VA BLR&D Merit Award 5I01BX005777.

E.S.C. was supported by the VA BLR&D CDA IK2BX005875, the American College of Gastroenterology CDA, and by NIH NIDDK T32-DK094775. A.M.E was supported by the Rackham International Student Fellowship. P.K. was supported by NIH/NIAID T32-AI007413 and NIH/NIGMS T32-GM113900. J.L was supported by NIH/NIGMS T32GM007863. K.D. was supported by NIH/NCI F31-CA265085-01A1. AR was supported by NCI Grants R37-CA214955, CCSG Bioinformatics Shared Resource 5 P30 CA046592. F.B. was funded by the Association for Academic Surgery Joel J. Roslyn Award and NCI R01-CA271510. J.S. was funded by NIH NCI K08CA234222 and R37CA262209. The funders had no role in study design, data collection and analysis, decision to publish or preparation of the manuscript.

Figures

Figure 2.1

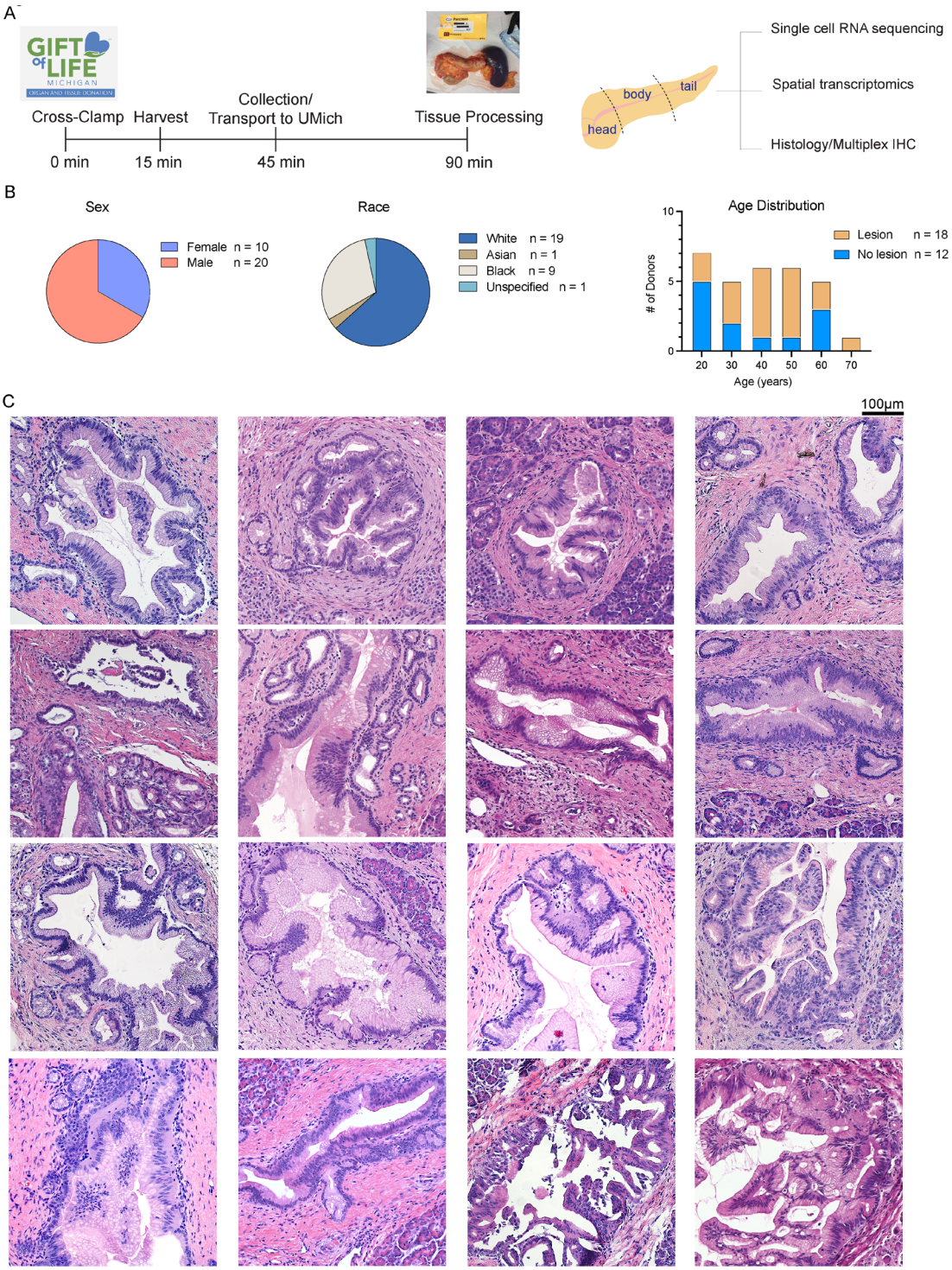


Figure 2.1 The adult human pancreas harbors frequent PanIN lesions
(A) Schematic of workflow to recover and process Gift of Life donor pancreas organs.
(B) (Left) Population distribution barplot of donor cohort. Tan bars represent donors that were found to have PanIN lesions on histological examination. Blue bars represent donors in whom no neoplastic lesions were found. (Middle) Pie chart of donor cohort by sex. (Right) Pie chart of donor cohort by race. (C) H&E of representative PanIN lesions found in donor pancreata. Each H&E section represents a different donor.

Figure 2.2

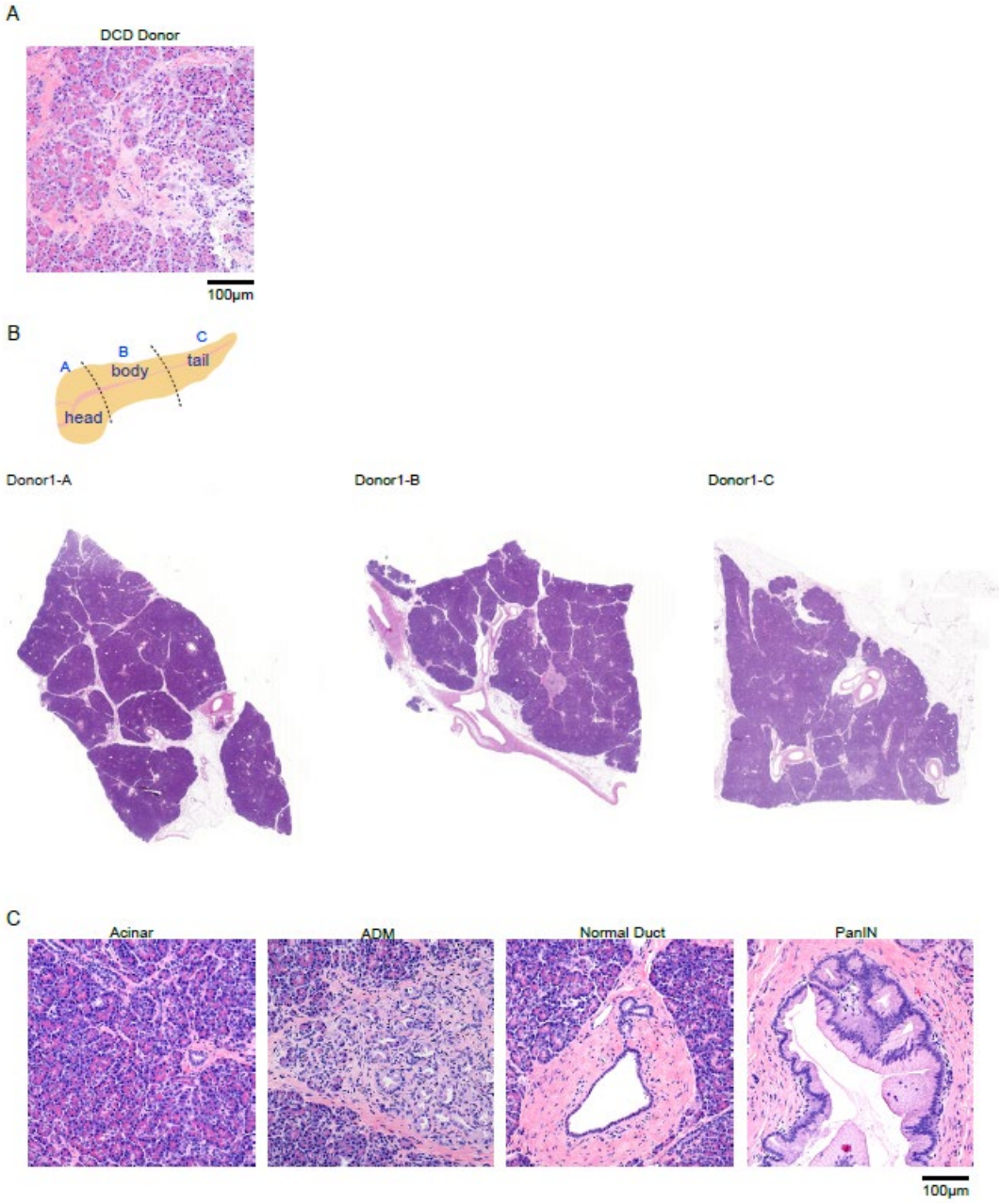


Figure 2.2 Distinct Lesions in adult Pancreas
(A) H&E from a DCD (donation after cardiac death) organ, showing extensive tissue degradation. (B) Representative slide scans from head (left), body (middle), and tail (right) of tissue sections from a donor pancreas. (C) Representative H&E sections of acinar, ADM (acinar-to-ductal metaplasia), normal duct, and PanIN structures in a donor pancreas.

Figure 2.3

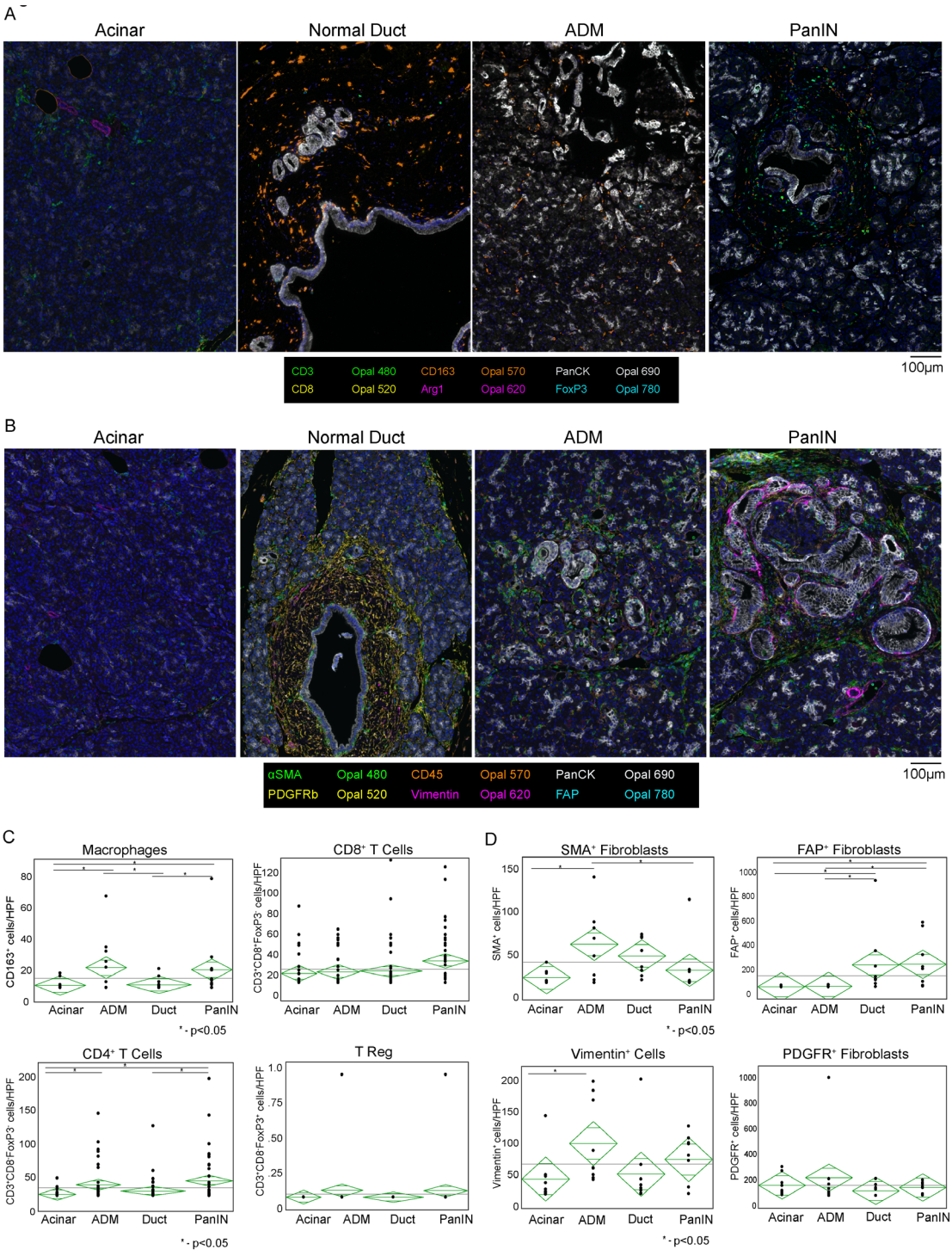

A
Acinar
Normal Duct
ADM
PanIN
CD3 Opal 480 CD163 Opal 570 PanCK Opal 690
CD8 Opal 520 Arg1 Opal 620 FoxP3 Opal 780
100μm
B
Acinar
Normal Duct
ADM
PanIN
αSMA Opal 480 CD45 Opal 570 PanCK Opal 690
PDGFRb Opal 520 Vimentin Opal 620 FAP Opal 780
100μm
C
Macrophages
CD163⁺ cells/HPF
CD8⁺ T Cells
CD3⁺CD8⁺FoxP3⁻ cells/HPF
CD4⁺ T Cells
CD3⁺CD8⁻FoxP3⁺ cells/HPF
T Reg
CD3⁺CD8⁻FoxP3⁺ cells/HPF
Acinar ADM Duct PanIN
* - p<0.05
D
SMA⁺ Fibroblasts
SMA⁺ cells/HPF
FAP⁺ Fibroblasts
FAP⁺ cells/HPF
Vimentin⁺ Cells
Vimentin⁺ cells/HPF
PDGFR⁺ Fibroblasts
PDGFR⁺ cells/HPF
Acinar ADM Duct PanIN
* - p<0.05

Fig 2.3 PanIN lesions in healthy pancreata is surrounded by a unique microenvironment.
(A) mfIHC composite images of formalin-fixed, paraffin-embedded donor tissue specimens, highlighting acinar, normal duct, ADM (acinar-to-ductal), and PanIN structures. Antibodies and colors of immune panel used in the legend below. (B) mfIHC composite images of formalin-fixed, paraffin-embedded donor tissue specimens, highlighting acinar, normal duct, ADM (acinar-to-ductal), and PanIN structures. Antibodies and colors of fibroblast panel used in the legend below. (C) Quantification of percent positive CD3+ cells (top) and CD163+ cells (bottom) surrounding Acinar, ADM, Duct, and PanIN populations, respectively. Asterisks denote a P value of <0.05, as determined by ANOVA. (D) Quantification of percent positive FAP^+ cells (top left) and $FDGFR^+$ cells (bottom left), SMA^+ cells (top right), and $Vimentin^+$ cells (bottom right) surrounding Acinar, ADM, Duct, and PanIN populations, respectively. Asterisks denote a P value of <0.05, as determined by ANOVA.

Figure 2.4

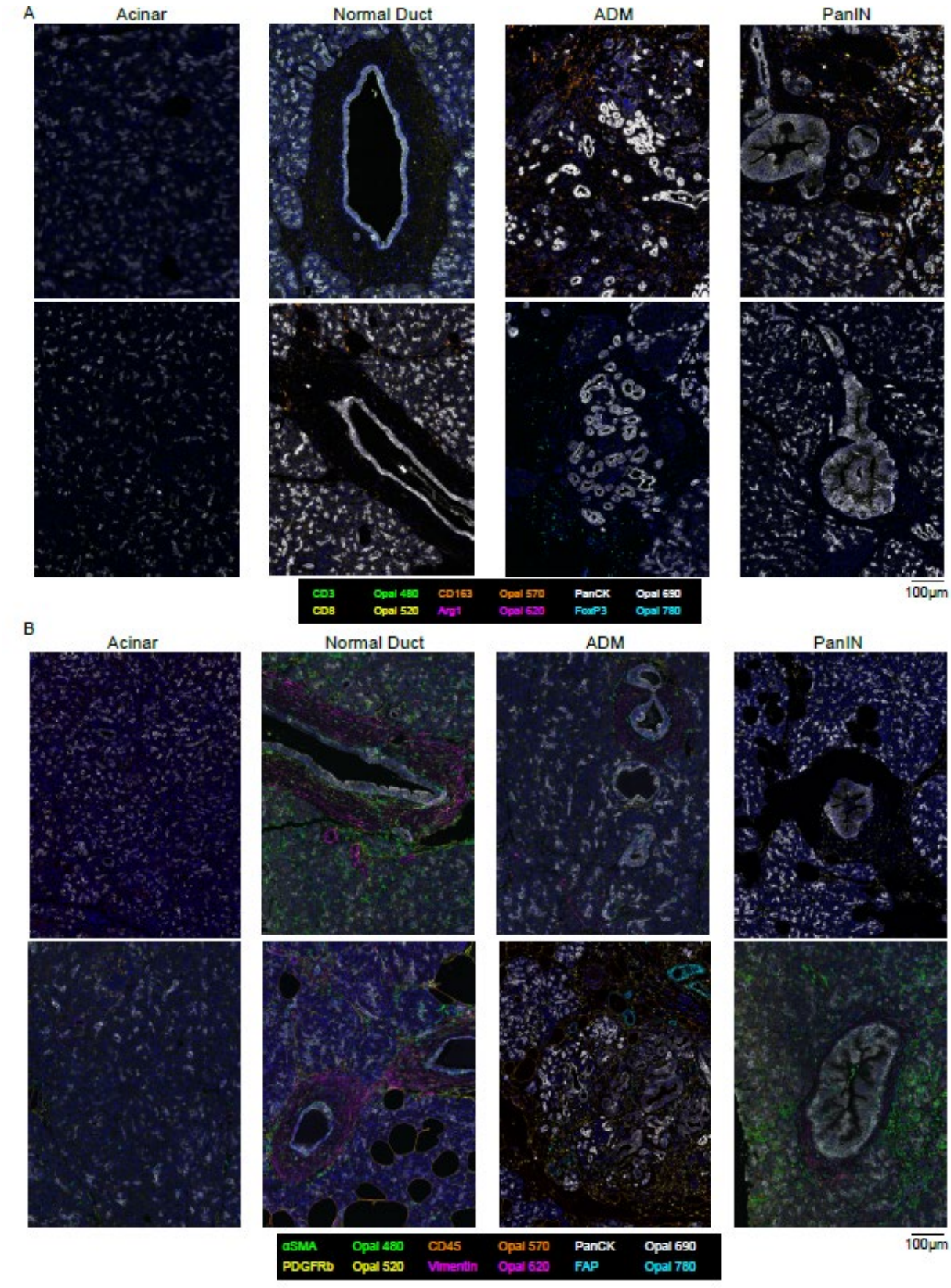

A
Acinar
Normal Duct
ADM
PanIN
CD3
CD8
Opal 480
Opal 520
CD163
Arg1
Opal 570
Opal 620
PanCK
FoxP3
Opal 690
Opal 780
100µm
B
Acinar
Normal Duct
ADM
PanIN
αSMA
PDGFRb
Opal 480
Opal 520
CD45
Vimentin
Opal 570
Opal 620
PanCK
FAP
Opal 690
Opal 780
100µm

Figure 2.4 Multiplex immunohistochemistry staining of donor pancreata
(A) mfIHC composite images of formalin-fixed, paraffin-embedded donor tissue specimens (each row taken from different donor organs), highlighting acinar, normal duct, ADM (acinar-to-ductal), and PanIN structures. Antibodies and colors of immune panel used in the legend below. (B) mfIHC composite images of formalin-fixed, paraffin-embedded donor tissue specimens (each row taken from different donor organs), highlighting acinar, normal duct, ADM (acinar-to-ductal), and PanIN structures. Antibodies and colors of fibroblast panel used in the legend below.

Figure 2.5

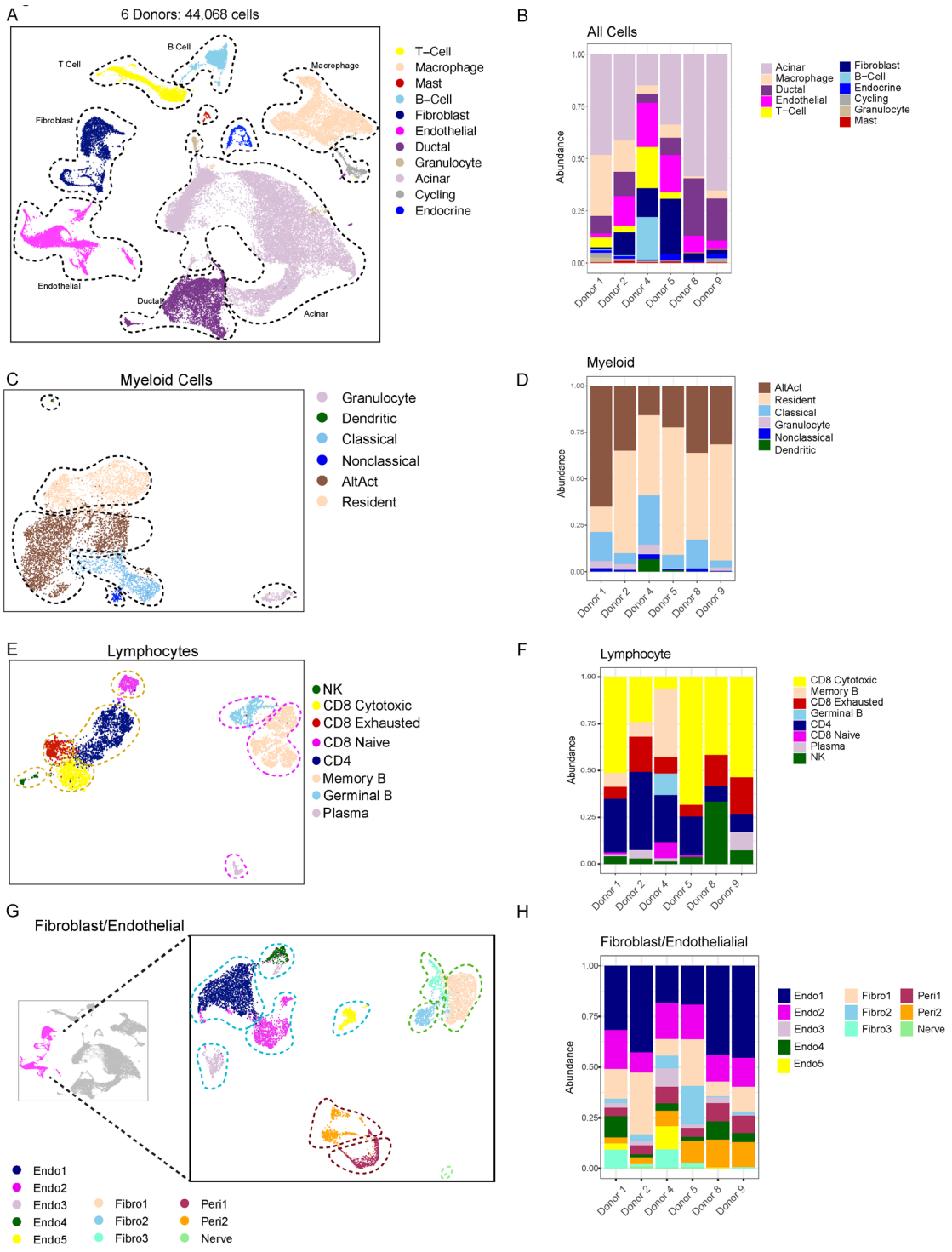

A
6 Donors: 44,068 cells
T Cell
B Cell
Macrophage
Fibroblast
Endothelial
Ductal
Acinar
T–Cell
Macrophage
Mast
B–Cell
Fibroblast
Endothelial
Ductal
Granulocyte
Acinar
Cycling
Endocrine
B
All Cells
Abundance
Donor 1
Donor 2
Donor 4
Donor 5
Donor 8
Donor 9
Acinar
Macrophage
Ductal
Endothelial
T–Cell
Fibroblast
B–Cell
Endocrine
Cycling
Granulocyte
Mast
C
Myeloid Cells
Granulocyte
Dendritic
Classical
Nonclassical
AltAct
Resident
D
Myeloid
AltAct
Resident
Classical
Granulocyte
Nonclassical
Dendritic
E
Lymphocytes
NK
CD8 Cytotoxic
CD8 Exhausted
CD8 Naive
CD4
Memory B
Germinal B
Plasma
F
Lymphocyte
CD8 Cytotoxic
Memory B
CD8 Exhausted
Germinal B
CD4
CD8 Naive
Plasma
NK
G
Fibroblast/Endothelial
Endo1
Endo2
Endo3
Endo4
Endo5
Fibro1
Fibro2
Fibro3
Peri1
Peri2
Nerve
H
Fibroblast/Endothelialial
Endo1
Endo2
Endo3
Endo4
Endo5
Fibro1
Fibro2
Fibro3
Peri1
Peri2
Nerve

Figure 2.5 Healthy pancreata contain several non-epithelial populations, including myeloid, lymphocyte, fibroblast, and endothelial cells
(A) UMAP of all cells captured from single cell RNA sequencing of six donor pancreata. Populations are identified by color. (B) Histogram of cell type abundance of all captured cells by donor. (C) UMAP of extracted myeloid cells from donor pancreata. Populations are identified by color. AltAct = Alternatively Activated Macrophages. (D) Histogram of cell type abundance of specific myeloid cell populations by donor. (E) UMAP of extracted lymphocytes from donor pancreata. Populations are identified by color. (F) Histogram of cell type abundance of specific lymphocyte populations by donor. (G) UMAP of extracted fibroblast, pericyte, and endothelial populations from donor pancreata. Populations are identified by color. (H) Histogram of cell type abundance of specific fibroblast, pericyte, and endothelial populations by donor.

Figure 2.6

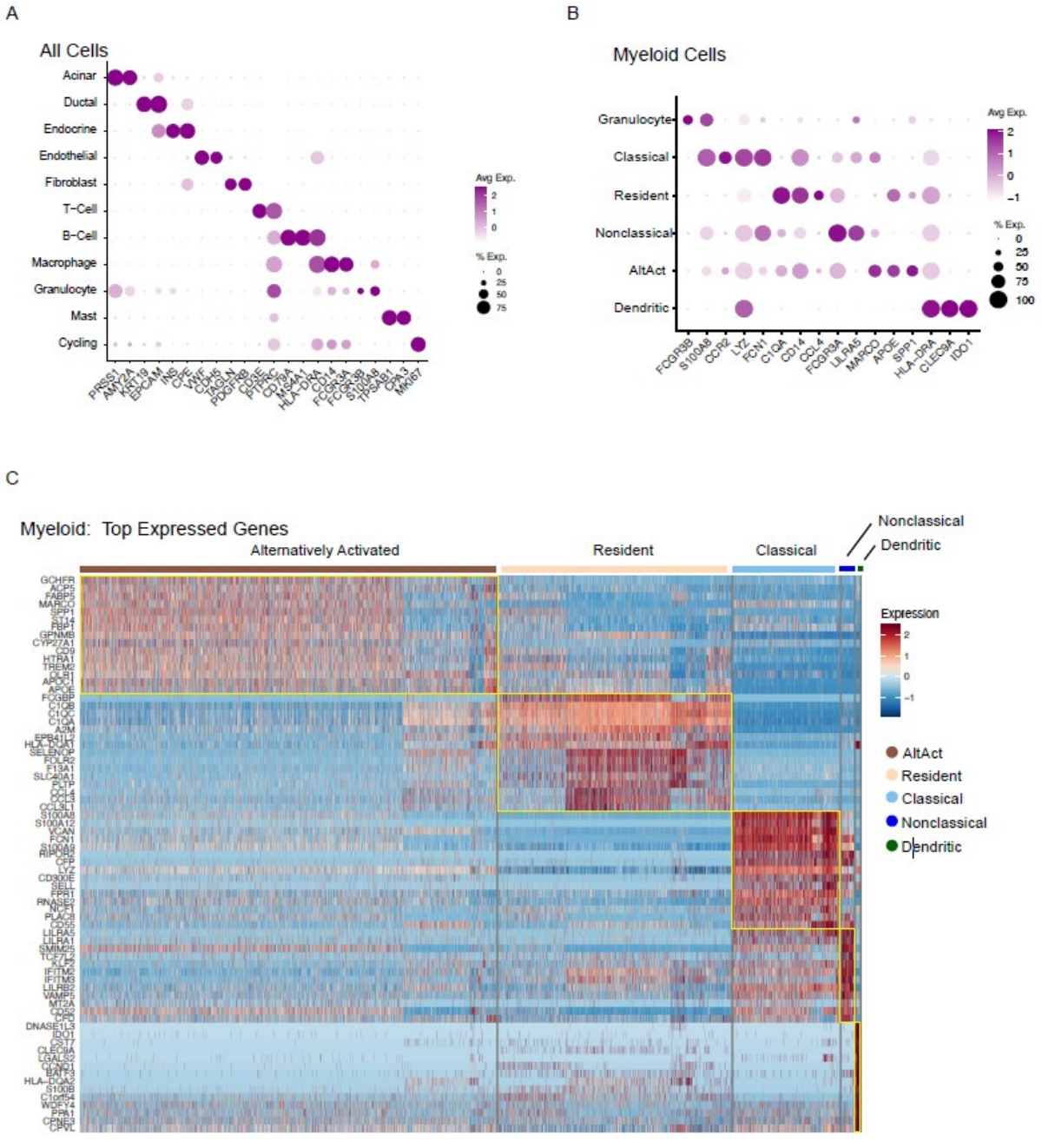


Figure 2.6 Cell linage markers and genes being expressed by myeloid cells
(A) Dotplot showing average expression and percent cells of top expressing markers in each cell cluster. (B) Dotplot showing markers defining different myeloid populations. (C) Single-cell-resolution heatmap of top expressed genes in each myeloid cell population identified.

Figure 2.7

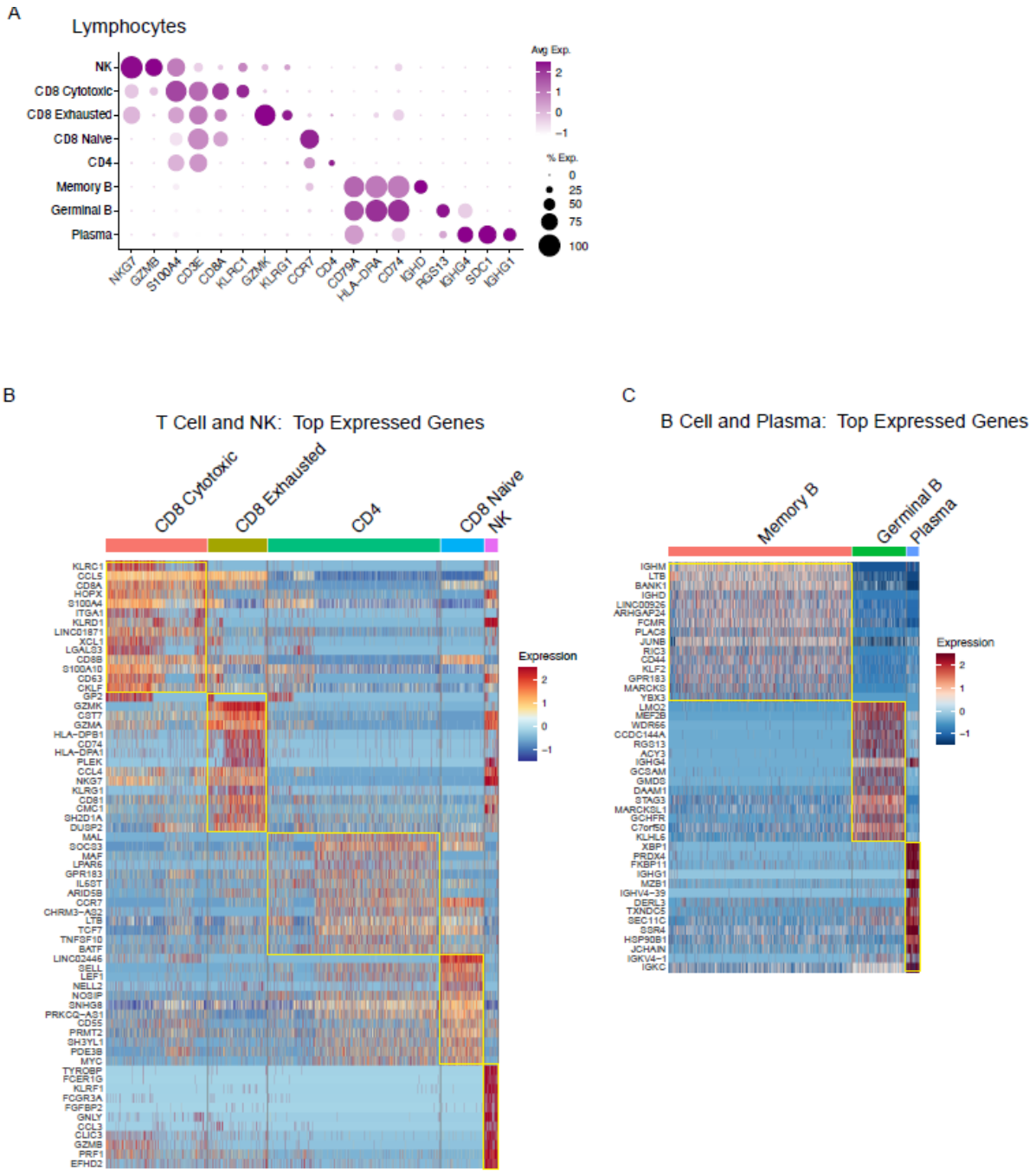


Figure 2.7 Markers and genes being expressed by lymphocytes
(A) Dotplot showing markers defining different lymphocyte populations. (B) Single-cell-resolution heatmap of top expressed genes in each T&NK cell population identified.
C) Single-cell-resolution heatmap of top expressed genes in each B cell and plasma cell population identified.

Figure 2.8

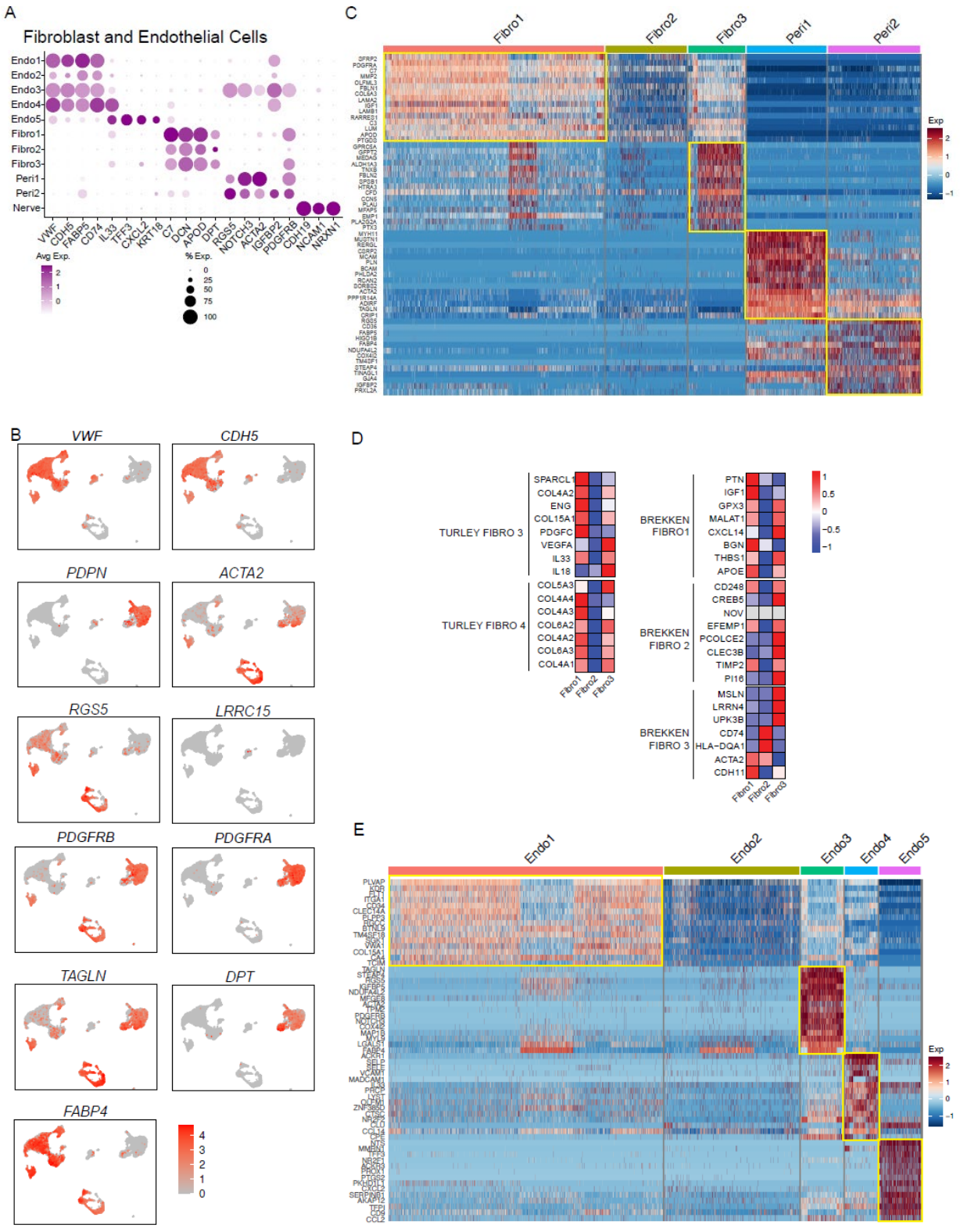

A
Fibroblast and Endothelial Cells
Endo1
Endo2
Endo3
Endo4
Endo5
Fibro1
Fibro2
Fibro3
Peri1
Peri2
Nerve
VWF
CDH5
FABP5
CD74
IL33
TFF3
CXCL2
KRT18
C7
DCN
APOD
DPT
RGS5
NOTCH3
ACTA2
IGFBP2
PDGFRB
CDH19
NCAM1
NRXN1
Avg Exp.
% Exp.
C
Fibro1
Fibro2
Fibro3
Peri1
Peri2
Exp
B
VWF
CDH5
PDPN
ACTA2
RGS5
LRRC15
PDGFRB
PDGFRA
TAGLN
DPT
FABP4
D
TURLEY FIBRO 3
SPARCL1
COL4A2
ENG
COL15A1
PDGFC
VEGFA
IL33
IL18
TURLEY FIBRO 4
COL5A3
COL4A4
COL4A3
COL6A2
COL4A2
COL6A3
COL4A1
BREKKEN FIBRO1
PTN
IGF1
GPX3
MALAT1
CXCL14
BGN
THBS1
APOE
BREKKEN FIBRO 2
CD248
CREB5
NOV
EFEMP1
PCOLCE2
CLEC3B
TIMP2
PI16
BREKKEN FIBRO 3
MSLN
LRRN4
UPK3B
CD74
HLA-DQA1
ACTA2
CDH11
Fibro1
Fibro2
Fibro3
E
Endo1
Endo2
Endo3
Endo4
Endo5
Exp

Figure 2.8 Markers and genes being expressed by Endothelial, Fibroblast and pericyte populations.
(A) Dotplot showing markers defining different populations endothelial, fibroblast, and pericyte populations. (B) Featureplots of select fibroblast and endothelial markers on UMAP of extracted fibroblast, endothelial, and pericyte cells. (C) Single-cell-resolution heatmap of top expressed genes in each fibroblast and pericyte population. (D) Average expression heatmaps of mouse fibroblast gene signatures obtained from literature on the 3 fibroblast populations obtained from healthy pancreas single cell dataset. (E) Single-cell-resolution heatmap of top expressed genes in each endothelial cell population.

Figure 2.9

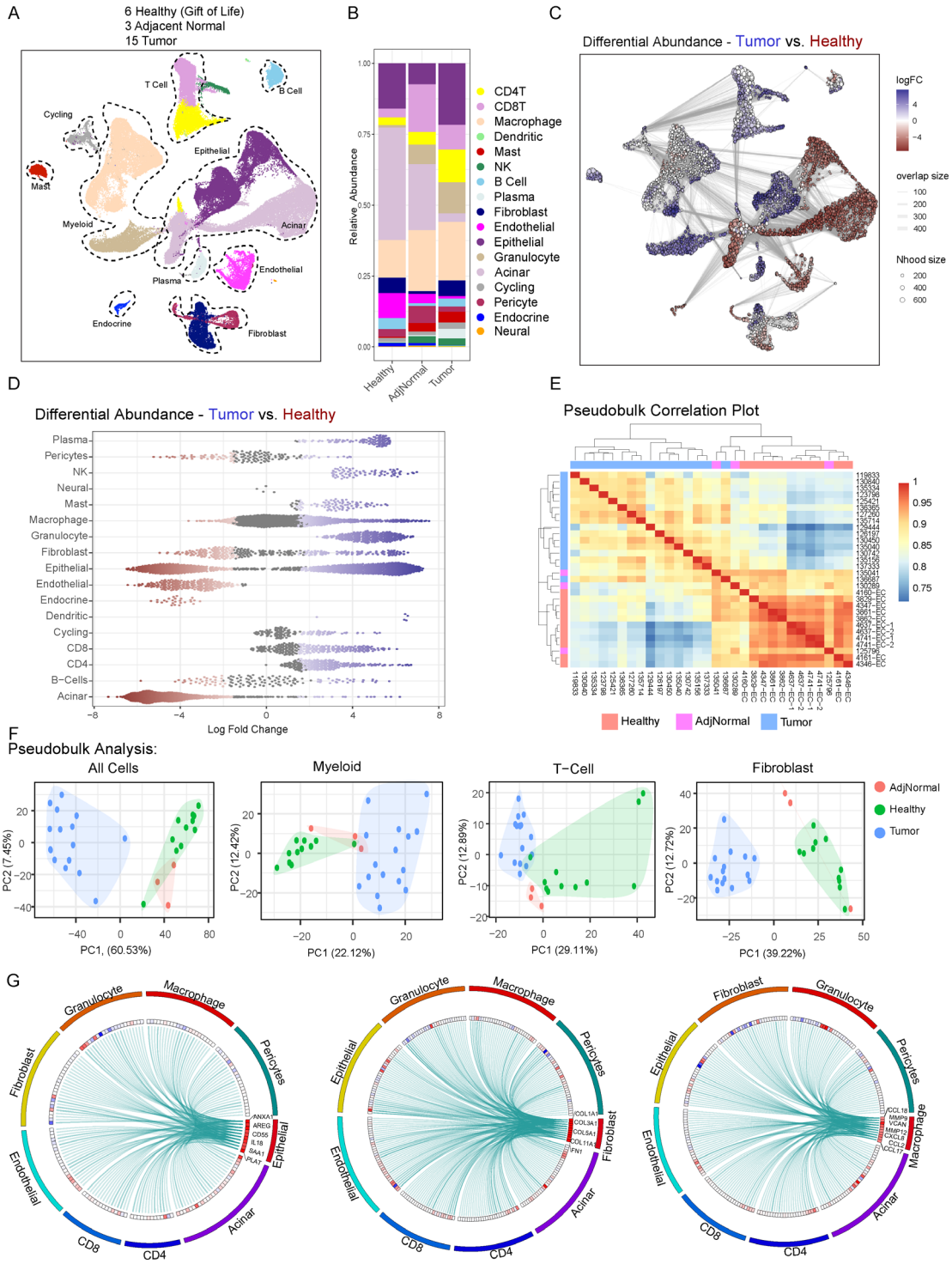

A
6 Healthy (Gift of Life)
3 Adjacent Normal
15 Tumor
T Cell
B Cell
Cycling
Epithelial
Mast
Myeloid
Acinar
Endothelial
Plasma
Endocrine
Fibroblast
B
Relative Abundance
Healthy
AdjNormal
Tumor
CD4T
CD8T
Macrophage
Dendritic
Mast
NK
B Cell
Plasma
Fibroblast
Endothelial
Epithelial
Granulocyte
Acinar
Cycling
Pericyte
Endocrine
Neural
C
Differential Abundance - Tumor vs. Healthy
logFC
overlap size
Nhood size
D
Differential Abundance - Tumor vs. Healthy
Log Fold Change
E
Pseudobulk Correlation Plot
Healthy
AdjNormal
Tumor
F
Pseudobulk Analysis:
All Cells
Myeloid
T−Cell
Fibroblast
PC1, (60.53%)
PC2 (7.45%)
PC1 (22.12%)
PC2 (12.42%)
PC1 (29.11%)
PC2 (12.89%)
PC1 (39.22%)
PC2 (12.72%)
AdjNormal
Healthy
Tumor
G
Granulocyte
Macrophage
Pericytes
Fibroblast
Epithelial
Endothelial
CD8
CD4
Acinar

Figure 2.9 Comparison of the microenvironment in healthy pancreata and pancreatic tumors reveals distinct stromal features.
(A) UMAP of all cells captured from single cell RNA sequencing of six donor pancreata merged with 15 PDAC samples and 3 adjacent normal samples. Populations are identified by color. (B) Histogram of cell type abundance of all cell populations by disease state (healthy, adjacent normal, and tumor). (C) Neighborhood graph differential abundance plot of merged tumor, healthy, and adjacent normal samples. Size of dots represent neighborhoods, while edges represent depict the number of cells shared between neighborhoods. Neighborhoods colored in red represent significantly increased abundance in healthy samples while neighborhoods colored in blue represent significantly increased abudance in tumor samples. (D) Beeswarm plot of differential abundance by cell type. X-axis represents log-fold change in abundance between tumor and healthy states. Each dot is a neighborhood; neighborhoods colored in red represent significnatly increased abundance in healthy samples while neighborhoods colored in blue represent signficantly increased abudance in tumor samples. (E) Correlation heatmap of pseudobulk-aggregrated counts of 15 tumor samples, 3 adjacent normal samples and 11 donor samples (given that single cell sequencing was performed on the head and tail sections separately of 5 out of 6 donors). Each row/line represents one aggregated single cell sequencing sample. (F) PCA plots of pseudobulk-aggregated counts from all cells, myeloid cells, t-cells, and fibroblasts. Each dot represents one aggregated single cell sequencing sample. (G) Circos plots of putative ligand–receptor interactions that are upregulated in PDAC epithelial (left), fibroblast (middle), and macrophage (right) cells compared with healthy cells. The heatmap within the circos plots is the scaled average expression of each gene within PDAC tissue cell populations. The interactions plotted are those in which the expression level of the ligand is increased in PDAC samples compared with healthy tissues.

Figure 2.10

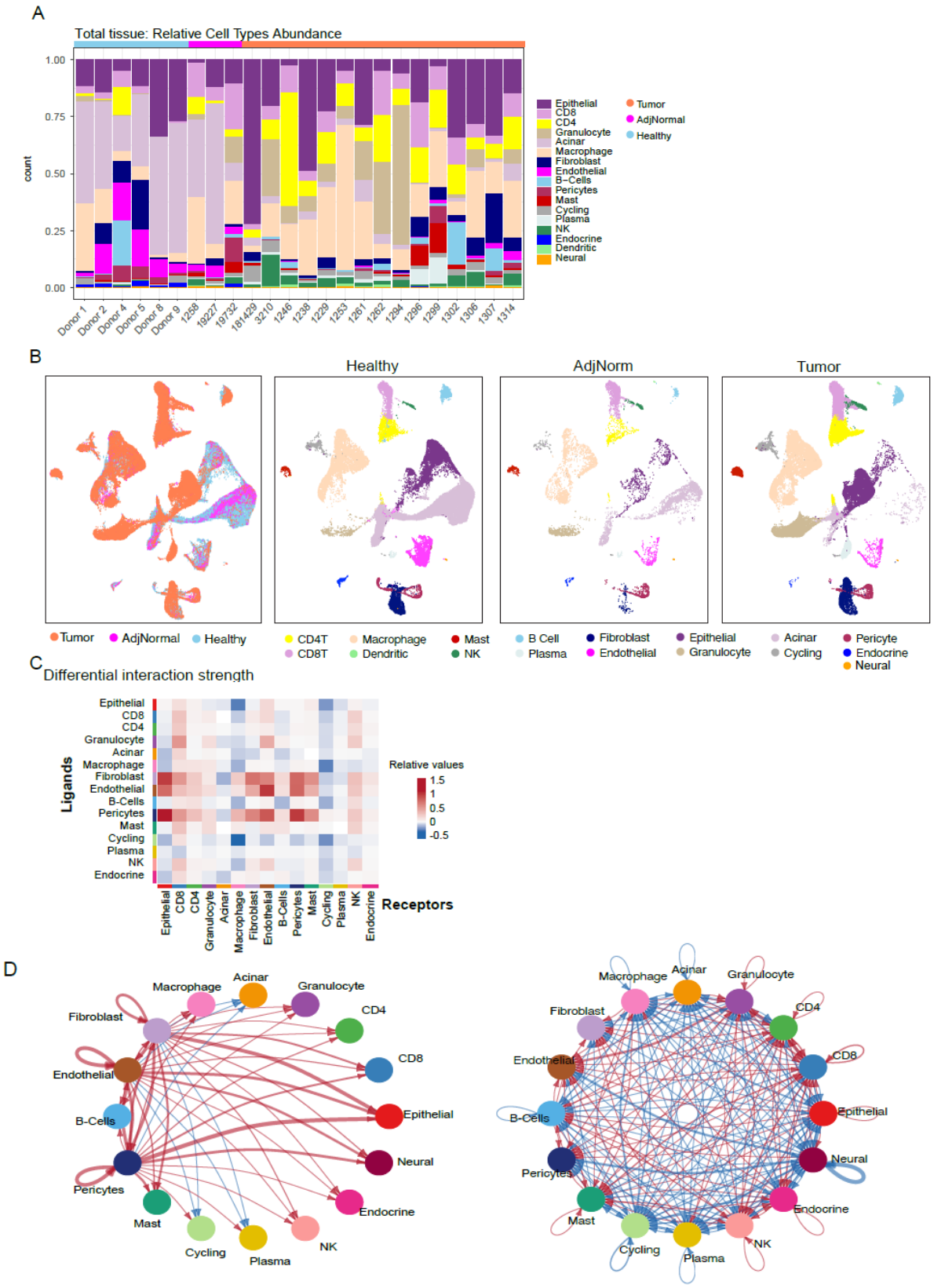

A
Total tissue: Relative Cell Types Abundance
count
Donor 1
Donor 2
Donor 4
Donor 5
Donor 8
Donor 9
1258
19227
19732
181429
3210
1246
1238
1229
1253
1261
1262
1294
1296
1299
1302
1306
1307
1314
Epithelial
CD8
CD4
Granulocyte
Acinar
Macrophage
Fibroblast
Endothelial
B−Cells
Pericytes
Mast
Cycling
Plasma
NK
Endocrine
Dendritic
Neural
Tumor
AdjNormal
Healthy
B
Healthy
AdjNorm
Tumor
Tumor
AdjNormal
Healthy
CD4T
CD8T
Macrophage
Dendritic
Mast
NK
B Cell
Plasma
Fibroblast
Endothelial
Epithelial
Granulocyte
Acinar
Cycling
Pericyte
Endocrine
Neural
C
Differential interaction strength
Ligands
Receptors
Relative values
1.5
1
0.5
0
-0.5
D

Figure 2.10: Cell abundance in Healthy, Adjacent Normal, and Tumor Samples
(A) Histogram of cell type abundance of all cell populations by sample. Blue samples represent healthy samples, magenta samples represent adjacent normal samples, and orange samples represent tumor samples. (B) UMAP overlay of disease states on all cells from single cell dataset of healthy, adjacent normal, and tumor samples. (C) Heatmap of the differential interaction strength comparing tumor samples to healthy samples. Y-axis represents outgoing signaling sent from cell populations while x-axis represents incoming signaling received to cell populations. (D) (left) Circle interaction plot showing differentially outgoing signaling strength upregulated in tumors compared to healthy in fibroblasts, endothelial cells, and pericytes. (right) Circle interaction plot showing differentially outgoing signaling strength upregulated in tumors compared to healthy in all cell types except for fibroblasts, endothelial cells, and pericytes. Red lines indicate increased signaling in tumors, blue lines indicate decreased signaling in tumors.

Figure 2.11

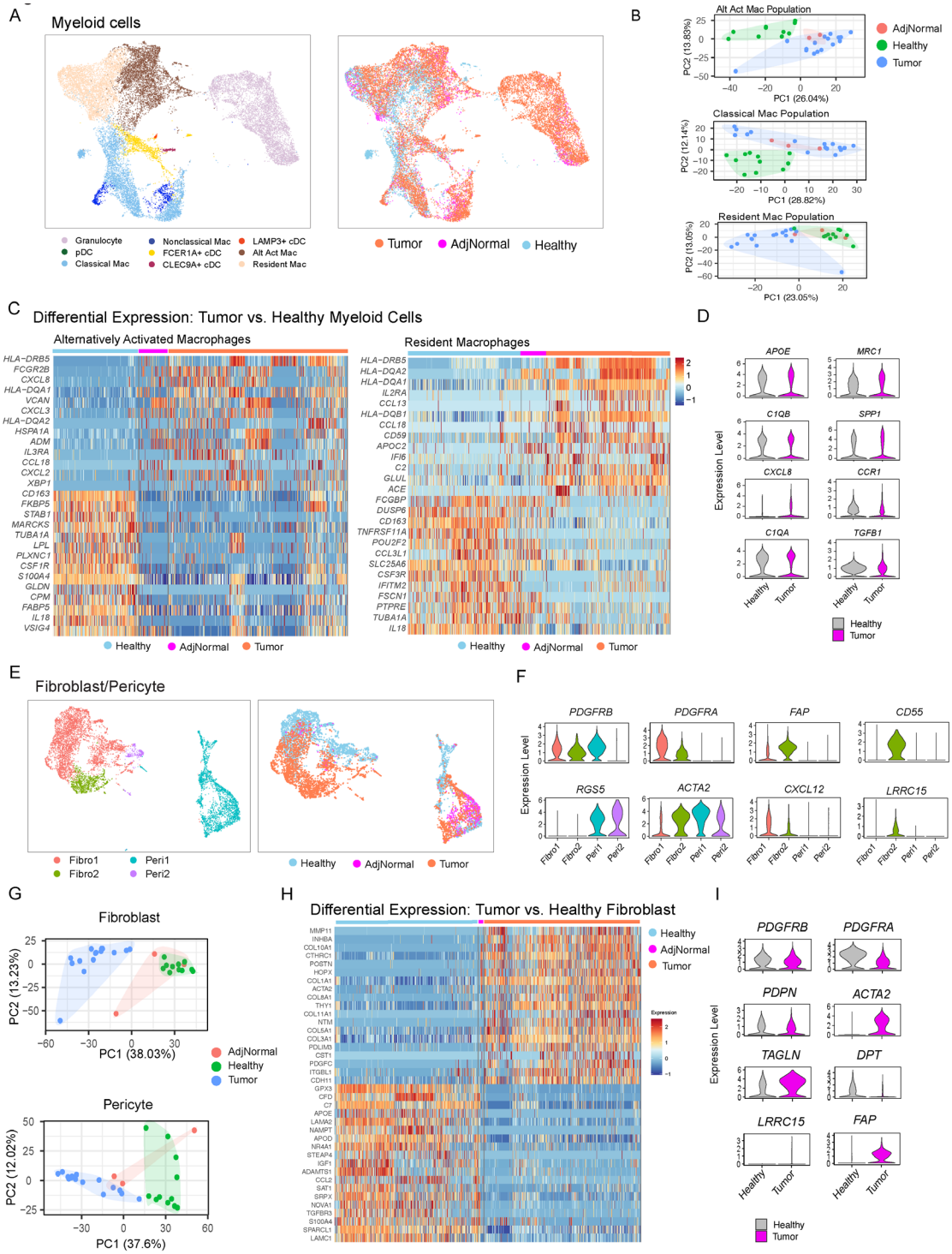

A
Myeloid cells
Granulocyte
pDC
Classical Mac
Nonclassical Mac
FCER1A+ cDC
CLEC9A+ cDC
LAMP3+ cDC
Alt Act Mac
Resident Mac
Tumor
AdjNormal
Healthy
B
Alt Act Mac Population
Classical Mac Population
Resident Mac Population
PC1 (26.04%)
PC2 (13.83%)
PC1 (28.82%)
PC2 (12.14%)
PC1 (23.05%)
PC2 (13.05%)
AdjNormal
Healthy
Tumor
C
Differential Expression: Tumor vs. Healthy Myeloid Cells
Alternatively Activated Macrophages
Resident Macrophages
HLA-DRB5
FCGR2B
CXCL8
HLA-DQA1
VCAN
CXCL3
HLA-DQA2
HSPA1A
ADM
IL3RA
CCL18
CXCL2
XBP1
CD163
FKBP5
STAB1
MARCKS
TUBA1A
LPL
PLXNC1
CSF1R
S100A4
GLDN
CPM
FABP5
IL18
VSIG4
HLA-DRB5
HLA-DQA2
HLA-DQA1
IL2RA
CCL13
HLA-DQB1
CCL18
CD59
APOC2
IFI6
C2
GLUL
ACE
FCGBP
DUSP6
CD163
TNFRSF11A
POU2F2
CCL3L1
SLC25A6
CSF3R
IFITM2
FSCN1
PTPRE
TUBA1A
IL18
Healthy
AdjNormal
Tumor
D
APOE
MRC1
C1QB
SPP1
CXCL8
CCR1
C1QA
TGFB1
Expression Level
Healthy
Tumor
E
Fibroblast/Pericyte
Fibro1
Fibro2
Peri1
Peri2
Healthy
AdjNormal
Tumor
F
PDGFRB
PDGFRA
FAP
CD55
RGS5
ACTA2
CXCL12
LRRC15
Expression Level
Fibro1
Fibro2
Peri1
Peri2
G
Fibroblast
PC1 (38.03%)
PC2 (13.23%)
AdjNormal
Healthy
Tumor
Pericyte
PC1 (37.6%)
PC2 (12.02%)
H
Differential Expression: Tumor vs. Healthy Fibroblast
MMP11
INHBA
COL10A1
CTHRC1
POSTN
HOPX
COL1A1
ACTA2
COL8A1
THY1
COL11A1
NTN1
COL5A1
COL3A1
PDLIM3
CST1
PDGFC
ITGBL1
CDH11
GPX3
CFD
C7
APOE
LAMA2
NAMPT
APOD
NR4A1
STEAP4
IGF1
ADAMTS1
CCL2
SAT1
SRPX
NOVA1
TGFBR3
S100A4
SPARCL1
LAMC1
Healthy
AdjNormal
Tumor
Expression
I
PDGFRB
PDGFRA
PDPN
ACTA2
TAGLN
DPT
LRRC15
FAP
Expression Level
Healthy
Tumor

Figure 2.11 Myeloid and fibroblast populations from tumor-bearing pancreata display distinct transcriptomic signatures compared to their non-tumor counterparts.
(A) (left) UMAP of extracted myeloid cells from single cell dataset of healthy, adjacent normal, and tumor samples. Populations are identified by color. AltAct = Alternatively Activated Macrophages. pDC = Plasmacytoid Dendritic Cells. cDC = Conventional Dendritic Cells. (right) UMAP overlay of disease states on extracted myeloid cells from single cell dataset of healthy, adjacent normal, and tumor samples. (B) PCA plots of pseudobulk-aggregated counts from specific myeloid cell populations Each dot represents one aggregated single cell sequencing sample. (C) Top differentially expressed genes between alternatively activated macrophages (left) and resident macrophages (right) from healthy (blue) and tumor (orange) samples. (D) Violin plots of normalized expression of select tumor-associated macrophage markers comparing healthy to tumor samples. Adjusted p value for significantly differentially expressed markers: *CXCL8* 4.64E-59. (E) (left) UMAP of extracted fibroblast and pericyte cells from single cell dataset of healthy, adjacent normal, and tumor samples. Populations are identified by color. (right) UMAP overlay of disease states on extracted fibroblast/pericyte cells from single cell dataset of healthy, adjacent normal, and tumor samples. (F) Violin plots of normalized expression of select fibroblast markers mapped across fibroblast and pericyte populations. Adjusted p value for significantly differentially expressed markers: *PDGFRA* 1.58E-308, *ACTA2* 1.85E-261, *TAGLN* 1.18E-117, *DPT* 2.00E-67, *FAP* 3.63E-308. (G) PCA plots of pseudobulk-aggregated counts from fibroblast (top) and pericyte (bottom) populations Each dot represents one aggregated single cell sequencing sample. (H) Top differentially expressed genes between fibroblasts from healthy (blue) and tumor (orange) samples. (I) Violin plots of normalized expression of select fibroblast markers comparing healthy to tumor samples.

Figure 2.12

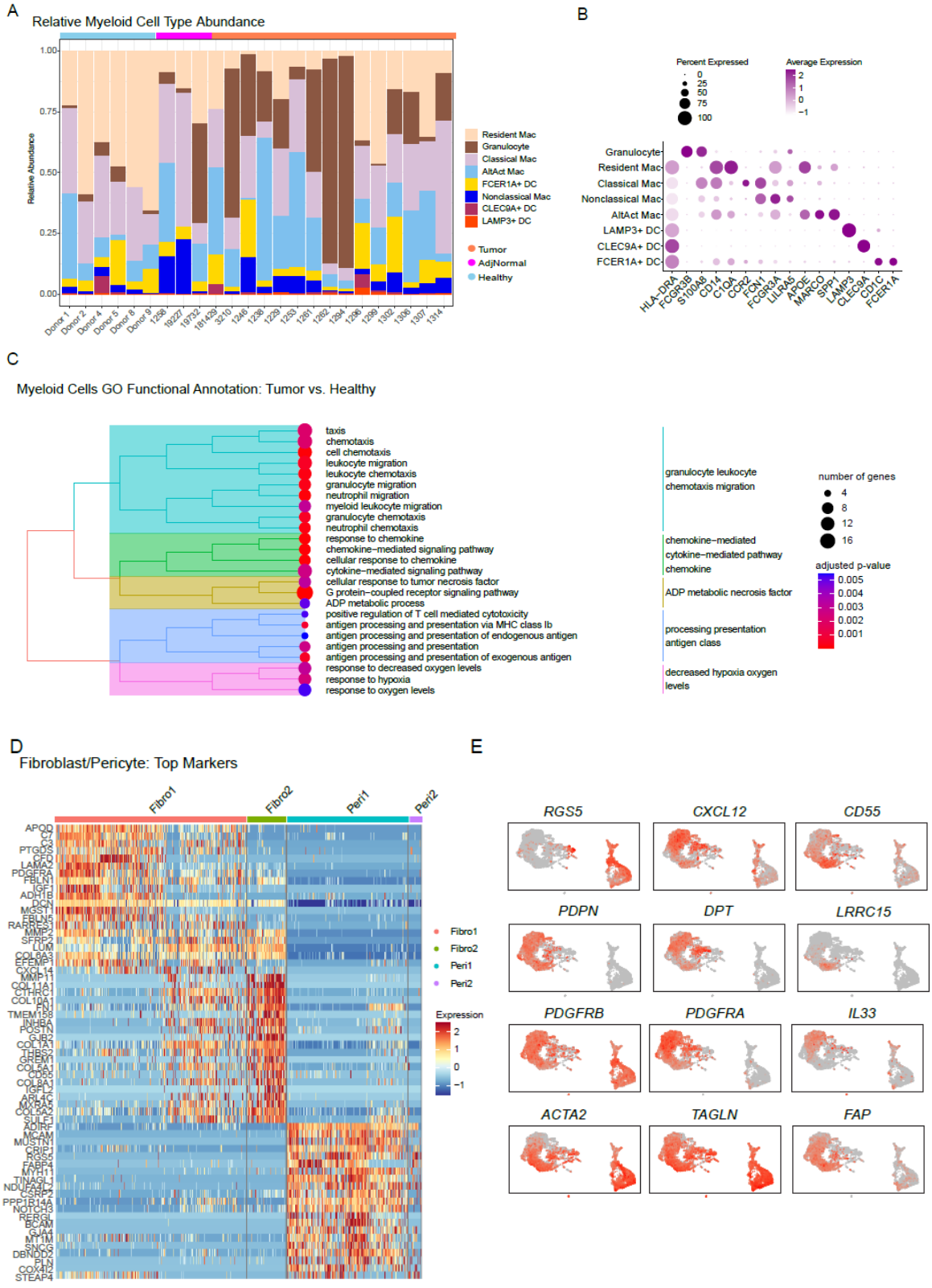

A
Relative Myeloid Cell Type Abundance
Relative Abundance
Resident Mac
Granulocyte
Classical Mac
AltAct Mac
FCER1A+ DC
Nonclassical Mac
CLEC9A+ DC
LAMP3+ DC
Tumor
AdjNormal
Healthy
B
Percent Expressed
Average Expression
Granulocyte
Resident Mac
Classical Mac
Nonclassical Mac
AltAct Mac
LAMP3+ DC
CLEC9A+ DC
FCER1A+ DC
HLA-DRA
FCGR3B
S100A8
CD14
C1QA
CCR2
FCN1
FCGR3A
LILRA5
APOE
MARCO
SPP1
LAMP3
CLEC9A
CD1C
FCER1A
C
Myeloid Cells GO Functional Annotation: Tumor vs. Healthy
taxis
chemotaxis
cell chemotaxis
leukocyte migration
leukocyte chemotaxis
granulocyte migration
neutrophil migration
myeloid leukocyte migration
granulocyte chemotaxis
neutrophil chemotaxis
response to chemokine
chemokine−mediated signaling pathway
cellular response to chemokine
cytokine−mediated signaling pathway
cellular response to tumor necrosis factor
G protein−coupled receptor signaling pathway
ADP metabolic process
positive regulation of T cell mediated cytotoxicity
antigen processing and presentation via MHC class Ib
antigen processing and presentation of endogenous antigen
antigen processing and presentation
antigen processing and presentation of exogenous antigen
response to decreased oxygen levels
response to hypoxia
response to oxygen levels
granulocyte leukocyte chemotaxis migration
chemokine−mediated cytokine−mediated pathway chemokine
ADP metabolic necrosis factor
processing presentation antigen class
decreased hypoxia oxygen levels
number of genes
adjusted p-value
D
Fibroblast/Pericyte: Top Markers
Fibro1
Fibro2
Peri1
Peri2
Expression
E
RGS5
CXCL12
CD55
PDPN
DPT
LRRC15
PDGFRB
PDGFRA
IL33
ACTA2
TAGLN
FAP

Figure 2.12 Myeloid and Fibroblast cell abundance in Healthy, Adjacent Normal, and Tumor Samples
(A) Histogram of cell type abundance of myeloid populations by sample. Blue samples represent healthy samples, magenta samples represent adjacent normal samples, and orange samples represent tumor samples. (B) Dotplot showing markers defining myeloid populations. (C) Tree plot of gene ontology functional annotation on pseudobulk aggregated tumor myeloid cells vs. healthy myeloid cells. Dot size represents number of genes in each pathway, and color bar represents adjusted p-value. (D) Single-cell-resolution heatmap of top expressed genes in fibroblast/pericyte populations in merged healthy and tumor samples. (E) Feature plots of select fibroblast markers on UMAP of extracted fibroblast and pericyte cells from merged healthy and tumor samples.

Figure 2.13

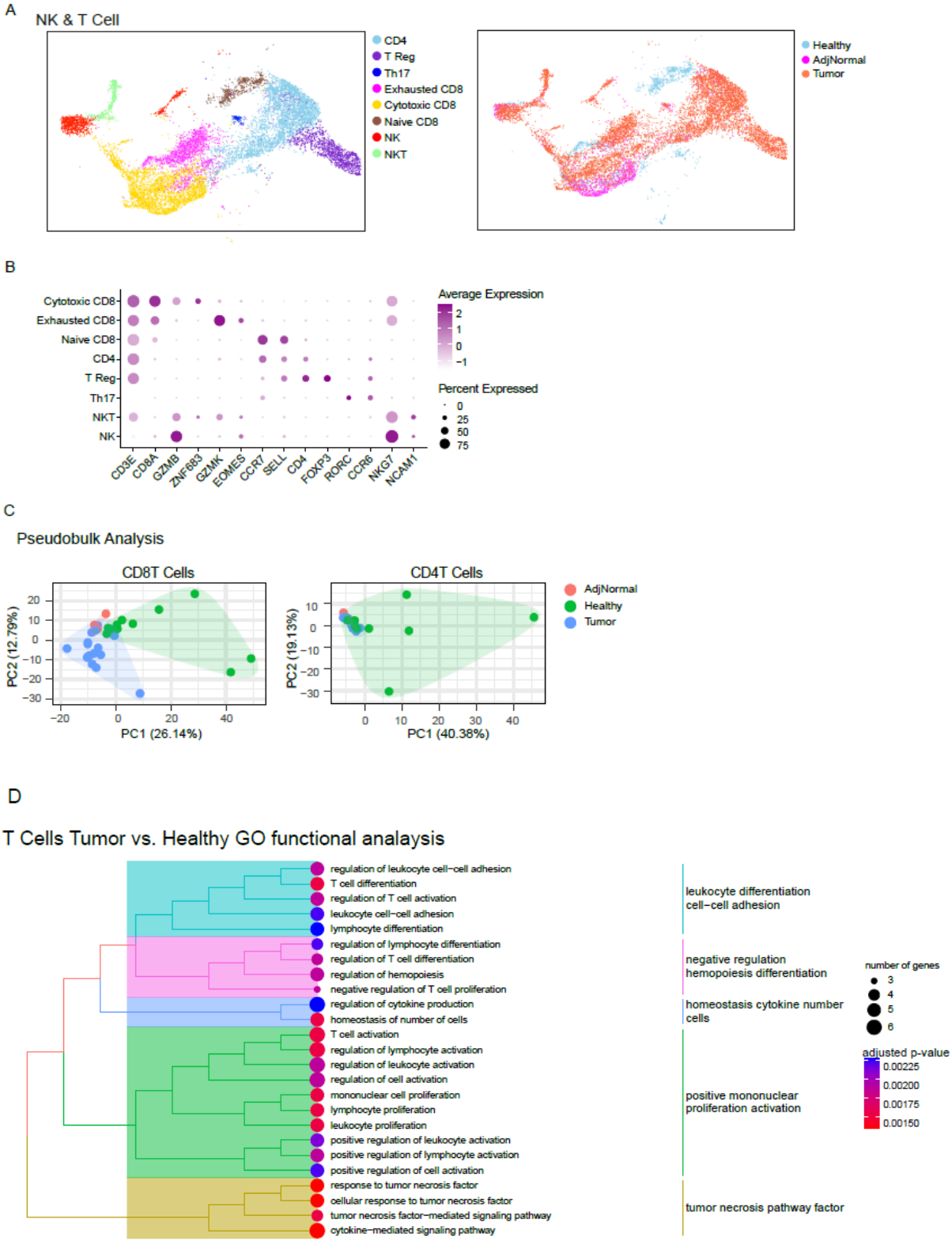

A
NK & T Cell
CD4
T Reg
Th17
Exhausted CD8
Cytotoxic CD8
Naive CD8
NK
NKT
Healthy
AdjNormal
Tumor
B
Cytotoxic CD8
Exhausted CD8
Naive CD8
CD4
T Reg
Th17
NKT
NK
CD3E
CD8A
GZMB
ZNF683
GZMK
EOMES
CCR7
SELL
CD4
FOXP3
RORC
CCR6
NKG7
NCAM1
Average Expression
Percent Expressed
C
Pseudobulk Analysis
CD8T Cells
CD4T Cells
PC2 (12.79%)
PC1 (26.14%)
PC2 (19.13%)
PC1 (40.38%)
AdjNormal
Healthy
Tumor
D
T Cells Tumor vs. Healthy GO functional analaysis
regulation of leukocyte cell−cell adhesion
T cell differentiation
regulation of T cell activation
leukocyte cell−cell adhesion
lymphocyte differentiation
regulation of lymphocyte differentiation
regulation of T cell differentiation
regulation of hemopoiesis
negative regulation of T cell proliferation
regulation of cytokine production
homeostasis of number of cells
T cell activation
regulation of lymphocyte activation
regulation of leukocyte activation
regulation of cell activation
mononuclear cell proliferation
lymphocyte proliferation
leukocyte proliferation
positive regulation of leukocyte activation
positive regulation of lymphocyte activation
positive regulation of cell activation
response to tumor necrosis factor
cellular response to tumor necrosis factor
tumor necrosis factor−mediated signaling pathway
cytokine−mediated signaling pathway
leukocyte differentiation
cell−cell adhesion
negative regulation
hemopoiesis differentiation
homeostasis cytokine number
cells
positive mononuclear
proliferation activation
tumor necrosis pathway factor
number of genes
adjusted p-value

Figure 2.13 Activated pathways in T cells from Healthy and Tumor samples
(A) (left) UMAP of extracted NK and T cell s from single cell dataset of healthy, adjacent normal, and tumor samples. Populations are identified by color. (right) UMAP overlay of disease states on extracted fibroblast/pericyte cells from single cell dataset of healthy, adjacent normal, and tumor samples. (B) Dotplot showing markers defining NK and T populations. (C) PCA plots of pseudobulk-aggregated counts from all cells, myeloid cells, t-cells, and fibroblasts. Each dot represents one aggregated single cell sequencing sample. (D) Treeplot of gene ontology functional annotation on pseudobulk aggregated tumor T cells vs. healthy T cells. Dot size represents number of genes in each pathway, and color bar represents adjusted p-value.

Figure 2.14

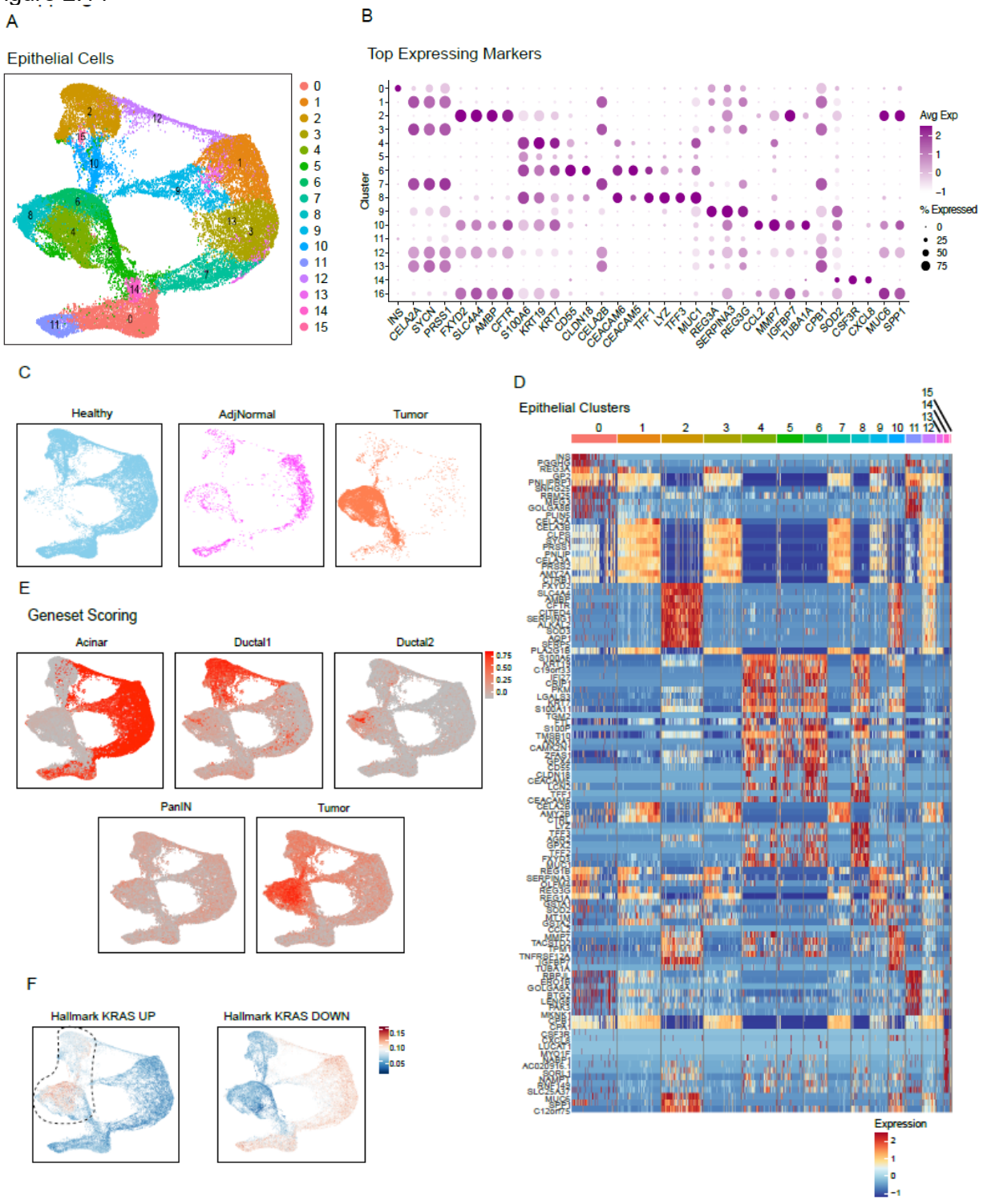

A
Epithelial Cells
0
1
2
3
4
5
6
7
8
9
10
11
12
13
14
15
B
Top Expressing Markers
Cluster
INS
CELA2A
SYCN
PRSS1
FXYD2
SLC4A4
AMBP
CFTR
S100A6
KRT19
KRT7
CD55
CLDN18
CELA2B
CEACAM6
CEACAM5
TFF1
LYZ
TFF3
MUC1
REG3A
SERPINA3
REG3G
CCL2
MMP7
IGFBP7
TUBA1A
CPB1
SOD2
CSF3R
CXCL8
MUC6
SPP1
Avg Exp
% Expressed
C
Healthy
AdjNormal
Tumor
D
Epithelial Clusters
Expression
E
Geneset Scoring
Acinar
Ductal1
Ductal2
PanIN
Tumor
F
Hallmark KRAS UP
Hallmark KRAS DOWN

Figure 2.14 Distinct Epithelial cells in Healthy, Adjacent normal, and Tumor samples
(A) UMAP of extracted epithelial cells from single cell dataset of healthy, adjacent normal, and tumor samples. Numbers represent unbiased clustering. (B) Dotplot of top expressed markers in each of the epithelial clusters. (C) UMAP split by disease states on extracted epithelial cells from single cell dataset of healthy, adjacent normal, and tumor samples. (D) Single cell resolution heatmap of top expressed markers in each unbiased epithelial cluster. (E) AUCell geneset scoring mapped to epithelial single cell dataset of healthy, adjacent normal, and tumor samples using previously reported acinar, ductal, PanIN, and tumor gene signatures. (F) KRAS activity score mapped to epithelial single cell dataset of healthy, adjacent normal, and tumor samples utilizing previously reported hallmark genesets.

Figure 2.15

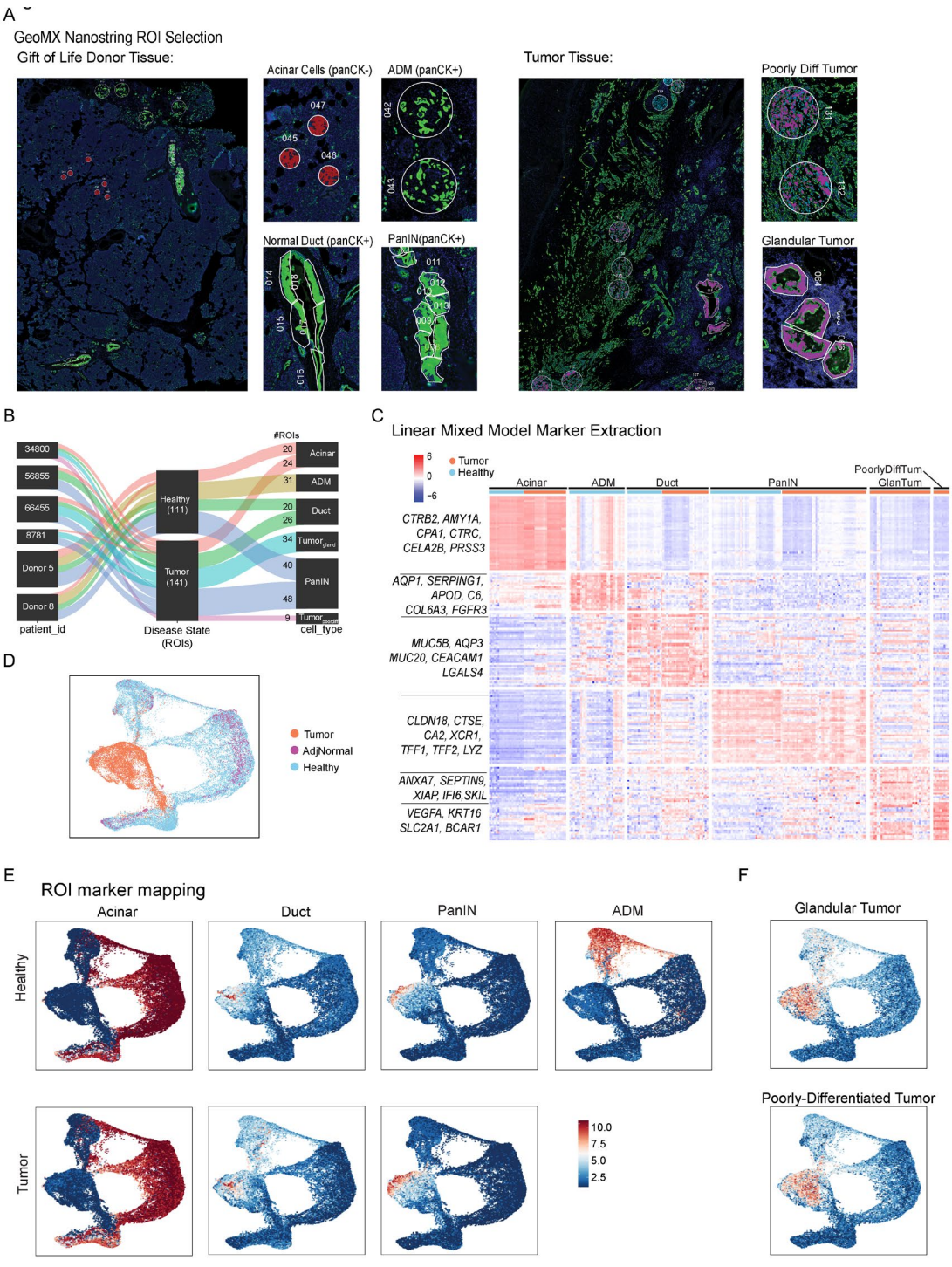

A
GeoMX Nanostring ROI Selection
Gift of Life Donor Tissue:
Acinar Cells (panCK-)
ADM (panCK+)
Normal Duct (panCK+)
PanIN(panCK+)
Tumor Tissue:
Poorly Diff Tumor
Glandular Tumor
B
#ROIs
patient_id
Disease State (ROIs)
cell_type
Healthy (111)
Tumor (141)
Acinar
ADM
Duct
PanIN
C
Linear Mixed Model Marker Extraction
Tumor
Healthy
Acinar
ADM
Duct
PanIN
PoorlyDiffTum
GlanTum
CTRB2, AMY1A, CPA1, CTRC, CELA2B, PRSS3
AQP1, SERPING1, APOD, C6, COL6A3, FGFR3
MUC5B, AQP3 MUC20, CEACAM1 LGALS4
CLDN18, CTSE, CA2, XCR1, TFF1, TFF2, LYZ
ANXA7, SEPTIN9, XIAP, IFI6,SKIL
VEGFA, KRT16 SLC2A1, BCAR1
D
Tumor
AdjNormal
Healthy
E
ROI marker mapping
Acinar
Duct
PanIN
ADM
Healthy
Tumor
10.0
7.5
5.0
2.5
F
Glandular Tumor
Poorly-Differentiated Tumor

Figure 2.15 Spatial transcriptomics reveals a unique epithelial gene signature of PanIN lesions which aligns closely with tumor epithelium.
(A) (Left) GeoMX tissue section from donor pancreas, stained for panCK and CD45. panCK^{+} segments were pseudo-colored in green, while panCK^{-}CD45^{-} segments were pseudo-colored in red. (Right) GeoMX tissue section from surgically resected treatment-naïve PDAC, stained for panCK and CD45. panCK^{+} segments were pseudo-colored in purple. (B) Sankey plot showing distribution of ROIs amount donor or PDAC samples. (C) Heatmap of cell-type specific markers derived from differential gene expression using the linear mixed model on spatial transcriptomic ROIs.
(D) UMAP overlay of disease states on extracted epithelial cells from single cell dataset of healthy, adjacent normal, and tumor samples. (E) AUCell geneset scoring mapped to epithelial single cell dataset of healthy, adjacent normal, and tumor samples using signatures derived from Acinar, Normal Duct, PanIN, and ADM (acinar to ductal metaplasia) spatial transcriptomic ROIs. Top row represents spatial transcriptomic signatures obtained from healthy tissue; bottom row represents spatial transcriptomic signatures obtained from tumor tissue. (F) AUCell geneset scoring mapped to epithelial single cell dataset of healthy, adjacent normal, and tumor samples using signatures derived from glandular tumor and poorly differentiated tumor ROIs.

Figure 2.16

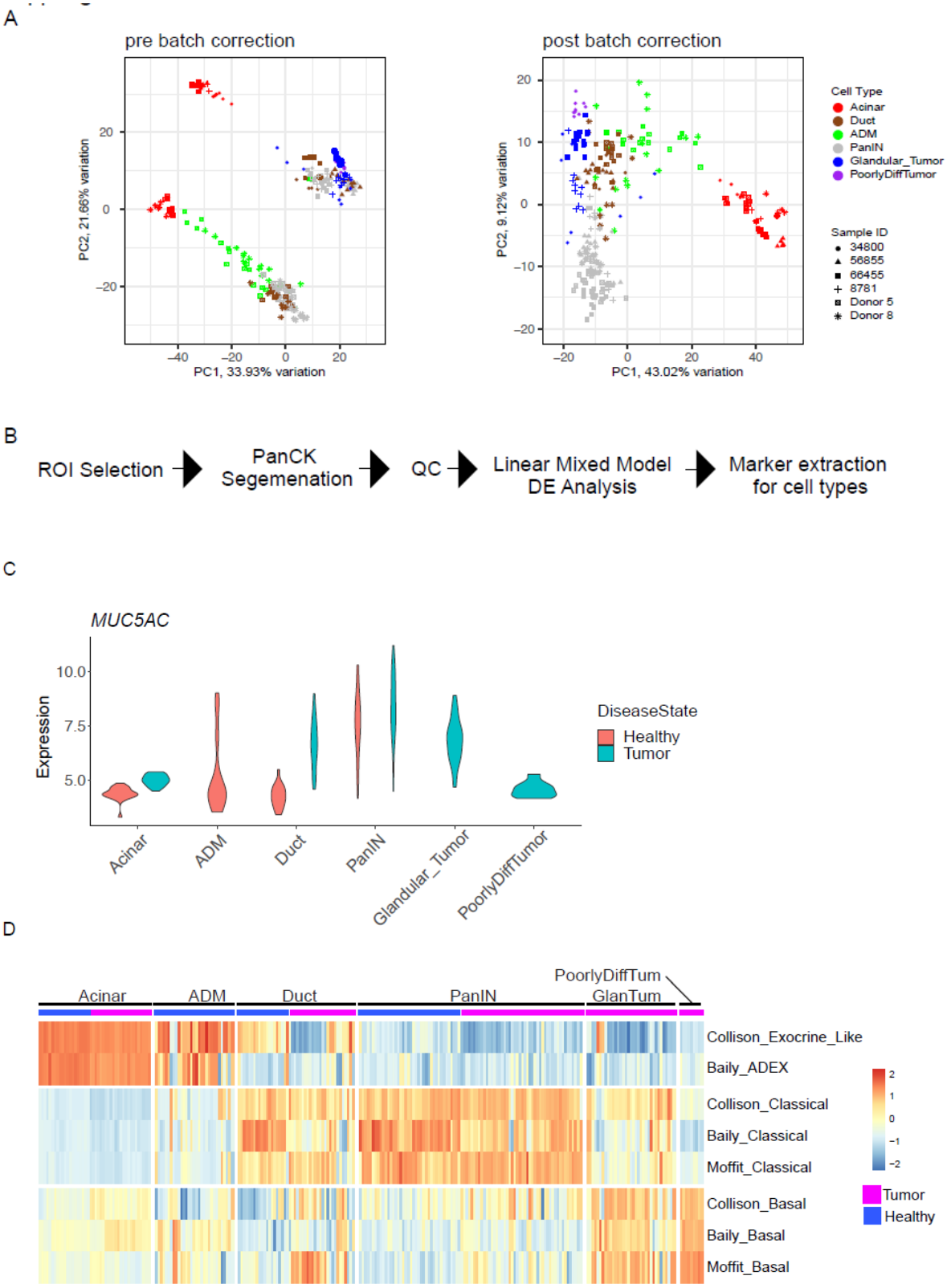

A
pre batch correction
post batch correction
PC2, 21.66% variation
PC1, 33.93% variation
PC2, 9.12% variation
PC1, 43.02% variation
Cell Type
Acinar
Duct
ADM
PanIN
Glandular_Tumor
PoorlyDiffTumor
Sample ID
34800
56855
66455
8781
Donor 5
Donor 8
B
ROI Selection
PanCK Segemenation
QC
Linear Mixed Model DE Analysis
Marker extraction for cell types
C
MUC5AC
Expression
DiseaseState
Healthy
Tumor
Acinar
ADM
Duct
PanIN
Glandular_Tumor
PoorlyDiffTumor
D
Acinar
ADM
Duct
PanIN
PoorlyDiffTum
GlanTum
Collison_Exocrine_Like
Baily_ADEX
Collison_Classical
Baily_Classical
Moffit_Classical
Collison_Basal
Baily_Basal
Moffit_Basal
Tumor
Healthy

Figure 2.16 Classification of the epithelial cells
(A) PCA plot of all segmented ROIs (each dot represents one ROI) pre- and post- batch correction. (B) Scheme for workflow of spatial trancriptomics analysis. (C) Violin plot of MUC5AC expression in spatial ROIs by cell type and disease state. (D) Heatmap of geneset enrichiment score using GSVA of Exocrine_like, ADEX, Classical, and Basal subyptes.

Figure 2.17

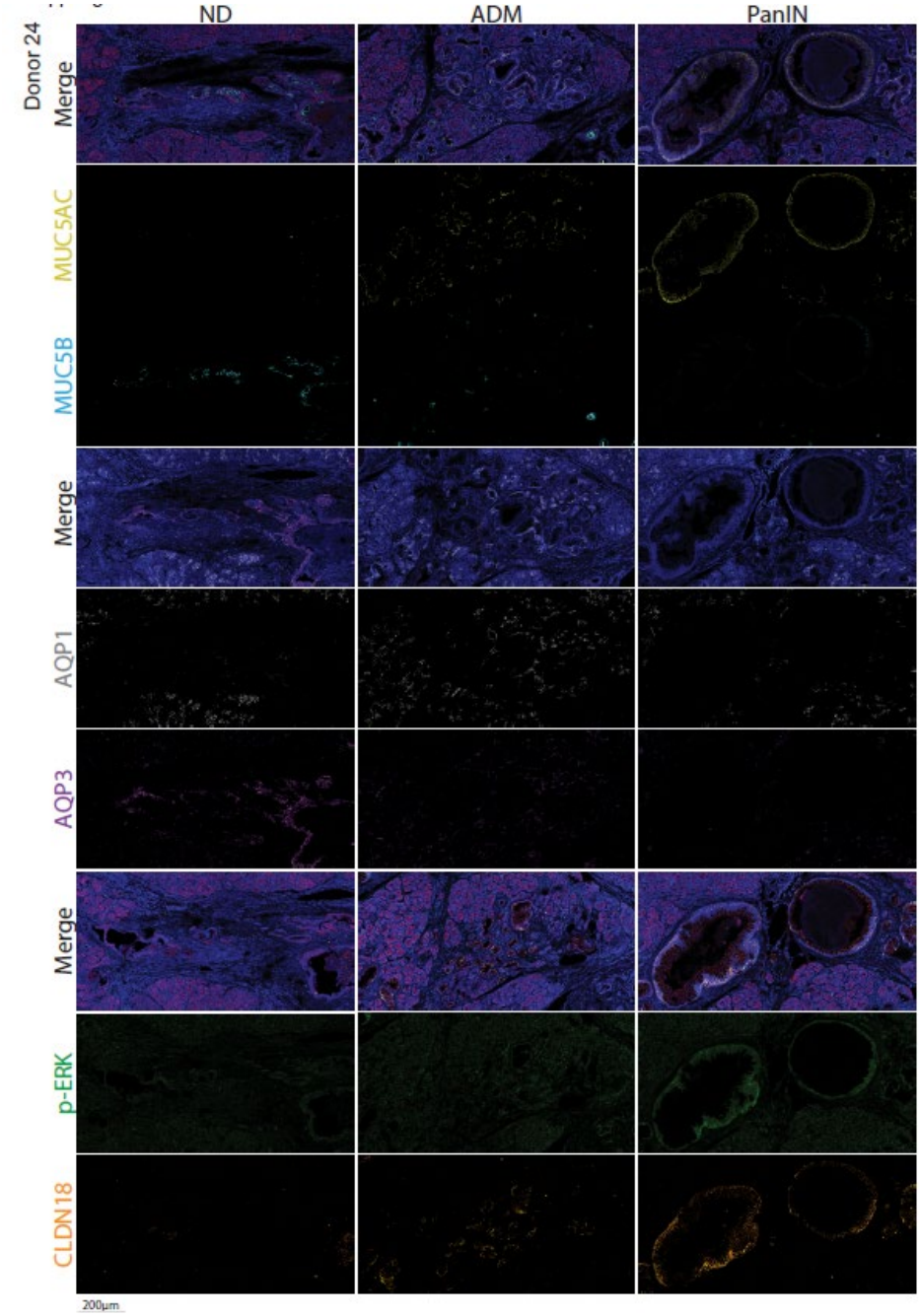


Figure 2.17 Immunofluorescence staining of Epithelial markers-Donor 24
Immunofluorescence staining of serial sections of normal duct (ND), ADM, and PanIN lesions found in donor tissue. In order from top row to bottom row: Merged co-IF of E-Cadherin (red), MUC5AC (yellow) and MUC5B (blue). Single channel of MUC5AC staining. Single channel of MUC5B staining. Merge of co-IF of AQP1 (grey) and AQP3 (purple). Single channel of AQP1 staining. Single channel of AQP3 staining. Merge of co-IF of p-ERK (green), E-Cadherin (red) and CLDN18 (orange). Single channel of p- ERK staining. Single channel of CLDN18 staining.

Figure 2.18

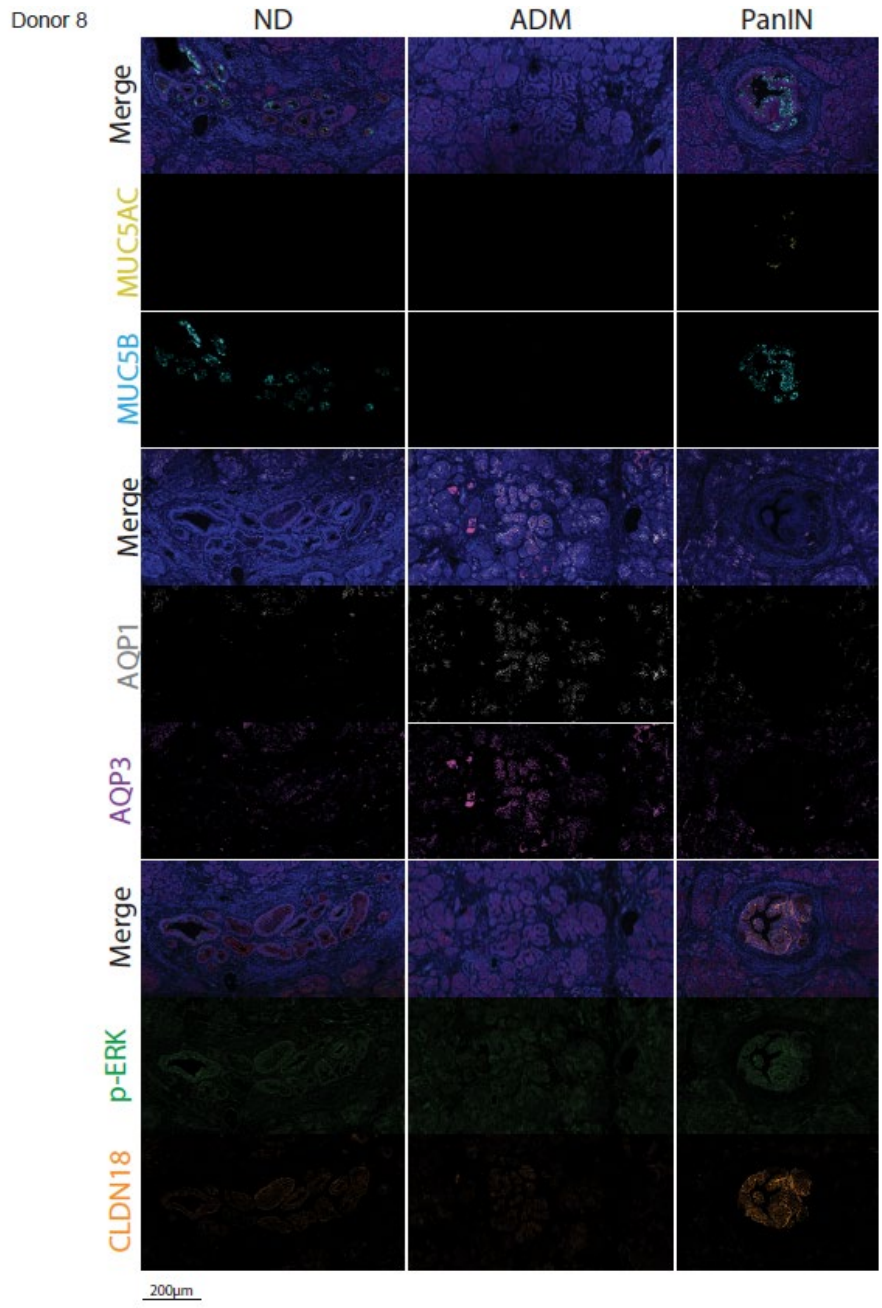


Figure 2.18 Immunofluorescence staining of Epithelial markers-Donor 8
Immunofluorescence staining of serial sections of normal duct (ND), ADM with PanIN transformation, and PanIN lesions found in donor tissue. In order from top row to bottom row: Merged co-IF of ECadherin (red), MUC5AC (yellow) and MUC5B (blue). Single channel of MUC5AC staining. Single channel of MUC5B staining. Merge of co-IF of AQP1 (grey) and AQP3 (purple). Single channel of AQP1 staining. Single channel of AQP3 staining. Merge of co-IF of p-ERK (green), E-Cadherin (red) and CLDN18 (orange). Single channel of p-ERK staining. Single channel of CLDN18 staining.

Figure 2.19

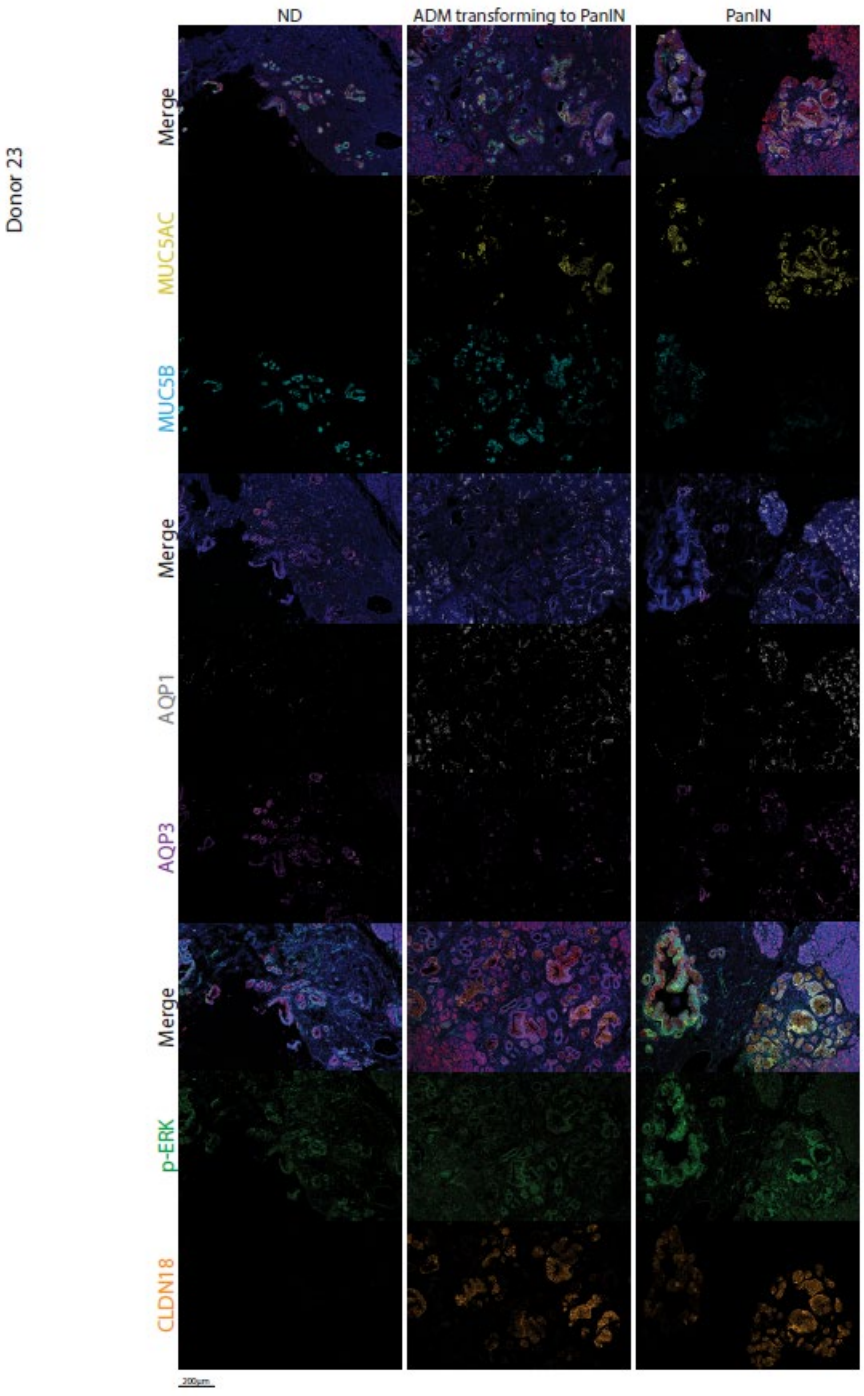

ND
ADM transforming to PanIN
PanIN
Donor 23
Merge
MUC5AC
MUC5B
Merge
AQP1
AQP3
Merge
p-ERK
CLDN18
200µm

Figure 2.19 Immunofluorescence staining of Epithelial markers-Donor 23
Immunofluorescence staining of serial sections of normal duct (ND), ADM with PanIN transformation, and PanIN lesions found in donor tissue. In order from top row to bottom row: Merged co-IF of ECadherin (red), MUC5AC (yellow) and MUC5B (blue). Single channel of MUC5AC staining. Single channel of MUC5B staining. Merge of co-IF of AQP1 (grey) and AQP3 (purple). Single channel of AQP1 staining. Single channel of AQP3 staining. Merge of co-IF of p-ERK (green), E-Cadherin (red) and CLDN18 (orange). Single channel of p-ERK staining. Single channel of CLDN18 staining.

Figure 2.20

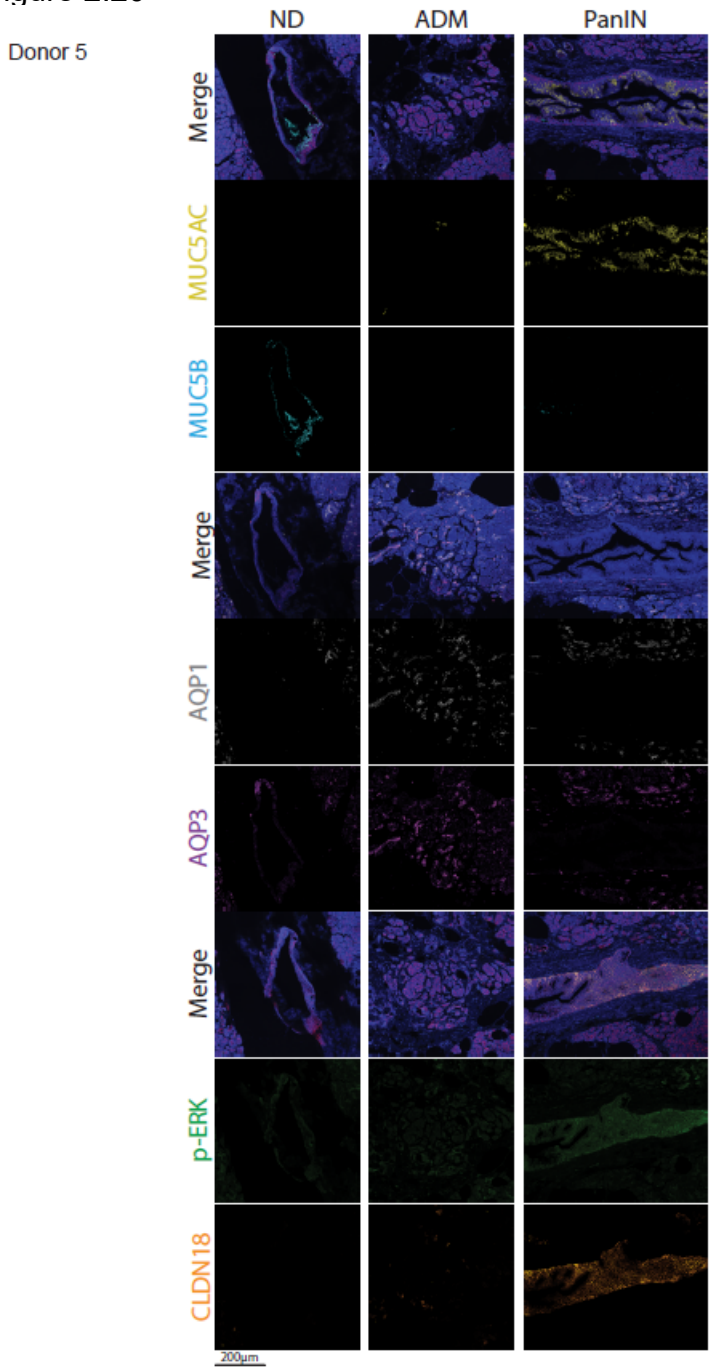


Figure 2.20 Immunofluorescence staining of Epithelial markers-Donor 5
Immunofluorescence staining of serial sections of normal duct (ND), ADM, and PanIN lesions found in donor tissue. In order from top row to bottom row: Merged co-IF of E-Cadherin (red), MUC5AC (yellow) and MUC5B (blue). Single channel of MUC5AC staining. Single channel of MUC5B staining. Merge of co-IF of AQP1 (grey) and AQP3 (purple). Single channel of AQP1 staining. Single channel of AQP3 staining. Merge of co-IF of p-ERK (green), E-Cadherin (red) and CLDN18 (orange). Single channel of p-ERK staining. Single channel of CLDN18 staining.

Figure 2.21

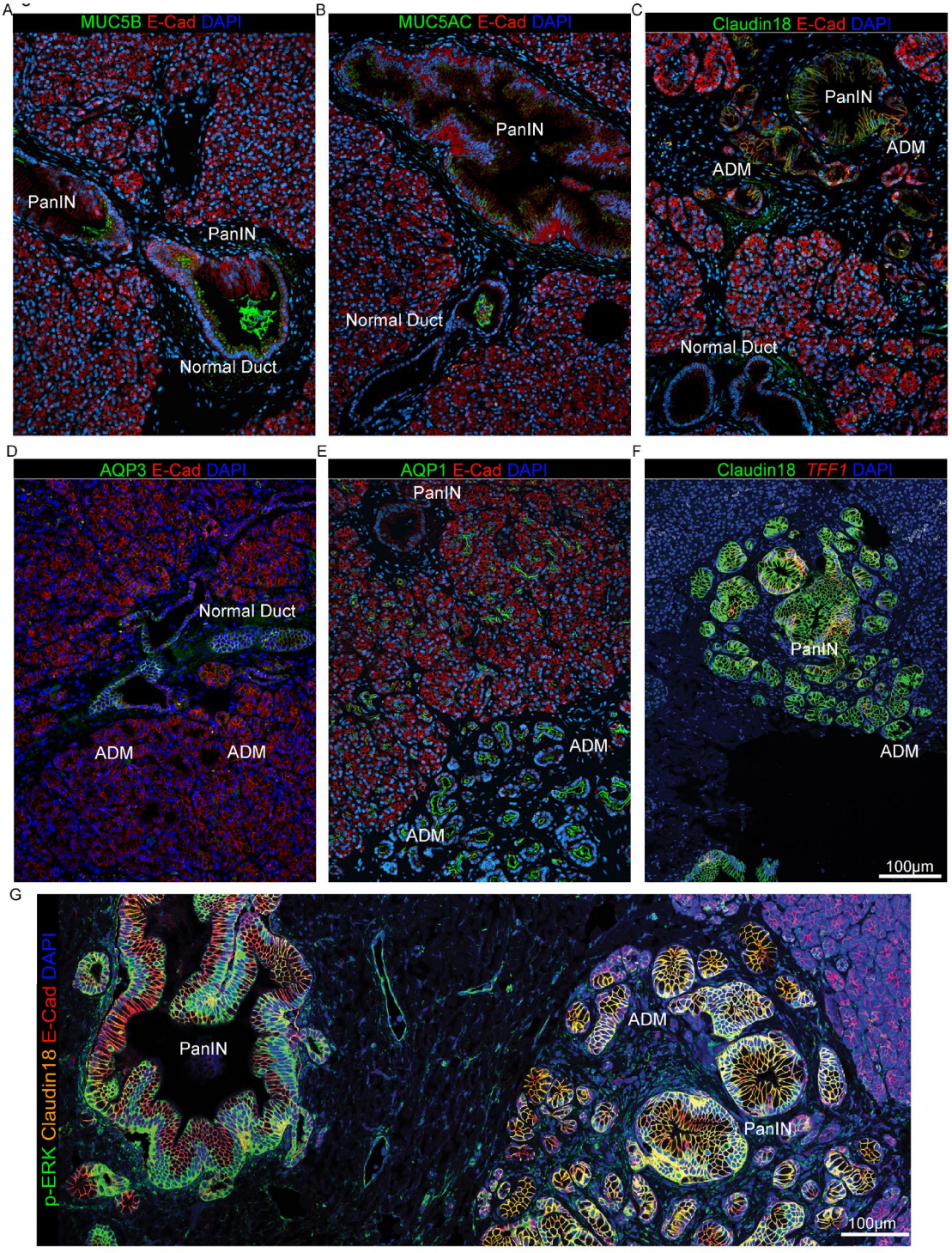

A
MUC5B E-Cad DAPI
PanIN
PanIN
Normal Duct
B
MUC5AC E-Cad DAPI
PanIN
Normal Duct
C
Claudin18 E-Cad DAPI
PanIN
ADM
ADM
Normal Duct
D
AQP3 E-Cad DAPI
Normal Duct
ADM
ADM
E
AQP1 E-Cad DAPI
PanIN
ADM
ADM
F
Claudin18 TFF1 DAPI
PanIN
ADM
100μm
G
p-ERK Claudin18 E-Cad DAPI
PanIN
ADM
PanIN
100μm

Figure 2.21 Claudin 18, MUC5AC/B, and AQP1/3 distinguish normal Ducts, ADM, and PanIN in healthy pancreas.
(A) Donor tissue stained with antibodies against Muc5B (green) and E-Cadherin (red), along with DAPI. (B) Donor tissue stained with antibodies against Muc5AC (green) and E-Cadherin (red), along with DAPI. (C) Donor tissue stained with antibodies against Claudin18 (green) and E-Cadherin (red), along with DAPI. (D) Donor tissue stained with antibodies against Aqp3 (green) and E-Cadherin (red), along with DAPI. (E) Donor tissue stained with antibodies against Aqp1 (green) and E-Cadherin (red), along with DAPI. (F) Donor tissue stained with RNAScope probe for *TFF1* (red) and antibody against Claudin18 (green), along with DAPI. (G) Donor tissue stained with antibodies against p-ERK (green), Claudin18 (orange), and E-Cadherin (red), along with DAPI.

Tables

Table 1: Demographics and clinical data for donor samples

Donor ID	Sex	Race	Lesions	BMI	Weight (Kg)	DM (Y/N)	EtOH Use	Tobacco Use	Sequencing Run
Donor 1	Female	Black	Yes	43.9	112.5	Y (ID)	Occasional	None	3829-EC
Donor 2	Male	Black	No	29.2	87.3	N	Unrecorded	None	Head 3861-EC; Tail 3862-EC
Donor 3	Male	Black	Yes	21.1	59	N	16 drinks per week	50 pack-year, current use	
Donor 4	Male	White	No	28.9	84	N	Occasional	Tobacco x 6yrs, unrecorded amount	Head 4160-EC; Tail 4161-EC
Donor 5	Female	White	Yes	32	77	Y	None	None	Head 4346-EC; Tail 4347-EC
Donor 6	Male	White	No	20.6	61.6	N	Rarely	1-2 cigarettes a month	Head 4450-E; Tail 4451-EC
Donor 7	Female	White	Yes	28.8	81.4	N	6 drinks per day	35 pack-year	
Donor 8	Male	White	Yes	32.2	107.9	Y (NID)	4 drinks per day	5 pack-year, quit 1991	Head 4637-EC1; Tail 4637-EC2
Donor 9	Male	Black	Yes	26.1	95.3	N	10 drinks per week	None	Head 4741-EC1; Tail 4741-EC2
Donor 10	Male	White	Yes	22.8	78.2	N	6 drinks per month	29 pack-year, current use	
Donor 11	Male	White	Yes	28.6	90.5	N	Daily	Daily	
Donor 12	Male	Black	No	20.1	61.6	TBD	1 drink, daily	None	
Donor 13	Female	White	No	26.4	83.8	N	Daily	Vape	
Donor 14	Male	White	Yes	23.2	71	N	Rarely	1pack a day x 15yrs	
Donor 15	Female	Not Specified/Unknown	No	51.2	126.1	N	Occasional	less than a pack a day x 19 yrs	
Donor 16	Male	Asian	No	24.2	66	N	Occasional	None	
Donor 17	Female	White	Yes	19.2	57.6	N	Daily	Yes-amout not specified	
Donor 18	Male	Black	No	34.6	103.5	N	Rarely	1pack a day	
Donor 19	Female	White	Yes	30.1	92.8	Y	Occasional	None	
Donor 20	Male	White	No	35.1	120	N	Occasional	1-2 sigarettes per day	
Donor 21	Male	Black	Yes	22.6	69.2	N	Daily, a pint	2 packs a week	
Donor 22	Male	White	No	31.2	95.4	Y (NID)	Occasional	less than a pack a day x 11 yrs	
Donor 23	Male	White	Yes	32.8	95.9	Y (NID)	2x a month	5 years	
Donor 24	Female	White	No	33.7	93	N	A pint a day	Half pack a day	
Donor 25	Female	White	Yes	38.6	105.2	Y	Occasional	1-2 cigarettes a yr	
Donor 26	Male	White	Yes	30.9	109	N	1 drink daily x 17yrs	1 pack a day x 17 yrs	
Donor 27	Male	White	Yes	26.2	80.28	N	3-4 drinks daily	1 pack a day x 56 yrs	
Donor 28	Male	Black	Yes	24.8	82.2	N	Occasional	None	
Donor 29	Female	White	No	29.9	69	N	1-2 drinks per week	None	
Donor 30	Male	Black	Yes	29.8	91.3	N	Occasional	None	

Table 2: Kras mutational profiling on select donor samples

Sample ID	IGO ID	Total	Droplet	Droplet Count	Ratio	Accepted	Mean	Std Ratio	Average
AIFR291_C1	Well 1	9	6	2383	0.002518	20651			
	Well 2	9	13	2380	0.005462	21779			
	Well 3	9	4	2208	0.001812	19504	0.0032639	0.0019363	20645
AII1271_C1	Well 1	9	3	4725	0.000635	21304			
	Well 2	9	9	4427	0.002033	19803			
	Well 3	9	8	3873	0.002066	18917	0.0015778	0.0008167	20008
Negative	Neg/Water	0	0	0	0.000000	19762			
Positive	Positive Control	9	2095	1947	1.076014	20354			
gDNAControl	H gDNA Control	9	0	1810	0.000000	19821			

Sample ID	IGO ID	Total	Droplet	Droplet Count	Ratio	Accepted	Mean	Std Ratio	Average
AIFR291_C1	Well 1	9	2	2264	0.000883	20949			
	Well 2	9	3	2281	0.001315	21384			
	Well 3	9	1	2285	0.000438	19901	0.0008787	0.0004388	20745
AII1271_C1	Well 1	9	1	4269	0.000234	20360			
	Well 2	9	2	4710	0.000425	21184			
	Well 3	9	1	4208	0.000238	20603	0.0002988	0.0001089	20716
Negative	Neg/Water	0	0	0	0.000000	19356			
Positive	Positive Control	9	191	1795	0.106407	19702			
gDNAControl	H gDNA Control	9	0	1753	0.000000	20787			

Sample ID	IGO ID	Total	Droplet	Droplet Count	Ratio	Accepted	Mean	Std Ratio	Average
AIFR291_C1	Well 1	9	1	2443	0.000409	21557			
	Well 2	9	1	2293	0.000436	20449			
	Well 3	9	0	2237	0.000000	18880	0.0002818	0.0002444	20295
AII1271_C1	Well 1	9	0	4654	0.000000	20515			
	Well 2	9	0	4679	0.000000	19898			
	Well 3	9	0	4400	0.000000	20140	0	0	20184
Negative	Neg/Water	0	0	0	0.000000	21097			
Positive	Positive Control	9	647	1731	0.373772	20601			
gDNAControl	H gDNA Control	9	0	1794	0.000000	20530			

Mutation Tested	Sample ID	Mean Ratio	Std Ratio	Average Accepted Droplets
KRAS G12D	AIFR291_C1	0.0033	0.0019	20645
KRAS G12D	AII1271_C1	0.0016	0.0008	20008
KRAS G12R	AIFR291_C1	0.0009	0.0004	20745
KRAS G12R	AII1271_C1	0.0003	0.0001	20716
KRAS G12V	AIFR291_C1	0.0003	0.0002	20295
KRAS G12V	AII1271_C1	0.0000	0.0000	20184

Table 3: Multiplex IF antibodies

Antibodies	**Source**	**Catalog Number**
Rabbit anti-human CD3, 1:100	Dako	A0452
Rabbit anti-human CD8, 1:400	Bioss	bs-0648R
Mouse anti-human CD163, 1:400	Leica	6080491
Mouse anti-human Arg1, 1:400	Proteintech	66129-1-Ig
Mouse anti-human Pancytokeratin, 1:500	Dako	M3515
Mouse anti-human FoxP3, 1:400	Biolegend	320201
Rabbit anti-human αSMA, 1:100	Abcam	ab5694
Rabbit anti-human PDGFRb, 1:300	Abcam	ab32570
Rabbit anti-human FAP, 1:100	Abcam	ab53066
Rabbit anti-human Vimentin, 1:1000	Sigma Life Science	HPA001762
Rabbit anti-human CD45, 1:100	Abcam	ab10558

Table 4: Immunofluorescence Primary, Secondary Antibodies Used for co-IF and RNA FISH probes

Antibodies	**Source**	**Catalog Number**
Rabbit anti-human Claudin 18, 1:100	Invitrogen	700178
Rabbit anti-human Aqp1, 1:500	Abcam	ab219055
Rabbit anti-human Aqp3, 1:200	Abcam	ab125219
Rabbit anti-human Muc5ac, 1:200	Cell Signaling	61193T
Rabbit anti-human Muc5b, 1:200	Cell Signaling	74978S
Goat polyclonal anti-rabbit Alexa Fluor 594, 1:400	Thermo Fisher Scientific	A-32740
Goat polyclonal anti-rabbit Alexa Fluor 488, 1:400	Thermo Fisher Scientific	A-11008
Probe	**Source**	**Catalog Number**
Hs-TFF1	Advanced Cell Diagnostics	417281

Chapter 3-JAK/STAT3-Signaling in Myeloid Cells Drives Immunoregulation in Pancreatic Cancer

This chapter is currently in preparation for submission

Kristee L. Brown*, Padma Kadiyala*, Ashley Velez-Delgado*, Wei Yan, Katelyn Donahue, Yukang Wen, Chang Xu, Brian Griffith, Paola Medina-Cabrera, Rosa E. Menjivar, Wenting Du, Filip Bednar, Timothy L. Frankel, Eileen S. Carpenter, Yaqing Zhang,[#] Marina Pasca di Magliano[#]
*Authors contributed equally; [#]Co-corresponding authors

Abstract
Pancreatic ductal adenocarcinoma (PDAC) is a dismal disease with a 5-year survival rate of 12.5%. This poor prognosis is due in part to a lack of early detection methods and resistance to current therapies. One of the hallmark characteristics of PDAC is the presence of a dense stroma comprised of immunosuppressive myeloid cells. Among these cells, tumor associated macrophages (TAMs) secrete factors that support tumor survival directly and indirectly through immune suppression in the tumor microenvironment (TME). Therapeutic strategies that target TAMs have been unsuccessful in PDAC patients, as macrophages can promote both tumor growth and tissue repair. Signal and Transducer of Activation Transcription (STAT) factors are important regulators of myeloid cell function. Herein, we observed that loss of STAT3 in myeloid cells leads to reprogramming of TAMs to an immunostimulatory phenotype with reduced neoplastic transformation of epithelial cells. As compensation, fibroblasts in the TME secrete factors to promote tumorigenesis, highlighting the context-dependent dual roles of the JAK/STAT3 signaling axis. Understanding mechanisms that underlie macrophage-fibroblast interactions may improve tumor responsiveness to targeted therapies.

Introduction

Immunotherapies have transformed clinical prospects for patients with solid tumors (155-157); however, they have not proven to be effective in treating pancreatic ductal adenocarcinoma (PDAC) (158). The fibrotic stroma that is a hallmark of PDAC consists of myeloid cells, fibroblasts and extra cellular matrix and acts as a physical barrier that prevents effector CD8 T cell infiltration (159). Furthermore, it facilitates an anti-inflammatory milieu to functionally inhibit CD8 T cell activity (159). Inflammatory myeloid cells release factors that contribute to the establishment and progression of precancerous lesions (160). Cell subtypes include tumor associated macrophages (TAMs) and myeloid derived suppressor cells (MDSCs), which have been shown to drive immune suppression in mouse models of PDAC (21, 161-171). In one study, depletion of myeloid cells impeded tumor growth in a CD8 T cell dependent manner (21). Although myeloid ablation is therapeutically valuable for PDAC treatment, it can be detrimental in the long-term (25, 167). Efforts aimed at reprogramming myeloid cells to an anti-tumor phenotype are underway, as these cells are highly plastic, having both pro- and anti-tumoral features (172, 173). Uncovering mechanisms that regulate myeloid cell function may provide insights into developing novel therapies.

Signal transducer and activator transcription (STAT) factors have been implicated in regulating myeloid cell function (174). For instance, IFNy mediated activation of STAT1 has been associated with anti-inflammatory myeloid cell activity, whereas IL4 and IL10 mediated activation of STAT3 and STAT5/6 has been associated with pro-inflammatory myeloid activity (174, 175). Several studies have noted a pro-tumorigenic role of myeloid STATs (176, 177), while others have observed the contrary (178, 179), indicating that STAT activity in myeloid cells is context-dependent.

Although preclinical data indicate that targeting the JAK/STAT pathway would be promising for the treatment of PDAC, clinically favorable outcomes have not been observed to date (180). Of note, clinical studies have not dissected the impact of therapeutics on specific immune or stromal components in the microenvironment (180), highlighting the need for investigating the role of JAK/STAT signaling in non-tumor cells. We have previously observed that oncogenic KRAS promotes the activation of the JAK/STAT3 signaling pathway in myeloid cells (49). However, the impact of inhibiting the

JAK/STAT3 signaling pathway in myeloid cells in the context of PDAC needs elucidation. Herein, we investigate the role of JAK/STAT3 signaling in modulating the function of myeloid cells in pancreatic tumorigenesis. Our data demonstrate that deletion of STAT3 in myeloid cells impacts macrophage infiltration and polarization, but does not enhance anti-tumor T cell activity, which may be due to compensatory fibroblast reprogramming.

Results

STAT3 signaling in myeloid cells regulates carcinogenesis

We have previously shown that expression of oncogenic KrasG12D in the pancreas epithelium regulates myeloid cell JAK/STAT3 signaling activity during an early stage of disease progression (49). To assess the functional role of JAK/STAT3 signaling in myeloid cells during carcinogenesis we generated genetically engineered *Kras$^{Frt\text{-}STOP\text{-}Frt\text{-}G12D/+}$;Ptf1a$^{FlpO/+}$*; *Lyz2^{Cre}* (KFC) and *Kras$^{Frt\text{-}STOP\text{-}Frt\text{-}G12D/+}$;Ptf1a$^{FlpO/+}$*; *Lyz2^{Cre}*;*STAT3$^{f/f}$ (KFCS) mice.* The dual recombinase approach in the KFCS model combines Flippase-FRT and Cre-loxP systems to allow for oncogenic KRAS expression within the pancreatic epithelium and deletion of *Stat3* in myeloid cells (**Fig. 3.1A**). We evaluated changes in the pancreata when mice reached 16 weeks of age (**Fig. 3.1B**), the timepoint at which control KFC mice exhibited acinar-ductal metaplasia (ADM) and PanIN formation. Histological examination of the pancreata revealed ~4-fold more normal acini present in KFCS mice compared to KFC mice and decrease in lesion formation, including acinar-ductal metaplasia (ADM) and PanINs in KFCS relative to KFC mice (**Fig. 3.1C-D**). These data suggest that loss of STAT3 activity in myeloid cells can reduce oncogenic KRAS-induced early tumorigenesis. To verify that *Stat3* had been deleted in myeloid cells in vivo, pancreata from KFC and KFCS mice were analyzed by immunofluorescence staining. We observed a ~1.8-fold decrease in F4/80+ macrophage infiltration in KFCS pancreata. Furthermore, there were fewer pSTAT3+F4/80+ macrophages surrounding Ecad+ epithelial cells (**Fig. 3.1E**). Interestingly, there were significantly fewer cells in the microenvironment undergoing proliferation (assessed by Ki67 staining) and apoptosis (assessed by cleaved caspase 3) in KFCS pancreata. We did not find significant changes in collagen deposition (assessed by trichrome staining) within the groups. These data indicate that loss of STAT3 activity in myeloid cells potentially hampers tumorigenesis.

STAT3 signaling modulates myeloid cells' phenotype

To evaluate the influence of STAT3 signaling in myeloid cells on the microenvironment, we performed single-cell RNA sequencing (scRNA-seq) on pancreata of 16-week-old KFC (n=1) and KFCS (n=1) mice. Using Uniform Manifold Approximation and Projection (UMAP) visualization, we identified transcriptomes of 11 cell types based on previously established canonical markers (49) (**Fig. 3.2A, Fig. 3.3A**), including acinar cells ($Muc1^+$, $Spink1^+$, $Amy1^+$), epithelial cells ($Cdh1^+$, $Krt19^+$), endothelial cells ($Pecam1^+$, Vwf^+), mesothelial cells ($Msln^+$, $Pdgfra^-$,Dcn^+), fibroblasts ($Pdgfra^+$,Dcn^+), myeloid cells ($Ptprc^+$, $Itgam^+$), T cells ($Ptprc^+$, $Cd3e^+$), B cells ($Ptprc^+$, $Cd79a^+$, $Cd19^+$), NK cells ($Ptprc^+$, $Cd3e^-$, $Nkg7^+$), cycling myeloid cells ($Ptprc^+$, $Itgam^+$,$Ki67^+$), and cycling T cells ($Ptprc^+$, $Cd3e^+$, $Ki67^+$).

To further investigate transcriptomic changes in myeloid cells, we re-clustered them and observed shifts in the cell populations between KFC and KFCS groups (**Fig. 3.2C**). We noted 8 unique myeloid subsets (**Fig. 3.2C, Fig. 3.3B**): neutrophils ($S100a8^+$, $S100a9^+$, $Mmp9^+$), monocytes ($H2\text{-}Aa^+$), SAM2 macrophages (107) ($Ly6c2^+$,$Chil3^+$, $Plac8^+$), dendritic cells ($Flt3^+$, $Zbtb46^+$,$H2\text{-}Aa^+$, $Itgax^+$), alternatively activated macrophages SAM1 ($H2\text{-}Aa^+$,$C1qa^+$, $C1qb^+$, $Itgax^+$, $Cebpa^+$, $Trem2^+$), Folr2+ alternatively activated macrophages ($H2\text{-}Aa^+$,$C1qa^+$, $C1qb^+$, $Cebpa^+$, $Trem2^+$,$Folr2^+$), Slit3+ macrophages ($H2\text{-}Aa^+$,$Plac8^+$, $Slit3^+$), and CD3+ myeloid cells ($Itgam^+$, $Cd3e^+$). Relative abundance of SAM2 and $Slit3^+$ macrophages increased in the KFCS group compared to KFC, whereas abundance of alternatively activated macrophages, dendritic cells, and Flor2+ alternatively activated macrophages decreased (**Fig. 3.2D**). We next compared the differential gene expression of myeloid cells in the KFC and KFCS groups and generated a selected list of genes. Myeloid cells in the KFCS condition expressed genes associated with a pro-inflammatory state, including Stat1, Isg15 and Iftm6 and IFNy-inducible chemokine ligands Cxcl10 and Tnf. In contrast, myeloid cells in the KFC group were enriched in anti-inflammatory genes such as Mrc1, Arg1 and TAM marker C1qa (**Fig 3.2E**). These data suggest STAT3 signaling impacts the transcriptional profile of myeloid cells.

Given that macrophages are a predominant myeloid cell subset, and their function is dependent on stimuli present in the PDAC microenvironment, we set up an in vitro assay

to validate our scRNA-seq findings (**Fig**. **3.2F**). Bone marrow (BM) derived macrophages from *Lyz2^{Cre}* or *Lyz2^{Cre}*;*STAT3$^{f/f}$* mice were polarized with pancreatic tumor conditioned media for 24 hrs. It has been shown that pancreatic tumor conditioned media can upregulate TAM markers in BM macrophages (21, 181). Real time quantitative PCR analysis revealed low expression of Arg1 and C1q in Lyz2^{Cre};STAT3$^{f/f}$ BM macrophages relative to Lyz2^{Cre} BM macrophages *(**Fig. 3.2G**)*. These data suggest that factors present in tumor conditioned media may contribute to the activation of STAT3 signaling in macrophages.

Loss of STAT3 signaling in myeloid cells leads to compensatory reprogramming of fibroblasts

Fibroblasts are abundant in the PanIN microenvironment and play a critical role in modulating disease progression (182). Thus, we investigated whether JAK/STAT3 signaling in myeloid cells impacts the fibroblast transcriptome. From scRNA-seq analysis, we identified 7 distinct subsets of fibroblasts (**Fig. 3.4A-B**). Interestingly, 5 fibroblast clusters were unique to the KFCS group but were not seen in the KFC group (**Fig. 3.4B**). Differential gene expression analysis revealed that fibroblasts in the KFCS group have a pro-inflammatory gene signature, unlike KFC fibroblasts, which have a tumor restricting myofibroblast gene signature (Acta2^{+}, Thy1^{+}, Tagln^{+}). Moreover, we observed higher expression of Cxcl1, Cxcl2, Cxcl5, and Tnsf11, which promote granulocyte recruitment, in KFCS fibroblasts (**Fig. 3.4C**). Gene set enrichment analysis (GSEA) revealed upregulation of JAK/STAT3 signaling in KFCS fibroblasts (**Fig. 3.4D**). Supporting these findings, we observed ~2.4-fold fewer aSMA+ activated fibroblasts in the KFCS group; remarkably, the activated fibroblasts in the KFCS group were pSTAT3+ (**Fig. 3.4E**). These data indicate that loss of STAT3 activity in myeloid cells results in compensatory activation of STAT3 in fibroblasts.

Loss of STAT3 signaling in myeloid cells alters features of T cell subsets in microenvironment

Given that macrophages exhibited a pro-inflammatory transcriptional profile upon loss of STAT3 in myeloid cells (**Fig. 3.2D**), we sought to assess the gene signature of T cells. We identified naive CD4s, Tregs, T helper subtype 1 (Th1), T helper subtype 17 (Th17), ydT cells, and CD8s expressing exhausted markers (**Fig. 3.5A-C**) based on cell linage

markers (181, 183). We observed an increase in the proportions of Tregs, Th17 and ydT cells in the KFCS group compared to KFC. Interestingly, the proportion of Th1 and CD8 T cells expressing exhaustion markers were lower in KFCS. Accordingly, gene expression for T cell exhaustion markers Pdcd1, Gzmk and Ctla4 were downregulated in the KFCS pancreas (**Fig. 3.5D**). These data suggest that *Stat3* loss in myeloid cells impacts the exhaustion status of CD8 T cells.

Discussion

The JAK/STAT3 signaling pathway has been identified as a central hub for the mediation of tumor progression and immune functions (49-52). Histopathological analysis of human PDAC has revealed phosphorylated STAT3 expression in tumor specimens, but not in normal pancreas (55-57). Furthermore, JAK/STAT3 signaling activation is not required for pancreas cancer development (57). We previously discovered that oncogenic KRAS, a driver of pancreas cancer, modulates STAT3 signaling in tumor infiltrating myeloid cells during early stages of tumorigenesis (49). While myeloid cells play an important role at various stages of PDAC development (184, 185), there is limited understanding about the mechanisms they utilize to drive immunosuppression and whether they interact with other cells types in the PanIN microenvironment at these stages. Herein, we delineated the role JAK/STAT3 signaling plays in myeloid cells during tumorigenesis.

Due to limitations in imaging technology, it is not possible to procure ADM or PanIN biopsies from humans (186). Thus, to examine the contribution of STAT3 signaling in myeloid cells to the tumor milieu at early stages of tumorigenesis we utilized a genetically engineered mouse model that recapitulates features of the human disease. Similar to human pancreatic cancer, the KFC model exhibits mutations in *Kras* (92) and serves as a good model to study dynamic changes in the microenvironment. We observed STAT3 activity in myeloid cells surrounding precancerous ADM and PanIN lesions (**Fig. 3.1**). Previous work in a KRAS driven PDAC model showed that STAT3 signaling promotes ADM and PanIN formation (52). We noted that loss of STAT3 in myeloid cells potentially hampers tumorigenesis (**Fig. 3.1**). It is well known that activated macrophages surround ADM lesions (160), and our data suggest that STAT3 signaling in myeloid cells potentially drives the initial transdifferentiation process.

A previous study showed that STAT3 signaling in macrophages polarizes them to an anti-inflammatory phenotype (187), indicating that lack of STAT3 in myeloid cells promotes a pro-inflammatory function. In accordance, LysM-Cre mediated deletion of STAT3 in a pancreatic neuroendocrine model reduced tumor growth (188) and enhanced anti-tumor T cell response in colorectal cancer and lung cancer models (189, 190). These results indicate that STAT3 signaling in myeloid cells regulates immunosuppressive functions (191). However, the role myeloid STAT3 signaling plays during early stages of pancreas tumorigenesis has not been elucidated. We observed that loss of STAT3 signaling in myeloid cells transforms them to an immunostimulatory status (**Fig. 3.2**). Tumor conditioned media treated bone marrow derived macrophages that lacked *Stat3* demonstrated reduced Arg1 expression, indicating that they are less immunosuppressive (**Fig. 3.2**).

Interestingly, we found that loss of *Stat3* signaling in myeloid cells resulted in activation of JAK/STAT3 signaling in fibroblasts (**Fig. 3.4**). These fibroblasts exhibited an immunosuppressive transcriptional profile that may limit the anti-tumor immune responses promoted by myeloid *Stat3* loss (**Fig. 3.5**). Similarly, others have shown that STAT3 signaling in CAFs facilitates pancreatic tumorigenesis (58). Regulation of the JAK/STAT3 pathway in the microenvironment is complex, and our findings highlight the importance of dissecting its role in different cell types, along with crosstalk within the TME, to understand mechanisms that drive tumorigenesis and therapeutic resistance.

Methods

Animal Strains

Mice were housed in pathogen free conditions at the University of Michigan. KFCS mice were generated by crossing KF ($Kras^{Frt\text{-}STOP\text{-}Frt\text{-}G12D/+}$;$Ptf1a^{FlpO/+}$) with $Lyz2^{Cre}$;$STAT3^{f/f}$ mice. Changes in the pancreata were evaluated when mice reached 16 weeks of age.

Histology and Immunohistochemistry

Pancreas tissue was fixed in 10% neutral-buffered formalin for 24h, embedded in paraffin and serially sectioned 5 μm thick. Hematoxylin and eosin (H&E), Gomori's Trichrome, immunohistochemical and immunofluorescent stains were performed on tissue section as described previously (34, 181). Images were acquired using Olympus BX53F

microscope equipped with CellSens software. Areas of the stain in micrographs was quantified using ImageJ software. Histopathological analysis of the H&E stains was performed by a pathologist (WY) as described previously.

Single cell RNA sequencing

Pancreas were processed into single-cell suspension as described previously and subjected to single-cell RNA sequencing using the NextGen 10x platform and reverse transcription reaction was performed at the University Sequencing Core. Approximately 50 ng of the amplified cDNA was used for each sample to construct the libraries. Paired-end sequencing was performed on the Novaseq 6000 Illumina sequencing platform.

Data analysis was performed using the Seurat R package version 4.0. Data were filtered, normalized, scaled to identify highly variable genes, then linear dimensional reduction was performed and cell clusters were identified as described previously (49, 181, 183). Differential expression analysis on the cell compartments was performed to delineate gene signatures. Pathway enrichment analysis using the ClusterProfiler package was performed to identify specific signaling pathways that were altered.

Macrophage Assay

Tumor condition media was collected from 7940B cells cultured in IMDM with 10% FBS and 1% Pen Strep for 72hrs. Bone marrow cells isolated from *Lyz2*^{Cre} or *Lyz2*^{Cre};*STAT3*$^{f/f}$ mice and cultured in IMDM media with 10% FBS, 1% Pen Strep, and 50ng/mL MCSF for 5 days to generate M0 macrophages (21). Then, macrophages were treated with 7940B tumor condition media for 24h and RNA was extracted using Qiagen kit, cDNA was generated using complementary DNA kit. Quantitative real-time polymerase chain reaction analysis was performed using *Arg1* and *C1qa* primers as described previously, and *Ppia* was used as a housekeeping control (34, 49, 181, 183).

Statical Analysis

Sample sizes were selected based on preliminary data from pilot experiments and previous published studies. Animal studies were performed after randomization. Unpaired Student t-test or two-way analysis of variance (ANOVA) was utilized for comparing experimental groups from histology and staining and functional assays. Data were analyzed using Prism 9.0 (GraphPad Software). P values less than 0.05 were considered

statistically significant and values are reported as means ± SD with the indicated sample size.

Acknowledgements

The work is supported in part by R01-CA268426 awarded to M.P.M. and T.L.F. Work in the M.P.M. laboratory was also supported by NIH/NCI grants R01-CA260752, R01-CA271510, U01-CA224145, U01-CA274154, and U54CA274371. Work in the T.L.F. laboratory was supported by NIH/NCI grant U01CA274154, NIH/National Institute of Diabetes and Digestive and Kidney Diseases (NIDDK) 5R01DK128102, and VA BLR&D Merit Award 5I01BX005777, P.K. was supported by NIH/National Institute of Allergy and Infectious Diseases T32-AI007413 and NIH/National Institute of General Medical Sciences (NIGMS) T32-GM113900. K.D. was supported by NIH/NCI F31-CA265085-01A1. Y.Z. was supported by R50 CA232985.

Author Contributions: K.L.B., P.K., A.V.D., Y.Z., M.P.M. designed the research. K.L.B., P.K., A.V.D., W.Y., K.D., Y.W., C.X., P.M.C., B.G., R.E.M., W.D. performed the experiments. K.L.B., P.K., A.V.D, W.Y., K.D. performed data analysis. P.K., A.V.D., Y.Z., M.P.M. wrote the original draft of the manuscript. K.L.B., P.K., A.V.D, W.Y., K.D., Y.W., C.X., B.G., R.E.M., W.D., F.B., T.L.F., E.C., Y.Z., M.P.M. read and edited the manuscript. F.B., T.L.F.,Y.Z., M.P.M. supervised and provided funding sources.

Figures

Figure 3.1

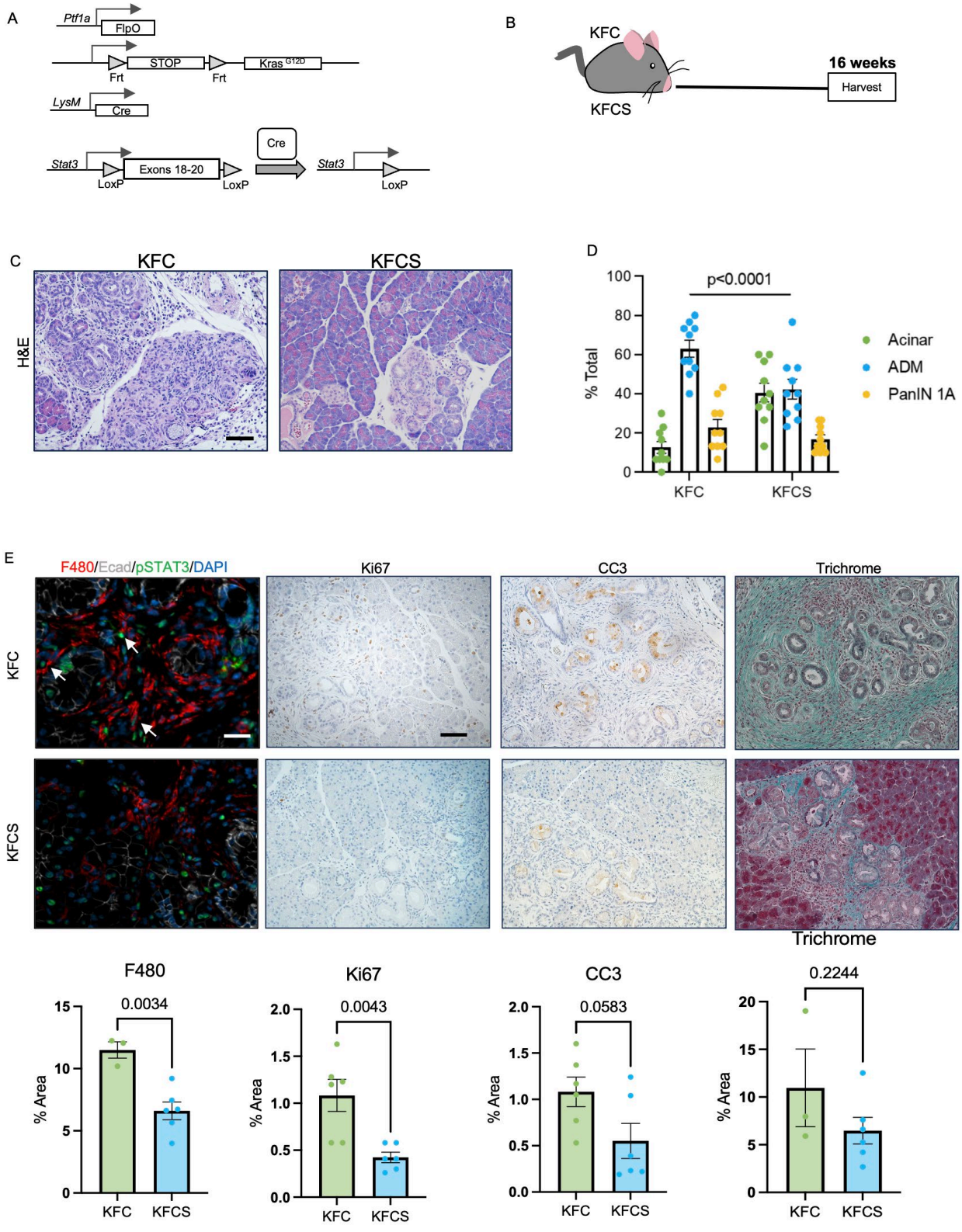


Figure 3.1 STAT3 activation in myeloid cells is required for tumorigenesis.
(A) Genetic makeup of the $Kras^{Frt\text{-}STOP\text{-}Frt\text{-}G12D/+}$;$Ptf1a^{FlipO/+}$;$Lyz2^{Cre}$;$Stat3^{f/f}$ mouse model. (B) Experimental time frame for harvesting pancreata. C. H&E staining of KFC and KFCS pancreata at 16-week timepoint. Scale bar = 200 μm. (D) Pathological analysis of lesion subtypes in KFC and KFCS pancreata at 16-week timepoint. Data represent mean ± SEM, n = 10 mice/group. Statistical analysis was assessed by 2-way ANOVA. $P < 0.05$ was considered significant. I Immunofluorescence staining for F4/80 (red), Ecad (grey), pSTAT3 (green) and DAPI (blue); immunohistochemistry for Ki67 and cleaved caspase 3 (CC3) and gomoria trichrome staining in KFC and KFCS pancreata. Scale bar = 50μm. Quantification of each stain is depicted at the bottom, data represent mean ± SEM, n = 6 mice/group with the exception of F4/80 and trichrome KFC group (n=3 mice/group). Statistical analysis was assessed by unpaired student t-test. $P < 0.05$ was considered significant.

Figure 3.2

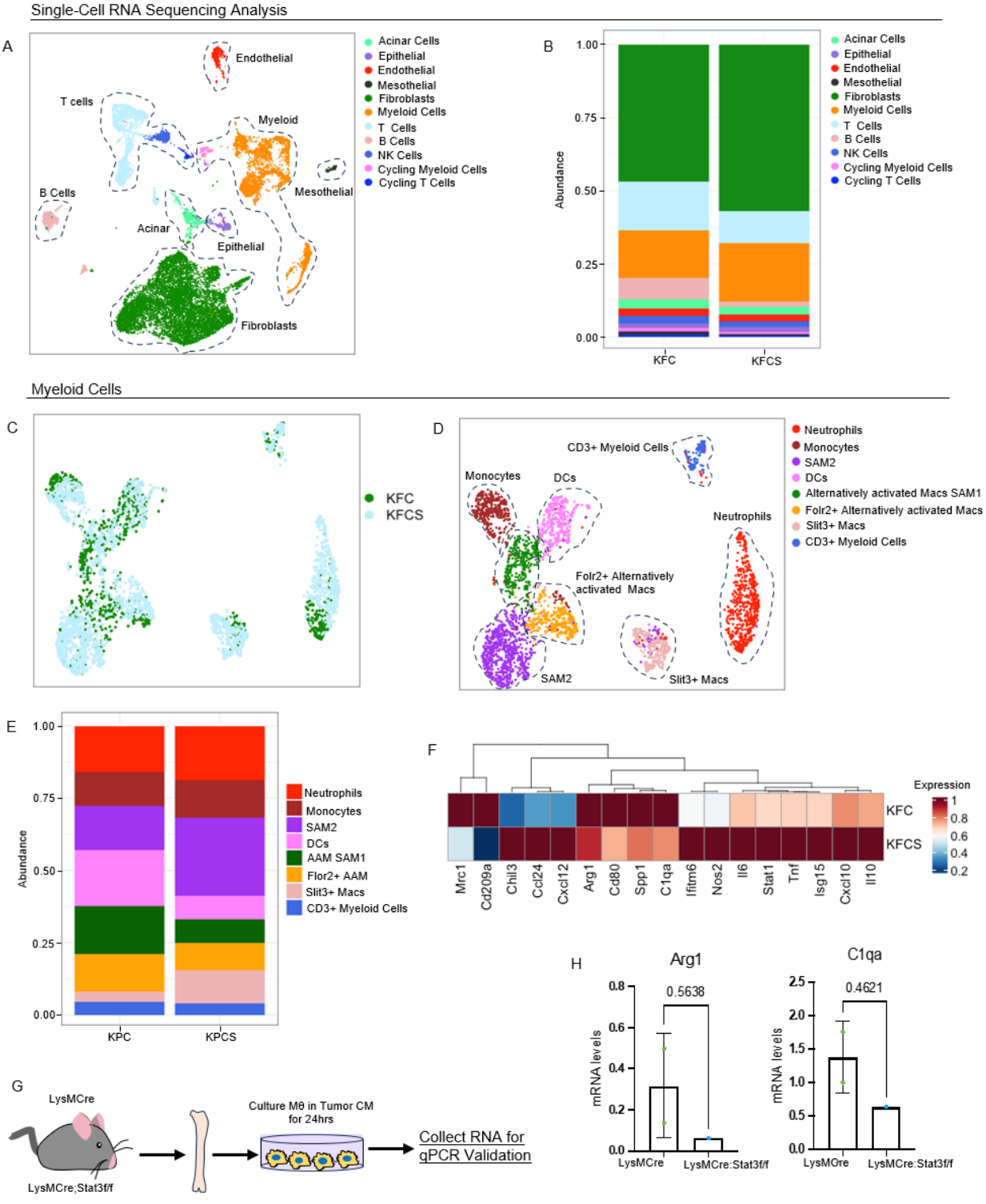

Single-Cell RNA Sequencing Analysis
A
Endothelial
T cells
Myeloid
Mesothelial
B Cells
Acinar
Epithelial
Fibroblasts
Acinar Cells
Epithelial
Endothelial
Mesothelial
Fibroblasts
Myeloid Cells
T Cells
B Cells
NK Cells
Cycling Myeloid Cells
Cycling T Cells
B
Abundance
1.00
0.75
0.50
0.25
0.00
KFC
KFCS
Myeloid Cells
C
KFC
KFCS
D
CD3+ Myeloid Cells
Monocytes
DCs
Neutrophils
Folr2+ Alternatively activated Macs
SAM2
Slit3+ Macs
Neutrophils
Monocytes
SAM2
DCs
Alternatively activated Macs SAM1
Folr2+ Alternatively activated Macs
Slit3+ Macs
CD3+ Myeloid Cells
E
Abundance
KPC
KPCS
Neutrophils
Monocytes
SAM2
DCs
AAM SAM1
Flor2+ AAM
Slit3+ Macs
CD3+ Myeloid Cells
F
Expression
KFC
KFCS
Mrc1
Cd209a
Chil3
Ccl24
Cxcl12
Arg1
Cd80
Spp1
C1qa
Ifitm6
Nos2
Il6
Stat1
Tnf
Isg15
Cxcl10
Il10
G
LysMCre
LysMCre;Stat3f/f
Culture MΘ in Tumor CM for 24hrs
Collect RNA for qPCR Validation
H
Arg1
0.5638
mRNA levels
LysMCre
LysMCre:Stat3f/f
C1qa
0.4621
mRNA levels
LysMCre
LysMCre:Stat3f/f

Figure 3.2 STAT3 signaling in myeloid cells regulates macrophage immunosuppressive phenotype
(A) UMAP representation of identified cell population and (B) histogram of cell type abundance noted in KFC and KFCS groups. (C) UMAP overlay of re-clustered myeloid cells from KFC and KFCS groups (D) UMAP representation of identified myeloid cell subtypes aI(E) histogram of cell abundance in KFC and KFCS groups. (F) Heatmap of select genes associated with myeloid cell function. Average gene expression was based relative to highest expressor. (G) Experimental design depicting culturing of bone marrow derived macrophages in tumor condition media (H) Realtime-quantitative PCR analysis for *Arg1* and *C1q* expression in macrophages. n=2 in $LysM^{cre}$ and n=1 in $LysM^{cre}$;$Stat3^{f/f}$ groups. Statistical analysis was assessed by unpaired student t-test. $P < 0.05$ was considered significant

Figure 3.3

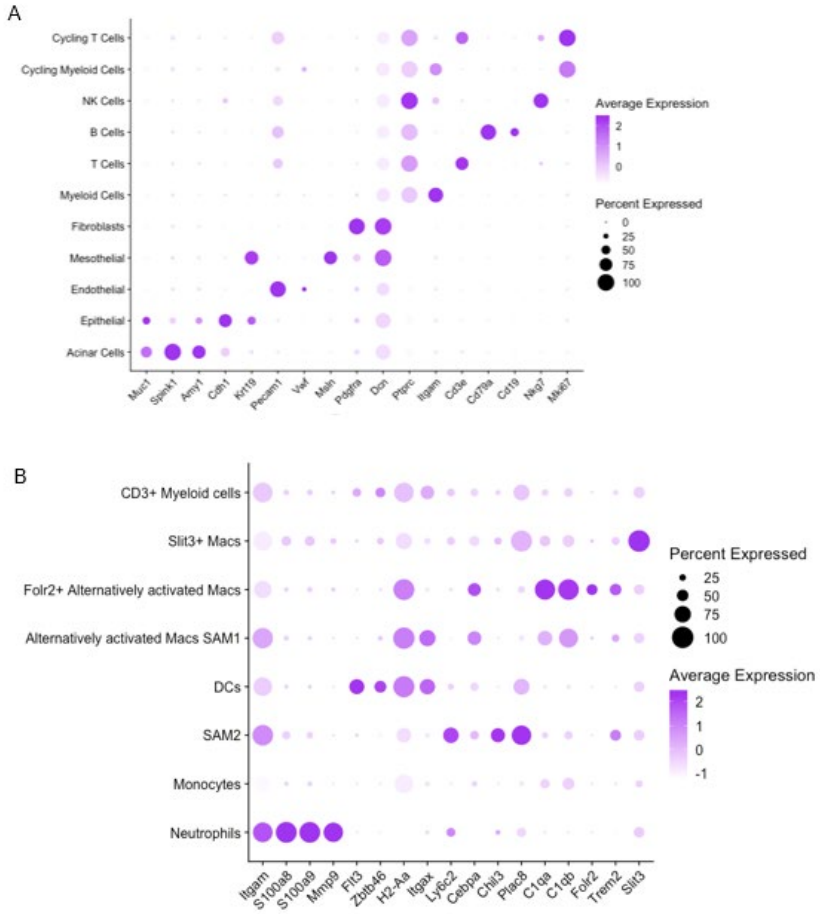


Figure 3.3 Single cell RNA-sequencing Data of KFC and KFCS mice.
Dot plots of markers used to identify (A) all cell populations or (B) myeloid cell subtypes in KFC and KFCS samples.

Figure 3.4

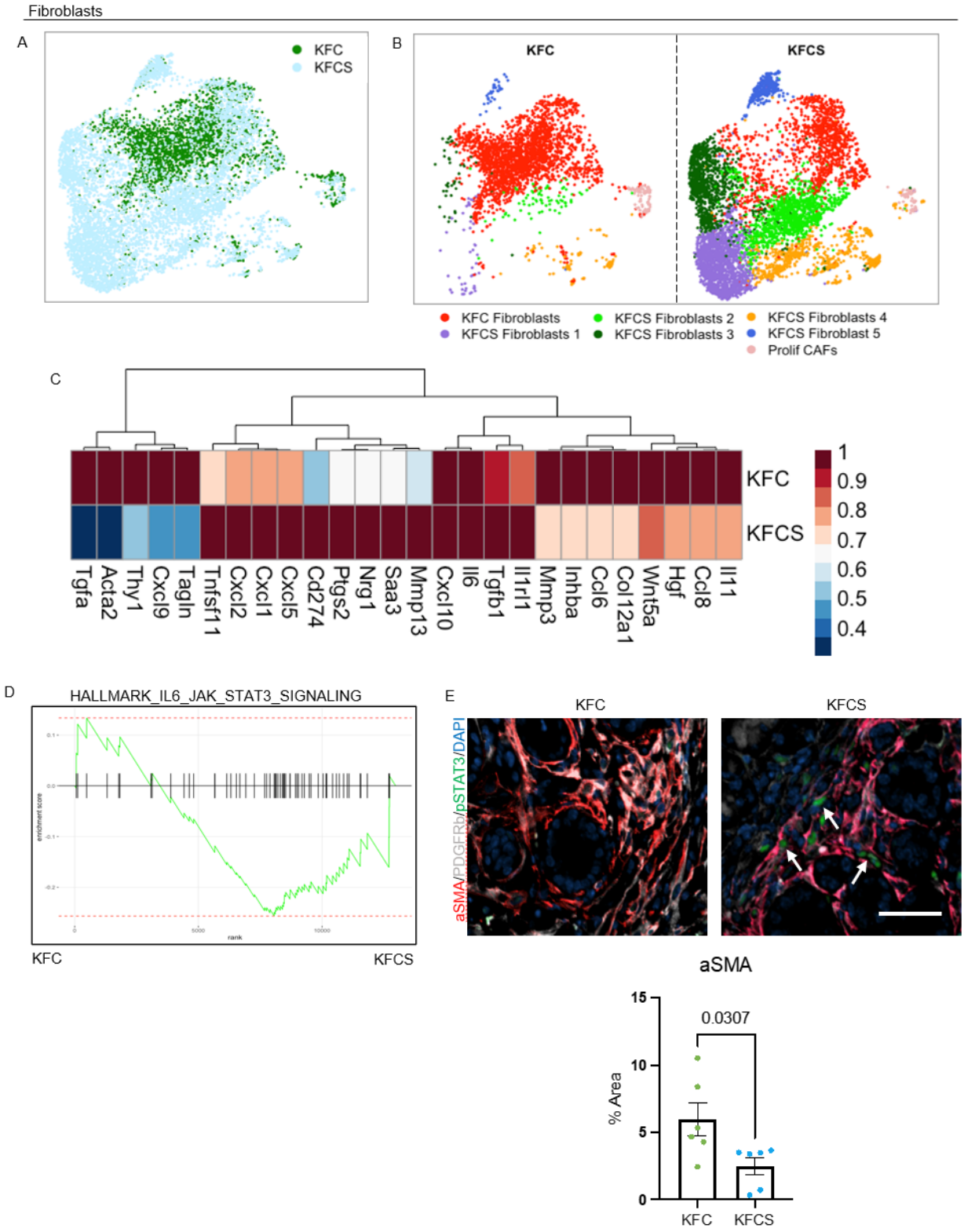

Fibroblasts
A
KFC
KFCS
B
KFC
KFCS
KFC Fibroblasts
KFCS Fibroblasts 1
KFCS Fibroblasts 2
KFCS Fibroblasts 3
KFCS Fibroblasts 4
KFCS Fibroblast 5
Prolif CAFs
C
KFC
KFCS
1
0.9
0.8
0.7
0.6
0.5
0.4
Tgfa
Acta2
Thy1
Cxcl9
Tagln
Tnfsf11
Cxcl2
Cxcl1
Cxcl5
Cd274
Ptgs2
Nrg1
Saa3
Mmp13
Cxcl10
Il6
Tgfb1
Il1rl1
Mmp3
Inhba
Ccl6
Col12a1
Wnt5a
Hgf
Ccl8
Il11
D
HALLMARK_IL6_JAK_STAT3_SIGNALING
enrichment score
rank
KFC
KFCS
E
KFC
KFCS
aSMA/PDGFRb/pSTAT3/DAPI
aSMA
0.0307
% Area
15
10
5
0
KFC
KFCS

Figure 3.4 Loss of STAT3 signaling in myeloid cells results in fibroblast reprogra
(A) UMAP overlay of re-clustered fibroblasts from KFC and KFCS groups (B) UMAP representation of unique fibroblast clusters in KFC and KFCS groups. (C) Heatmap of curated genes associated with fibroblast secretome. Average gene expression was based relative to highest expressor. (D) Gene set enrichment analysis of JAK/STAT3 signature in fibroblasts from KFC compared to IS. (E) Immunofluorescence staining for aSMA (red), Pdgfra/b (grey), pSTAT3 (green) and DAPI (blue) in KFC and KFCS pancreata. Scale bar = 20μm. White arrows point to pSTAT3+/aSMA+ fibroblasts. Quantification of aSMA stain is depicted at the bottom, data represent mean ± SEM, n = 6 mice/group. Statistical analysis was assessed by unpaired student t-test. $P < 0.05$ was considered significant

Figure 3.5

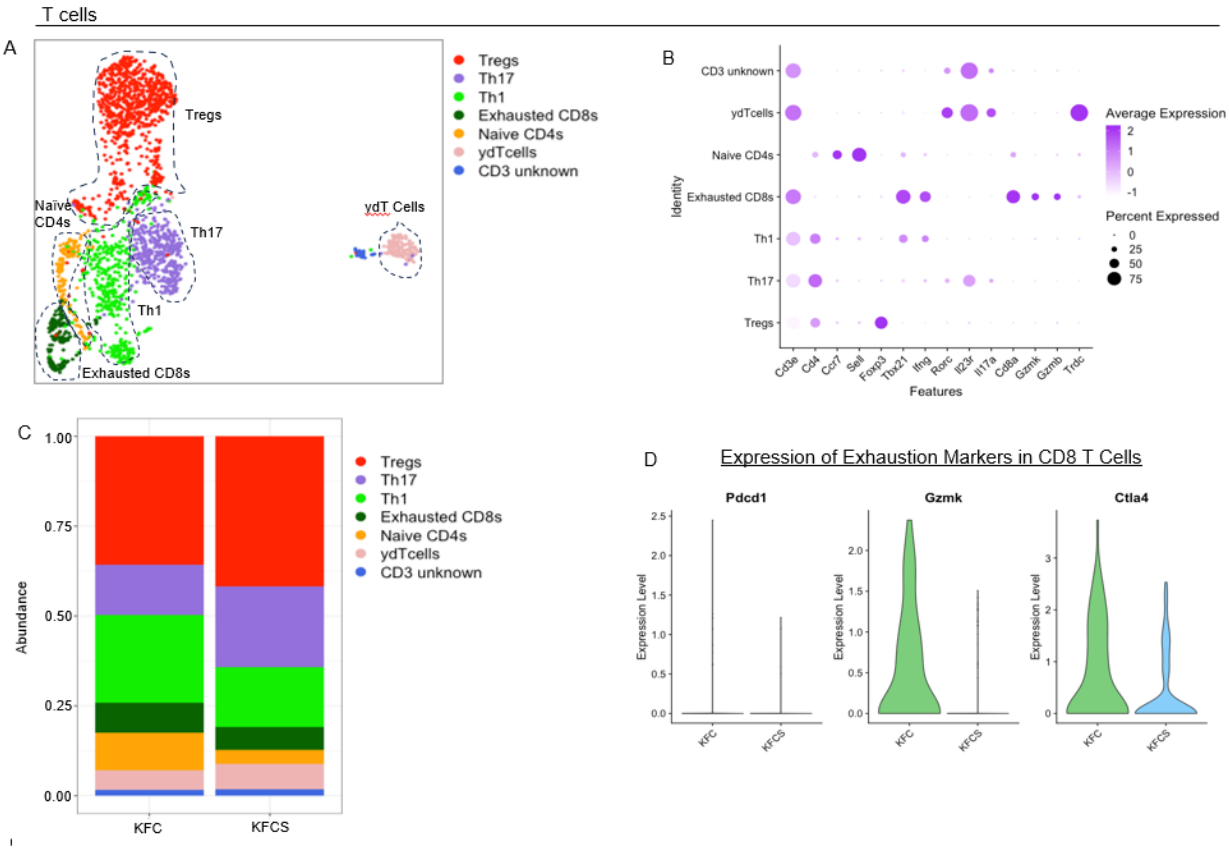


Figure 3.5 Loss of STAT3 signaling in myeloid reduces expression of exhaustion markers in CD8 T cells
(A) UMAP representation of re-clustered T cells in KFC and KFCS groups. (B) Dot plot of markers used to identify various T cell subtypes. (C) Cell abundance histogram of various T cell subsets in KFC and KFCS groups. (D) Violin plots of normalized gene expression levels of T cell exhaustion markers

Chapter 4- Crosstalk between Cancer Associated Fibroblasts and T Helper 2 Cells in Pancreas Cancer

This chapter is currently in preparation for submission

Padma Kadiyala, Jacqueline Morales, Kristee Brown, Brian Griffith, Katelyn Donahue, Ahmed Elhossiny, Wenting Du, Xi He, Timothy Frankel, Eileen Carpenter, Filip Bednar, [#]Yaqing Zhang, [#]Marina Pasca Di Magliano
[#]Co-corresponding authors

Abstract

Pancreatic ductal adenocarcinoma (PDAC) is a dismal disease with a 5-year survival rate of 12.5%. A hallmark feature of this disease is its abundant microenvironment which creates a highly immunosuppressive milieu. The PDAC tumor microenvironment consists of dense fibrotic stroma and immune cells of suppressive nature that render cytotoxic T cell activity. Our previous work has demonstrated that depletion of regulatory T cells (Tregs) from a mouse model of PDAC does not promote an anti-tumor immune response. Rather, Treg depletion reprogramed fibroblasts in the tumor microenvironment to exhibit an inflammatory phenotype, which contributed to the recruitment of immunosuppressive myeloid cells to promote tumor progression. Herein, we explored the fate of the CD4 T cells subsets in the Treg depleted PDAC. Intriguingly, single-cell RNA sequencing analysis of the pancreatic neoplastic lesions upon Treg depletion revealed that the majority of infiltrating CD4 T cells were Gata3+ T helper 2 (Th2) cells. We also noted that the pancreatic fibroblasts respond to type 2 cytokines *in vitro*, suggesting a potential crosstalk between Th2 cells and fibroblasts in PDAC tumor microenvironment. Results from our study will not only provide a new understanding of the role Th2 T cells play in PDAC development and disease progression, thereby addressing a significant knowledge gap in the field, but also lead to the development of novel strategies to target the Treg/Th2 axis.

Introduction

Pancreatic ductal adenocarcinoma (PDAC) is a dismal disease with a 5-year survival rate of 12.5% (1). This poor prognosis is due in part to a lack of early disease detection methods and resistance to current therapies (1-3). Surgical resection is feasible in less than 20% of cases and often does not result in cure (1-3). Consequently, there is an unmet need for the development of efficacious therapies for treating PDAC patients. Immune checkpoint blockade therapy has provided robust and durable clinical benefits in multiple solid tumors (192, 193). Unfortunately, this immunotherapy has been ineffective in improving PDAC patients' survival (192, 193). This is partially due to the immunosuppressive effects of the PDAC tumor microenvironment (TME), which is established at the earliest stages of tumorigenesis alongside the formation of the PDAC precursor lesions, pancreatic intraepithelial neoplasia (PanIN) (194, 195). Elucidating mechanisms of immune evasion will prove beneficial to treating the disease.

The tumor microenvironment (TME) is primarily comprised of cancer associated fibroblast (CAFs) and immunosuppressive cells that promote PDAC growth (194, 195). Cytotoxic CD8 T cells in the TME express high levels of exhaustion markers that indicate CD8 T cell dysfunction (41, 196). Our group has previously shown that depletion of CD4 T cells in a genetically engineered mouse model of PDAC suppresses the formation and progression of PanINs and increases infiltration of cytotoxic CD8 T cells into the TME (194). Furthermore, in this model we have also observed a reduction in immunosuppressive myeloid cell' infiltration, as well as CAF expansion. These data suggest that tumor infiltrating CD4 T cells promote pancreatic carcinogenesis by functionally repressing CD8 T cell activity. Because these observations are based on a model in which all CD4 T cells were eliminated (194), the contribution of specific CD4 T cell subtypes to the accumulation of fibroinflammatory stroma is unknown.

Tregs play an important role in balancing immune responses and tissue repair (197) and PDAC patients with Treg infiltration exhibit poor prognosis (198). Interestingly, depletion of Tregs in a spontaneous PDAC mouse model, accelerated carcinogenesis by re-programming the CAFs in the microenvironment (34). The re-programmed CAFs

expressed inflammatory cytokines such as *Ccl3*, *Ccl6*, and *Ccl8*, which facilitated recruitment of immunosuppressive myeloid cells into the PDAC TME. Furthermore, analysis of T cells in pancreas of Treg depleted mice revealed a drastic increase of T helper 2 (Th2) cytokine production (34).

Clinically PDAC stroma has been shown to be predominantly infiltrated by Th2 cells marked by GATA-3 expression over T helper 1 (Th1) cells marked by T-bet expression (199). The ratio of GATA-3/T-bet PDAC infiltrating cells was used as a predictive marker of patient survival (32). Th2 T cells secrete type 2 cytokines such as interleukin-4 (IL-4) and IL-13 (200, 201), which influence the polarization macrophages within the PDAC TME (200). The role of Th2 T cells in fibroblasts programming in the PDAC TME remains to be explored and is the focus of our study.

Results

CD8 T cells increase, but have a marked exhaustion transcriptional signature upon Treg depletion

We previously generated $Kras^{+/LSL\text{-}G12D}$; $Ptf1a^{+/Cre}$; $Foxp3^{tm3(DTR/GFP)Ayr}$ (KC;$Foxp3^{DTR}$) genetically engineered mouse model to evaluate the role of Tregs in PanIN microenvironment (34). We have shown that induction of acute pancreatitis (via caeruelin administration) synergizes with oncogenic *Kras* to promote PanIN formation in the KC mice (34, 202); 8 weeks later, treatment of KC;$Foxp3^{DTR}$ with diphtheria toxin for 3 weeks ablated Tregs (34). Given that Treg depletion does not alleviate immunosuppression (34), we sought out to characterize the transcriptional signature of the cells in Treg depleted PanIN microenvironment. We performed single cell RNA-sequencing (scRNA-seq) analysis on KC and KC;$FoxP3^{DTR}$ pancreata and visualized the data using uniform manifold approximation and projection (UMAP). Using established gene markers (49, 181, 183), we identified 17 distinct cell populations (**Fig. 4.1A-B, 4.2A**). Among these, fibroblasts in KC;$FoxP3^{DTR}$ clustered separately compared to fibroblasts in control KC, while other cells types shared an overlapping pattern of clustering (**Fig. 4.1B**). Interestingly, CD4 and CD8 T cells were present at a higher proportion in KC;$FoxP3^{DTR}$

group (**Fig. 4.1C**). To further investigate this, we subclustered the CD8 T cells and assessed their activation related gene expression profile, which revealed high expression of *Ifng*, *Gzmb, and Prf1* in cells from KC;FoxP3^{DTR} (**Fig. 4.1D-E**). We then examined their exhaustion status, CD8 T cells from KC;FoxP3^{DTR} group exhibited increased expression of *Gzmk*, *Lag3*, *Tox*, and *Pdcd1* (**Fig. 4.1D-E**). These data suggest that CD8 T cells in the Treg depleted mice have an exhausted transcriptional signature that likely contributes to the immunosuppressive microenvironment.

Treg depletion leads to increase in Th2 T cells and fibroblast reprogramming

To examine the impact on Treg depletion on CD4 T cells in the microenvironment, we subclustered CD4 T cells in the scRNA-seq data from KC and KC;FoxP3^{DTR} pancreata. Using conventional CD4 T cell linage markers (49, 181, 183), we were able to identify Naïve CD4 (CD4+, Tcf7+), Tregs (CD4+, Foxp3+) and Th2s (CD4+, Gata3+, Il4+), as well as ydT cells (Cd3+, Trdc+) cells (**Fig. 4.3A, 4.2B**). Remarkably, nearly all CD4 T cells in the KC;FoxP3^{DTR} exhibited Th2 T cell transcriptomic signature. Interrogation of genes involved in the function of CD4 T cells reveled that CD4s from KC;FoxP3^{DTR} expressed Th2 defining receptor genes *Il4ra*, *Il5ra*, and type 2 cytokine genes *Il13*, *Il4*, and *Il10* (**Fig.4.3B**). To investigate this further, we performed immunohistochemistry staining for Gata3 on KC and KC;FoxP3^{DTR} pancreata. Consistent with the scRNA-seq findings, we observed a striking ~4 fold increase in Gata3+ infiltrates in KC;FoxP3^{DTR} pancreata (**Fig. 4.3C**).

Since type 2 immune responses are known to regulate tissue repair, we next examined whether fibroblasts in the Treg depleted microenvironment engage in the type 2 immunity. Notably, fibroblasts in KC: FoxP3^{DTR} clustered distinctly from fibroblasts in KC (**Fig. 4.1B**). We subclustered the fibroblasts further to characterize their transcriptomic signature. In accordance with previous observations (34), KC;FoxP3^{DTR} fibroblasts express myeloid chemo-attractant genes such as *Ccl8* and *Ccl6*. Additionally, they lack myCAF gene signature indicated by low expression of *Acta2* and *Tagln* (**Fig. 4.3D-E**). On the other hand, intriguingly, type 2 receptor family genes Il4ra, and Il13ra1 were expressed robustly by KC;FoxP3^{DTR} fibroblasts relative to KC. These findings suggest that the fibroblast

reprogramming in Treg depleted mice could be resulted from responding to Th2 cells via the type 2 receptor signaling.

Fibroblast and Th2 T cell crosstalk may contribute to tumorigenesis in Treg depleted microenvironment

To understand whether there is a crosstalk between Th2 T cells and fibroblasts we performed ligand-receptor analysis using CellChat. While comparing the ligand-receptor pairs, we found that IL4 signaling to have the highest interaction score. Cell-Cell interaction network analysis revealed that Th2 cells were the main sources of IL4 signaling, while fibroblasts in the KC;Foxp3^{DTR} pancreas were the prominent receivers (**Fig. 4.4A**). To further investigate the interaction between Th2 T cells and fibroblasts, we employed an indirect co-culture system (**Fig.4.4B**). CD4 T cells from the tumor microenvironment of orthotopic tumors in wildtype or Foxp3^{DTR} mice upon DT treatments were isolated and indirectly co-cultured with normal fibroblasts using transwell plates for three days (**Fig. 4.4B**). We observed an increased Th2 cytokines (IL4, IL10, IL13) in the coculture media of Foxp3^{DTR} group (**Fig. 4.5A-B**) by ELISA indicating the presence of type II signaling. Bulk RNA sequencing (RNA-seq) was performed on the fibroblasts from the co-culture system. Principle Component Analysis (PCA) showed distinct profiles of fibroblasts co-cultured with (i) CD4 T cells from wildtype mice (WT), (ii) CD4 T cells from Foxp3-DTR mice (Foxp3^{DTR}) or in (iii) media alone (control) (**Fig. 4.4C**). Among the differentially expressed transcripts between WT and Foxp3^{DTR} groups, we observed genes associated with inflammatory profile such as *Ccl8*, *Ccl7*, *Cxcl1*, *Cxcl5*, *Il6* upregulated in Foxp3^{DTR} fibroblasts. Interestingly, genes associated with extra cellular matrix such as *Col3a1*, and *Col5a1* were upregulated in WT fibroblasts (**Fig. 4.4D**). We validated the results by qPCR, observing a ~10-fold increase in *Ccl8* mRNA levels in Foxp3^{DTR} fibroblasts relative to WT and control (**Fig. 4.5C**). Type 2 cytokines have been shown to activate the JAK-STAT pathway (201). Consistent with this, gene set enrichment analysis revealed activation of pathways such as IL2-STA5, TNFA-NFKB, and IL6-JAK-STAT3 in Foxp3^{DTR} fibroblasts (**Fig. 4.4E**). To gain a thorough understanding about whether fibroblasts are responsive to type II cytokines, we cultured normal pancreatic fibroblasts in (i) culturing media, (ii) IL-4, (iii) IL-13, or (iv) the combination of IL-4 and IL-

13 for 24hrs (**Fig. 4.5D**). Compared with control media, IL4 induced a ~1.5-fold increased expression of *Ccl8* in fibroblasts (**Fig. 4.5D**). Notably, IL-13 treatment or the combination of IL-4 and IL-13 treatments did not significantly alter the mRNA expression of *Ccl8* in fibroblasts (**Fig. 4.5D**). These results suggest that pancreatic fibroblasts respond to Th2 T cell stimuli, mainly to IL4.

Discussion

The mechanisms that contribute to immune suppression during the onset and progression of PDA remain incompletely understood. Crosstalk between fibroblasts and tumor-infiltrating immune cells is of significant interest due to the complex and heterogeneous nature of the TME in PDA. We provide the first report to our knowledge of Th2 T cells directly interacting with pancreatic fibroblasts. We describe a circuit where IL4 stimulation of fibroblasts results in the expression of myeloid chemo-attractant chemokines such as *Ccl8*, which could promote the recruitment of myeloid cells into the microenvironment. Furthermore, we demonstrate that Tregs play a critical role in limiting the type 2 immune response regulated by Th2 T cells (**Fig. 4.6**).

Immunotherapy has emerged as a powerful strategy for cancer treatment, however, in PDAC it has failed to improve patient outcomes due to upregulated expression of inhibitory immune checkpoint receptors on T lymphocytes (192, 193). There are insufficient effector T lymphocytes in the microenvironment to mount a robust anti-tumor immune response. The main factors that contribute to T cell dysfunction include dense fibrotic stroma, CD4 T cells, and myeloid cells (194, 195). We speculate that the high stromal density precludes infiltration of effector T lymphocytes while supporting activity of other cell types to promote tumor growth through mechanisms uncovered in this study. We highlight the unique role distinct CD4 T cells play in the PDAC microenvironment. Notably, depletion of Tregs at PanIN stage of tumorigenesis led to CD8 T cells infiltration, however, these T cells expressed an exhaustion transcriptional signature. While Th1 cells facilitate CD8 T cell activity and enhance anti-tumor responses (199), Th2 T cells diminishes CD8 T cell effector functions to promote tumor growth (32, 199). A study also demonstrated that infiltration of Th2 cells at a PanIN stage promotes tumorigenesis (201). In line with this, we observed that nearly all CD4 T cells in the Tregs depleted

microenvironment remarkably had a Th2 transcriptomic signature and increased Gata3+ infiltrates were present in the pancreas, which likely impact the effector function of CD8 T cells.

Stromal fibroblasts are a major source of immune regulatory cytokines/chemokines and have been demonstrated to interact with immune cells (203). How they are regulated in PDAC remains unclear. We have previously shown that depletion of Tregs re-programs the CAFs to express inflammatory cytokines such as *Ccl3*, *Ccl6*, and *Ccl8*, facilitating recruitment of immunosuppressive myeloid cells into the microenvironment (34). A study observed that depletion of Tregs in a chronic pancreatitis model prompted activation of type 2 immune response and increased pancreatic fibroblasts and fibrosis (204). A notable finding from our current study was the high expression of type 2 receptor family genes *Il4ra*, and *Il13ra1* in pancreas fibroblasts from Treg depleted mice. Interestingly, it was previously demonstrated that thymic stromal lymphopoietin secreted by pancreas cancer associated fibroblasts promotes Th2 T cell polarization (32). However, there is evidence to suggest that Th2 cells could also impact fibroblast secreteome, as shown in in vitro co-culture system, culturing normal fibroblasts indirectly with CD4 T cells isolated from the tumor microenvironment of Treg depleted resulted in fibroblasts having an inflammatory secreteome profile. Accordingly, IL-4 stimulation induced expression of *Ccl8* in fibroblasts-a feature of fibroblasts in Treg depleted microenvironment. These results suggest that Th2 T cells are capable of reprogramming pancreas fibroblasts to express myeloid recruiting cytokines. Furthermore, our data also provide evidence to suggest that IL4 signaling contributes to fibroblast differentiation. Considering that fibroblasts are heterogeneous in the microenvironment with tumor promoting and restrictive functions, more mechanistic studies are required to investigate the relationship between Th2 T cells and fibroblasts.

Methods

Animal Strains

Mice were housed in pathogen free conditions at the University of Michigan. KC;Foxp3^{DTR} mice were generated as described previously (34). Treg depletion in KC;Foxp3^{DTR} mice was achieved by treating the mice intraperitonealy with diphtheria toxin (DT) at 50ng/g

dose as detailed in the experimental paradigm. Pancreatitis was induced in 4–5-week-old mice by administration of 8 hourly intraperitoneal injections of caerulein (34).

Immunohistochemistry

Pancreas tissue was fixed in 10% neutral-buffered formalin for 24h, embedded in paraffin and serially sectioned 5 μm thick. Immunohistochemical for Gata3 (1:200 primary antibody) was performed post EDTA antigen retrieval (49). Images were acquired using Olympus BX53F microscope equipped with CellSens software. Areas of the stain in micrographs was quantified using ImageJ software.

Single cell RNA sequencing

Pancreas were processed into single-cell suspension as described previously and subjected to single-cell RNA sequencing using the NextGen 10x platform and reverse transcription reaction was performed at the University Sequencing Core. Approximately 50 ng of the amplified cDNA was used for each sample to construct the libraries. Paired-end sequencing was performed on the Novaseq 6000 Illumina sequencing platform.

Data analysis was performed using the Seurat R package version 4.0. Data were filtered, normalized, scaled to identify highly variable genes, then linear dimensional reduction was performed and cell clusters were identified as described previously (49, 181, 183). Differential expression analysis on the cell compartments was performed to delineate gene signatures. Pathway enrichment analysis using the ClusterProfiler package was performed to identify specific signaling pathways that were altered.

Orthotopic Surgeries

Orthotopic tumors were established in 6-8 weeks old C57BL/6 mice or Foxp3^{DTR} through the injection of 50uL of 50,000 7940B cells resuspended in 1:1 ratio of RPMI and Matrigel. Treg depletion in Foxp3^{DTR} mice was achieved by treating the mice intraperitonealy with diphtheria toxin (DT) at 50ng/g dose as detailed in the experimental paradigm.

In-direct Coculture Assay

Normal pancreas CD1-WT fibroblasts were grown in the bottom well of a trans-well setup for 24h in RPMI with 10% FBS and 1% Pen Strep. CD4 T cells isolated from the pancreas tumor microenvironment using magnetic cell sorting were plated in the top well of a trans-

well in the presence of aCD3 and aCD28 for 72h. Condition media was collected for Type 2 cytokine ELISA analysis and RNA was extracted from the fibroblasts using Qiagen kit. Then, cDNA was generated from the fibroblast RNA using complementary DNA kit. Quantitative real-time polymerase chain reaction analysis was performed using *Ccl8* primers as described previously (34), and *Ppia* was used as a housekeeping control.

Bulk RNA sequencing

RNA isolated from fibroblast in the in-direct co-culture assay was subjected to bulk RNA sequencing. Quality of the RNA was determined by the University of Michigan sequencing core and libraries were generated. Paired-end sequencing was performed on the Novaseq 6000 Illumina sequencing platform. Quality control of the data was performed as described previously (34) and data was analyzed using DESeq2 in R version 4.

Type 2 Cytokine Fibroblast Assay

Normal pancreas CD1-WT fibroblasts were plated in 6 well plate in RPMI with 10% FBS and 1% Pen Strep. The next day, 50ng/mL recombinant mouse IL4, IL13 or the combination of the cytokines was added to the media. RNA was extracted from the fibroblasts 24h later and cDNA was generated using complementary DNA kit. Quantitative real-time polymerase chain reaction analysis was performed using *Ccl8* primers as described previously, and *Ppia* was used as a housekeeping control.

Statical Analysis

Sample sizes were selected based on preliminary data from pilot experiments and previous published studies. Animal studies were performed after randomization. Unpaired Student t-test or two-way analysis of variance (ANOVA) was utilized for comparing experimental groups from staining and functional assays. Data were analyzed using Prism 9.0 (GraphPad Software). P values less than 0.05 were considered statistically significant and values are reported as means ± SD with the indicated sample size.

Acknowledgements

The work is supported in part by R01-CA268426 awarded to M.P.M. and T.L.F. Work in the M.P.M. laboratory was also supported by NIH/NCI grants R01-CA260752, R01-CA271510, U01-CA224145, U01-CA274154, and U54CA274371. Work in the T.L.F. laboratory was supported by NIH/NCI grant U01CA274154, NIH/National Institute of Diabetes and Digestive and Kidney Diseases (NIDDK) 5R01DK128102, and VA BLR&D Merit Award 5I01BX005777, P.K. was supported by NIH/National Institute of Allergy and Infectious Diseases T32-AI007413 and NIH/National Institute of General Medical Sciences (NIGMS) T32-GM113900. K.D. was supported by NIH/NCI F31-CA265085-01A1. Y.Z. was supported by R50 CA232985.

Author Contributions: P.K., Y.Z., M.P.D. designed the research. P.K., J.M., K.B., B.G., K.D., A.E., W.D., X.H. performed the experiments. P.K., J.M, performed data analysis. P.K., Y.Z., M.P.D. wrote the original draft of the manuscript. P.K., J.M, K.B., B.G., K.D., A.E., W.D., X.H., T.F, E.C, F.B., Y.Z., M.P.D. read and edited the manuscript. E.C., F.B., T.L.F., Y.Z., M.P.D. supervised and provided funding sources.

Figures

Figure 4.1

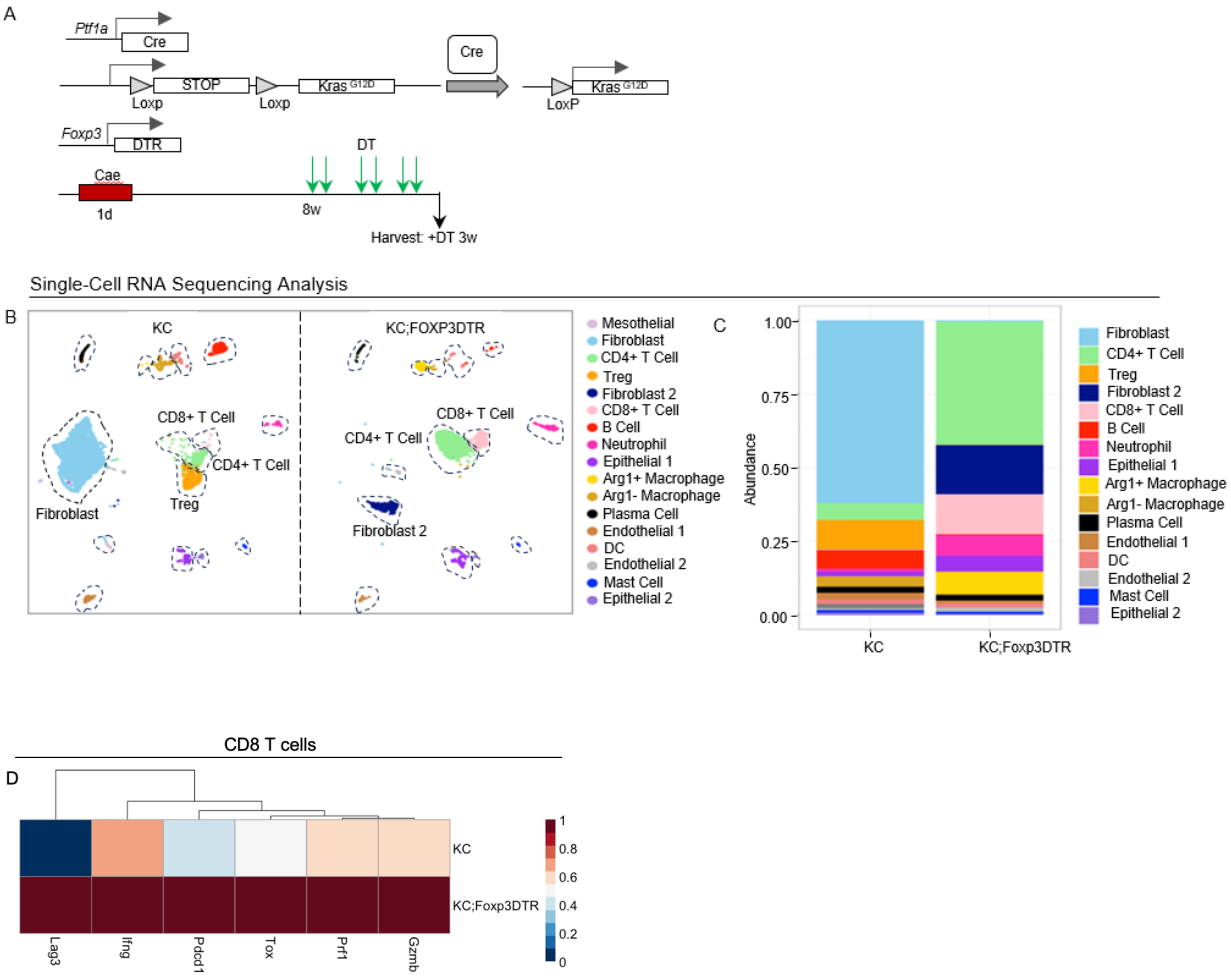


Figure 4.1 CD8 T cells in Treg depleted mice have an exhausted transcriptional signature. (A) Genetic makeup of the Kras$^{+/LSL-G12D}$;Ptf1a$^{Cre/+}$; Foxp3$^{tm3(DTR/GFP)Ayr}$ mouse model and experimental timeline for caeruelin and diphtheria toxin administration. (B) UMAP representation of identified cell population and (C) histogram of cell types abundance noted in KC and KC;Foxp3^{DTR} groups. (D) Heatmap of select genes associated with T cells' function. Average gene expression was based relative to highest expressor.

Figure 4.2

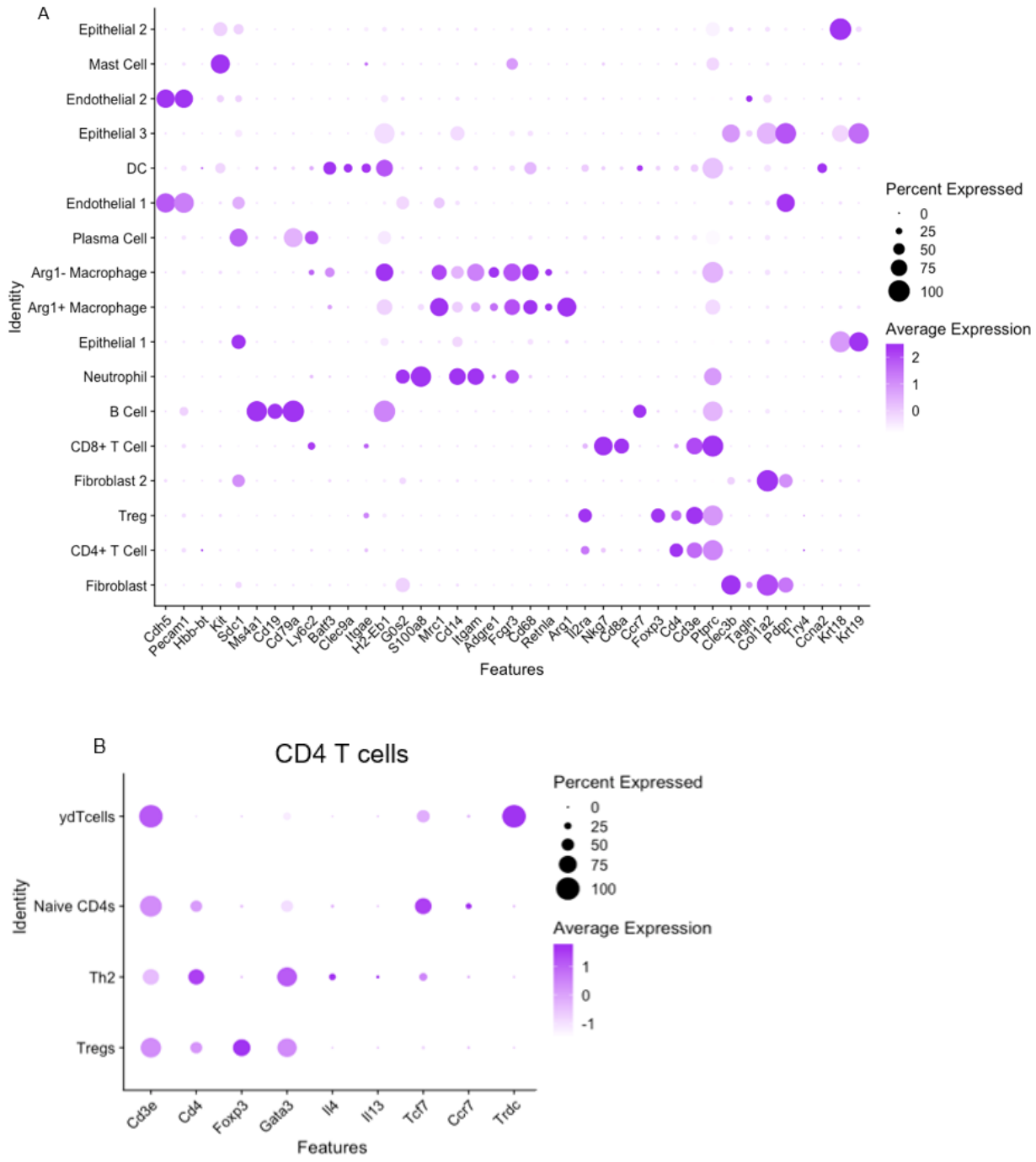


Figure 4.2 Single cell RNA-sequencing data of KC and KC;Foxp3^{DTR} mice. Dot plots of markers used to identify (A) all cell populations or (B) CD4 cell subtypes in KC and KC;Foxp3^{DTR} mice

Figure 4.3

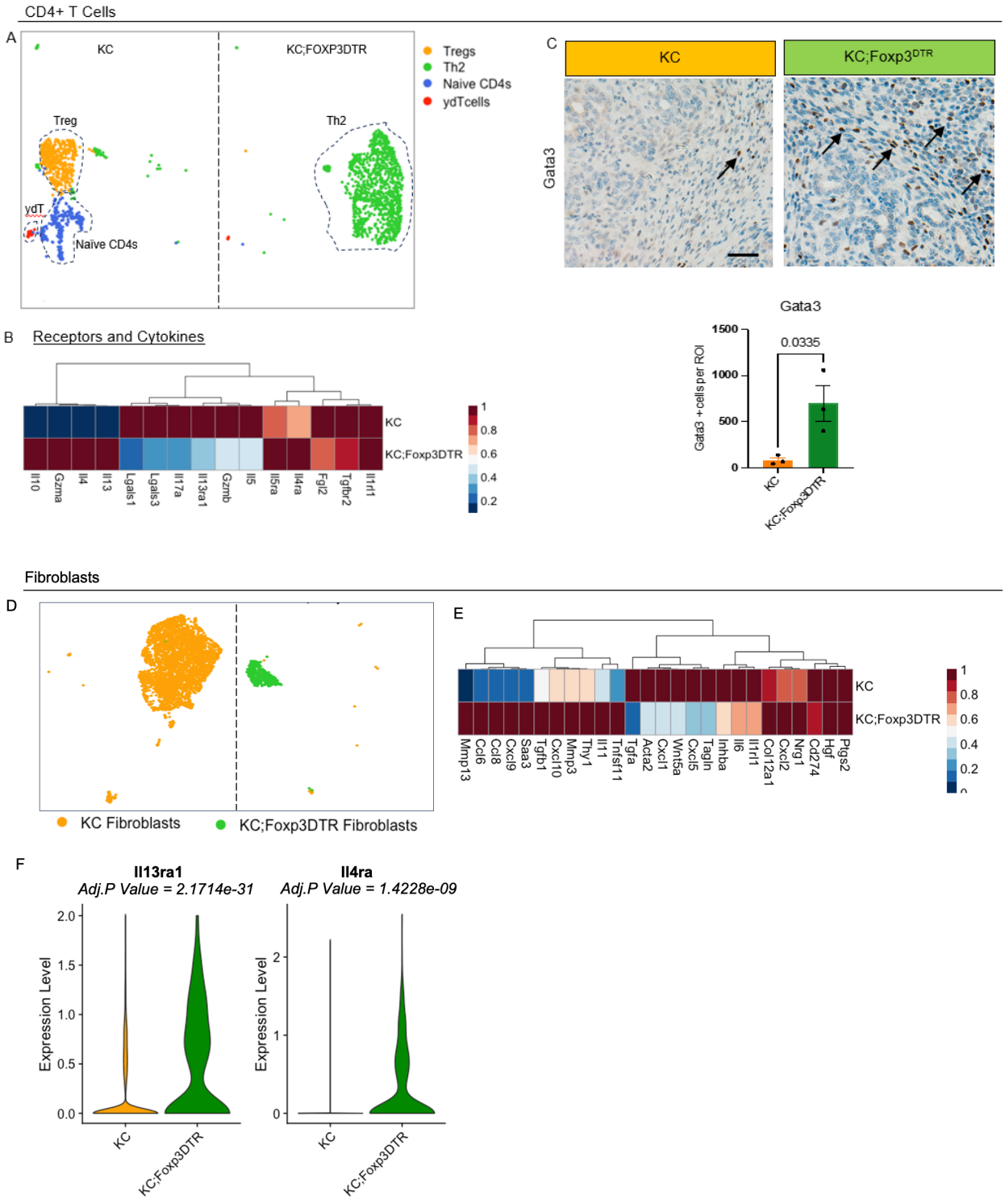

CD4+ T Cells
A
KC
KC;FOXP3DTR
Tregs
Th2
Naive CD4s
ydTcells
Treg
Th2
ydT
Naive CD4s
C
KC
KC;Foxp3DTR
Gata3
B
Receptors and Cytokines
KC
KC;Foxp3DTR
Il10
Gzma
Il4
Il13
Lgals1
Lgals3
Il17a
Il13ra1
Gzmb
Il5
Il5ra
Il4ra
Fgl2
Tgfbr2
Il1r1
1
0.8
0.6
0.4
0.2
Gata3
Gata3 + cells per ROI
1500
1000
500
0
0.0335
KC
KC;Foxp3DTR
Fibroblasts
D
KC Fibroblasts
KC;Foxp3DTR Fibroblasts
E
KC
KC;Foxp3DTR
Mmp13
Ccl6
Ccl8
Cxcl9
Saa3
Tgfb1
Cxcl10
Mmp3
Thy1
Il11
Tnfsf11
Tgfa
Acta2
Cxcl1
Wnt5a
Cxcl5
Tagln
Inhba
Il6
Il1r1
Col12a1
Cxcl2
Nrg1
Cd274
Hgf
Ptgs2
1
0.8
0.6
0.4
0.2
F
Il13ra1
Adj.P Value = 2.1714e-31
Il4ra
Adj.P Value = 1.4228e-09
Expression Level
2.0
1.5
1.0
0.5
0.0
2
1
0
KC
KC;Foxp3DTR

Figure 4.3 Depletion of Tregs results in increase in Th2 T cells and fibroblast reprogramming (A) UMAP overlay of re-clustered CD4 T cells from KC and KC;Foxp3^{DTR} groups. (B) Heatmap of select genes associated with CD4 T cells' function. Average gene expression was based relative to highest expressor (C) Immunohistochemistry for Gata3 in KC and KC;Foxp3^{DTR} pancreata. Scale bar = 50μm. Quantification of stain is depicted at the bottom, data represent mean ± SEM, n = 3 mice/group. Statical analysis was assessed by unpaired student t-test. $P < 0.05$ was considered significant. (D) UMAP overlay of re-clustered fibroblasts from KC and KC;Foxp3^{DTR} groups. (E) Heatmap of select genes associated with fibroblast secretome. Average gene expression was based relative to highest expressor. (F) Violin plots of normalized gene expression levels of type 2 receptor genes.

Figure 4.4

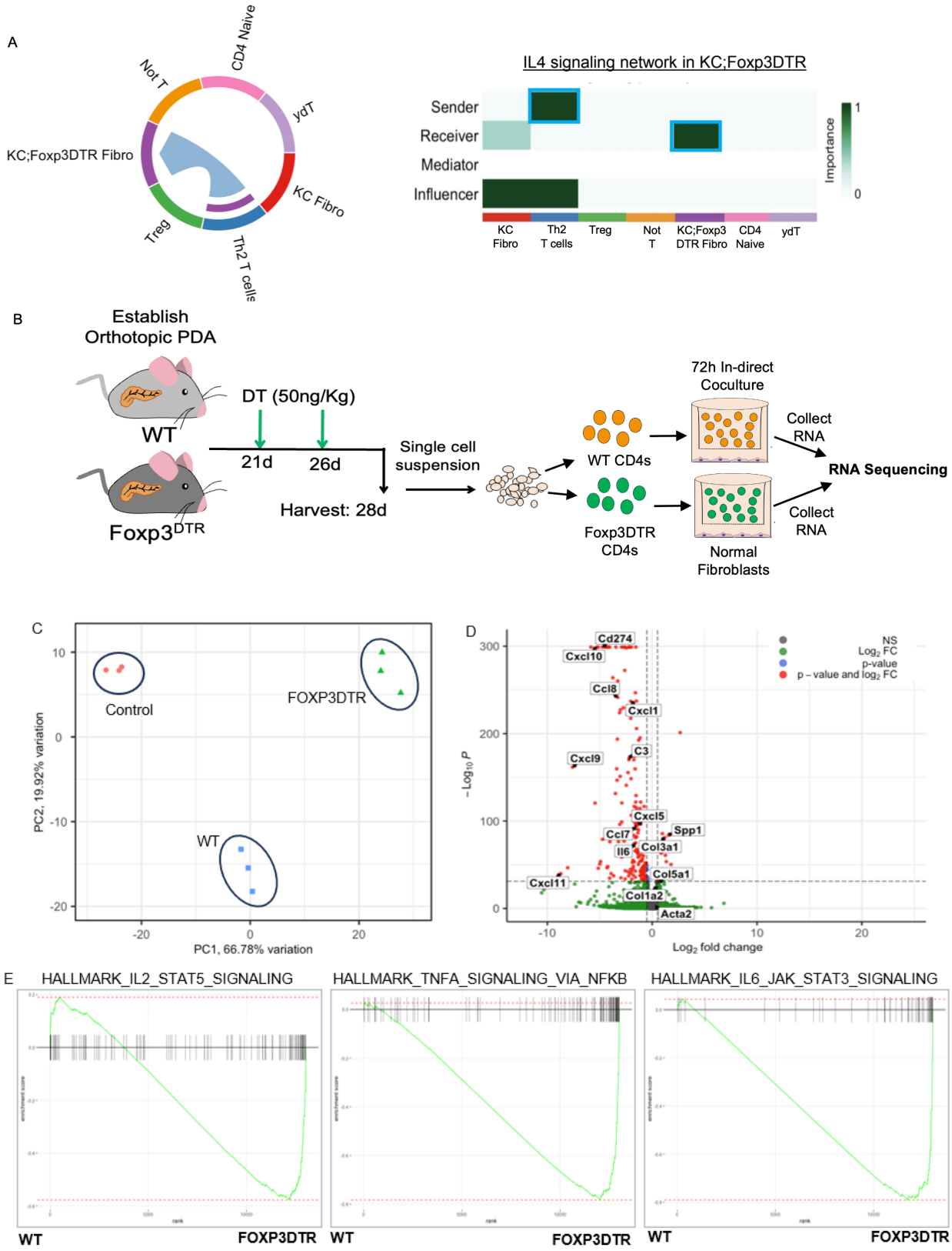

A
CD4 Naive
ydT
KC Fibro
Th2 T cells
Treg
KC;Foxp3DTR Fibro
Not T
IL4 signaling network in KC;Foxp3DTR
Sender
Receiver
Mediator
Influencer
Importance
1
0
KC Fibro
Th2 T cells
Treg
Not T
KC;Foxp3 DTR Fibro
CD4 Naive
ydT
B
Establish Orthotopic PDA
WT
Foxp3DTR
DT (50ng/Kg)
21d
26d
Harvest: 28d
Single cell suspension
WT CD4s
Foxp3DTR CD4s
72h In-direct Coculture
Normal Fibroblasts
Collect RNA
Collect RNA
RNA Sequencing
C
Control
FOXP3DTR
WT
PC2, 19.92% variation
PC1, 66.78% variation
D
Cd274
Cxcl10
Ccl8
Cxcl1
Cxcl9
C3
Cxcl5
Ccl7
Spp1
Il6
Col3a1
Col5a1
Cxcl11
Col1a2
Acta2
NS
Log2 FC
p-value
p – value and log2 FC
−Log10 P
Log2 fold change
E
HALLMARK_IL2_STAT5_SIGNALING
HALLMARK_TNFA_SIGNALING_VIA_NFKB
HALLMARK_IL6_JAK_STAT3_SIGNALING
WT
FOXP3DTR
WT
FOXP3DTR
WT
FOXP3DTR

Figure 4.4 CD4 T cells from Treg depleted tumor microenvironment reprogram pancreatic fibroblasts. (A) Cord diagram and cell interaction diagram of IL4 signaling pathway network analysis showing interactions between T cells and fibroblasts. (B) Experimental design of CD4 T cells and fibroblast indirect co-culture system. (C) PCA plot showing gene expression profile of Control, WT, FOXP3 fibroblasts. (D) Volcano plot of differentially expressed genes in WT and FOXP3 fibroblasts. (E) Gene set enrichment analysis of IL2-STAT5, TNFA-NFKB, and JAK-STAT3 signatures in WT fibroblasts compared to FOXP3 fibroblasts.

Figure 4.5

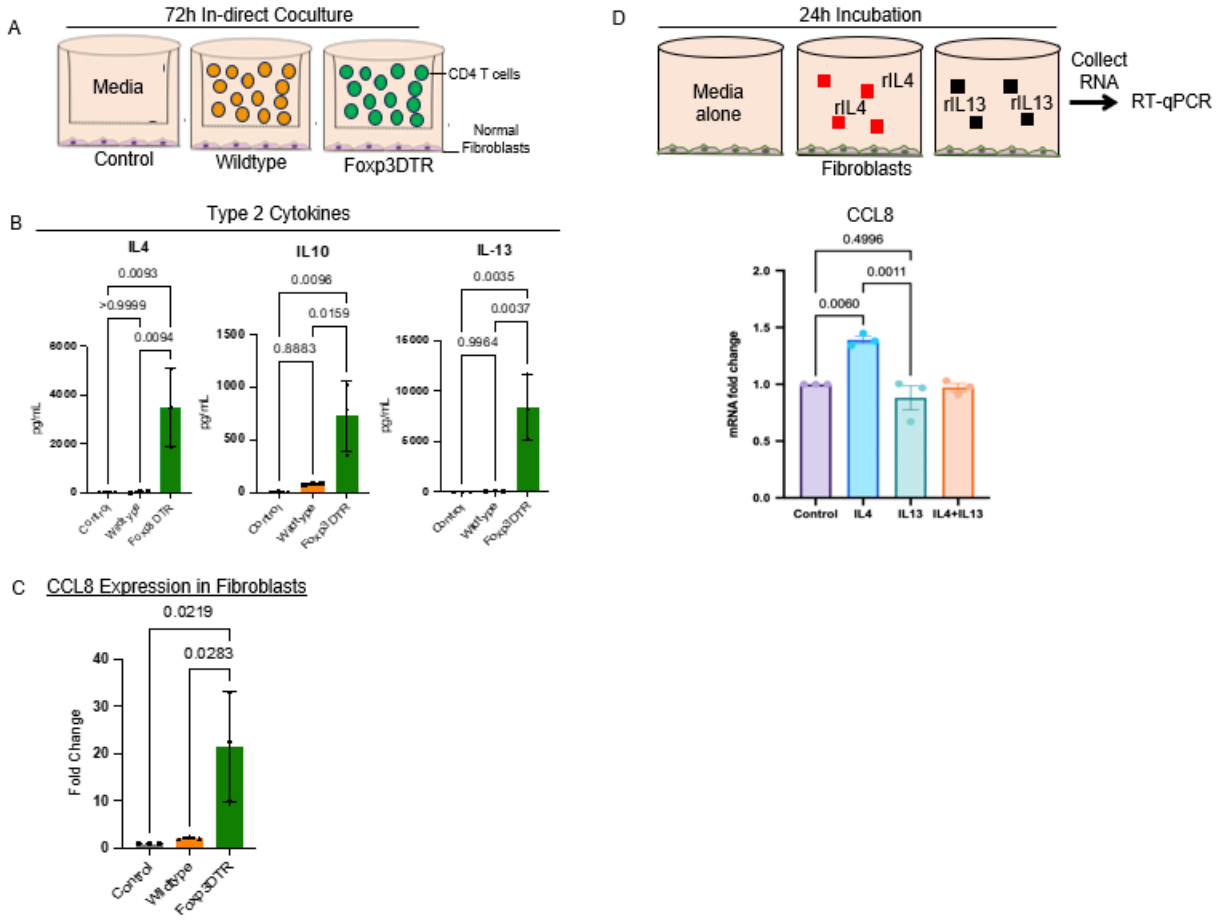


Figure 4.5 Type 2 cytokines reprogram pancreatic fibroblasts. (A) Experimental design of CD4 T cells and fibroblast indirect co-culture system. (B) Levels of type 2 cytokines IL-4, IL-10, and IL-13 in the condition media from CD4 T cells and fibroblast indirect co-culture system. (C) Realtime- quantitative PCR analysis for *Ccl8* expression in fibroblasts. n=3 biological replicates in Control, Wildtype, and Foxp3DTR groups. Statical analysis was assessed by one-way ANNOVA. $P < 0.05$ was considered significant. (D) Experimental design showing normal pancreatic fibroblasts being cultured with 50 ng/mL IL4, IL13 or the combination for 24h. Realtime- quantitative PCR analysis for *Ccl8* expression in fibroblasts. n=3 technical replicates. Statical analysis was assessed by one-way ANNOVA. $P < 0.05$ was considered significant.

Figure 4.6

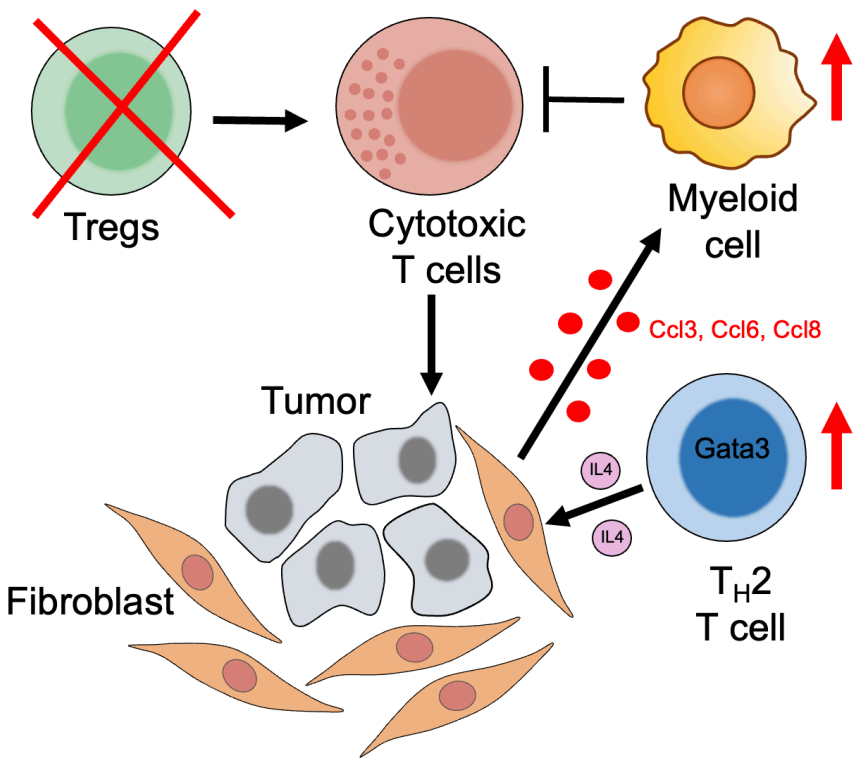


Figure 4.6 CD4 T cells and fibroblast crosstalk schematic. Upon Treg depletion, CD4 T cells are polarized to TH2 T cells and they directly interact with pancreatic fibroblasts to recruit myeloid cells into the microenvironment.

Chapter 5-Conclusions and Future Directions

Summary

Infiltration of immune cells into the PDAC microenvironment is well documented, and new studies are constantly uncovering the intricacies of the PDAC immune microenvironment. Studying nuances of the interplay between microenvironment and the immune system could lead to development of therapeutic strategies that are efficacious clinically.

Future Directions for Chapter 2

In chapter 2, we discovered that pancreata from healthy donors remarkably contained neoplastic lesions and the epithelial cells surrounding the lesions expressed KRAS mutations similar to pancreatic cancer cells. Furthermore, we noted that the fibroblasts in the PanIN microenvironment had a distinct transcriptomic signature relative to those in the tumor microenvironment. Heterogeneous population of CAFs with diverse functions contribute to poor therapeutic outcomes (203). Given that some precursor lesions remain quiescent while others progress to tumor, elucidating how the transcriptional programs in epithelial cells influence fibroblasts cell fate will be insightful. To understand the mechanisms contributing to cellular interactions, we developed a 3D ex-vivo organoid-fibroblast co-culture system using primary organoid and fibroblast cultures successfully derived from gift of life healthy donors or PDAC patients undergoing surgical resection (**Fig. 5.1A**,**B**). Our 3D ex-vivo model included the following mono- and co-culture groups: (a) tumor fibroblasts, (b) normal fibroblasts, (c) tumor organoids, (d) normal organoids, (e) matching tumor fibroblasts and tumor organoids, and (f) normal fibroblasts and tumor organoids. Notably, histological features of primary tumor were retained in the 3D fibroblast-organoid co-culture system (**Fig. 5.1C,D**). To assess the transcriptomic

changes in the mono- and co-cultures we performed sc-RNAseq analysis. The resulting data set comprised a total of 24,909 cells. UMAP visualization reveled distinct fibroblast and epithelial cell clusters that were annotated based previously established cell markers (41) (**Fig. 5.1E,F**). To elucidate the difference between fibroblasts in healthy relative to tumor cultures, we performed sub clustering on the fibroblasts. A total of 7 subclusters were identified, with clusters 4 and 5 common amongst all groups. Notably, clusters 1 and 7 were unique in tumor fibroblasts, while cluster 2 was unique to normal fibroblasts. Interestingly, cluster 3 was enriched in fibroblasts from matching tumor co-culture system, and cluster 6 was enriched in normal fibroblasts co-cultured with tumor organoids (**Fig. 5.1G**). Interestingly, we observed that fibroblasts in the matching tumor co-culture system have an enrichment of *IL33* relative to all other groups (**Fig. 5.1H**). Using in situ hybridization, we confirmed that the fibroblasts in the matching tumor co-culture system express IL33 (**Fig. 5.1I**) Currently, we are working on determining whether fibroblasts *in vitro* system retain transcriptional features of *in vivo* tumors. Since the 3D fibroblast-organoid co-culture system pancreatic tumor microenvironment is complex and the fibroblast-organoid system does not reflect tumor characteristics fully, we are also optimizing conditions to incorporate immune cells into the 3D co-culture system. This model will allow us to gain an understanding about how components of the microenvironment restrain or promote malignant transformation. Using this ex-vivo model, we can also elucidate tumor-specific as well as patient-specific features that contribute to therapeutic resistance.

Future Directions for Chapter 3

In Chapter 3 chapter, we strikingly observed that myeloid STAT3 activity drives the pathogenesis of new lesion formation and regulates immunosuppressive function of myeloid cells. Our study also had some limitations worth discussing. First, we did not assess the impact of *Stat3* loss in myeloid cells at later stages of tumorigenesis or in established tumors. Future work will investigate this by evaluating the direct effect of loss of *Stat3* in myeloid cells on epithelial cells and by determining how T cell functionality is transformed in the KFCS model. Similarly, investigating whether STAT3 activation in peripheral myeloid cells or pancreas resident myeloid cells plays a role in disease

pathogenesis is important. Furthermore, assessing if *Stat3* loss alters splenic or circulating myeloid cells' function through immunophenotyping will be insightful. Another limitation to the study was that as *LysM^{Cre};Stat3$^{f/f}$* mice aged, they became susceptible to chronic enterocolitis due to activation of type 1 helper T cell activity (205). Although mice with rectal prolapse were not included in the study, inflammation in the gastrointestinal tract may have impacted lesion formation in the pancreas.

Clinical trials targeting JAK/STAT signaling in PDAC have not met with success (180) and the studies have not dissected the contribution of therapeutics on non-tumor cells. While we noted that the loss of *Stat3* in myeloid cells impacted macrophage infiltration and function, fibroblasts in the microenvironment exhibited an anti-inflammatory gene signature due to *Stat3* dependency. Further validation studies are required to delineate the role of STAT3 signaling in different cell types in the microenvironment.

To assess whether STAT3 signaling in fibroblasts drives carcinogenesis we generated genetically engineered *Kras$^{Frt\text{-}STOP\text{-}Frt\text{-}G12D/+}$;Ptf1a$^{FlpO/+}$*; *Pdgfra^{CreER}* (KFPa) and *Kras$^{Frt\text{-}STOP\text{-}Frt\text{-}G12D/+}$;Ptf1a$^{FlpO/+}$*; *Pdgfra^{CreER};STAT3$^{f/f}$ (KFPaS) mice (***Fig. 5.2A***). Tamoxifen treatment allowed for the deletion of Stat3 specifically in Pdgfra+ fibroblasts. To promote lesion formation, we induced pancreatitis in mice (***Fig. 5.2B***).* We evaluated changes in the pancreas epithelium 3 weeks post treatment, the timepoint at which control KFPa mice exhibited lesions. Histological examination of the pancreas revealed decreased lesions in KFPaS mice relative to KFPa mice *(***Fig. 5.2C***)* These data suggest that loss of STAT3 activity in fibroblasts can reduce lesion formation in the pancreas.

We performed scRNA-seq analysis on the pancreas of KFPa (n=1) and KFPaS (n=1) mice. Using UMAP visualization, we identified transcriptomes of 16 cell types based on previously established canonical markers (49) (**Fig. 5.2D,E**). These cells included acinar cells (Muc1$^+$, Spink1$^+$, Amy1$^+$), epithelial cells (Cdh1$^+$, Krt19$^+$), endothelial 1 and 2 cells (Pecam1$^+$, Vwf$^+$), mesothelial cells (Msln$^+$, Pdgfra$^-$,Dcn$^+$), fibroblasts (Pdgfra$^+$,Dcn$^+$), macrophages (Ptprc$^+$, Itgam$^+$, C1q$^+$), T cells (Ptprc$^+$, Cd3e$^+$), B cells (Ptprc$^+$, Cd79a$^+$, Cd19$^+$), NK cells (Ptprc$^+$, Cd3e$^-$, Nkg7$^+$), dendritic cells (Ptprc$^+$, Itgam$^+$, Itgax$^+$), and proliferating cells (Ki67$^+$). To reveal differences in cell composition between KFC and KFCS conditions, we calculated the relative abundance of the 11 cell populations in the scRNA-seq data set. The relative abundance of fibroblasts, macrophages, B cells and T

cells decreased in the KFPaS group in comparison to KFPa, whereas relative abundance of acinar cells increased (**Fig. 5.2F**).

To further investigate transcriptomic changes in fibroblasts, we re-clustered them and observed a dramatic shift in the cell populations between the KFPa and KFPaS groups (**Fig. 5.2F**). Comparison of the differential gene expression of fibroblasts based on a selected list of genes revealed that fibroblasts in the KFPaS condition expressed genes associated with a pro-inflammatory state, including *Isg15, Isg20, Il1b, Ccl5,* and *IFNγ*-inducible chemokine ligands *Cxcl9* and *Cxcl10*. In contrast, fibroblasts in the KFPa group were enriched in genes associated with tumor development and invasion including *Il6, Saa3, Il33, Tnfsf11, Timp1,* and *Mmp3* (**Fig. 5.2F**). These data suggest that Stat3 activity in fibroblasts does play a major role in driving late-stage pancreatic tumorigenesis. The observed phenotype is from a single pair of mice in the study; for rigor, an increased sample number per experimental group is required. Nevertheless, our data highlight the important role JAK/STAT3 signaling plays in non-tumor cell in the pancreas. Targeting the signaling axis in both myeloid and fibroblast cells may be beneficial clinically.

Future Directions for Chapter 4

We and others have shown that one of the most abundant PDAC infiltrating immune cell types are CD4 T cells (32, 194, 201). The role CD4 T cell subsets play during the onset and progression of PDA is not well understood. Previously we have noted that that depletion of Tregs accelerates tumorigenesis due to fibroblasts assuming an inflammatory signature that promotes the recruitment of immunosuppressive myeloid cells in the microenvironment (34). In Chapter 4, we observed that depletion of Tregs results in significant increase in type 2 immune response in PanIN microenvironment. Notably, CD4 T cells assume a Th2 signature and fibroblasts have enriched expression of type 2 receptor genes Il4ra, and *Il13ra1*. We further identified that IL-4 signaling may contribute to the direct crosstalk between Th2 T cells and pancreas fibroblasts. It is also important to explore whether there is direct crosstalk between other CD4 T cell subsets and pancreatic fibroblasts. To evaluate this, an indirect co-culture was set up between CD4 T cell subsets and normal pancreas fibroblasts. Naïve CD4 T cells isolated from a wildtype mouse's spleen were polarized to Th1, Th2, or Th17 T cells. Three days later,

the differentiated T cells were indirectly co-cultured with pancreatic fibroblasts for an additional two days. We observed that levels of *Ccl8* expression was significantly higher in fibroblasts co-cultured with Th2 T cells in comparison to other CD4 T cell subsets, suggesting that pancreatic fibroblasts respond predominantly to Th2 T cell stimuli (**Fig. 5.3**). These data reveal that Th2 T cells play an important role in reprogramming fibroblasts.

A previous study has reported that PDAC patients with predominant Th2 (GATA3 expression) T cells show reduced survival compared with patients with higher levels of Th1 cells (32). We evaluated the levels of type 2 cytokines (IL4, IL10, IL13) in PDAC patients' serum. Patients were classified into non-progressive and progressive groups based on disease progression status over a time interval. In comparison to the initial target lesion diameter, patients that displayed a 30% or more increase in the diameter of the lesion or showed new lesion development were assigned to the progressive group. IL-4 and IL-13 levels were significantly higher in the serum of progressive patients relative to non-progressive patients (**Fig. 5.4**). Interestingly, levels of IL-4 were more prominent than other type 2 cytokines. These observations are in line with the results acquired in the Treg depleted mouse model and raise the possibility of targeting IL4 signaling in PDAC as a treatment modality.

It is known that type 2 immune responses are regulated by JAK/STAT signaling pathway and based on the RNA-seq data from Chapter 4 we established the activation STAT3 and STAT5 signaling in fibroblasts co-cultured with CD4 T cells isolated from Treg depleted microenvironment. To examine ligand-induced activation of signaling pathways in fibroblasts, we will need to further analyze Th2 T cell mediated activation of JAK/STAT pathway members. In parallel, we'll also have to investigate the effect of neutralizing type 2 cytokines on Th2 and fibroblast crosstalk in vitro as well as potential effects on tumorigenesis in vivo. Notably, IL-4 blocked has been shown inhibited growth of human PDAC cells (206) and decrease metastatic foci in lungs of mammary adenocarcinomas (200). Examining the role of Th2 T cells in PDAC progression as well as characterize the nature of intercellular crosstalk between Th2 T cells and fibroblasts in PDAC microenvironment could lead to identification of novel targets to complement current immunotherapy treatment modalities.

Final Remarks

With the current advances in genomic platforms, personalized medicine approaches, and multidisciplinary team collaborations, it is becoming evident that the survival rate for pancreatic cancer patients is improving. However, incidence of PDAC is still on the rise, requiring deeper understanding about the tumor microenvironment. Results from the dissertation provide some insight into the complicated cross-talk among fibroblasts, immune cells, and epithelial cells that mediate the immunosuppression in PDAC, which could lead to the development of novel strategies for the treatment of the disease.

Figures

Figure 5.1

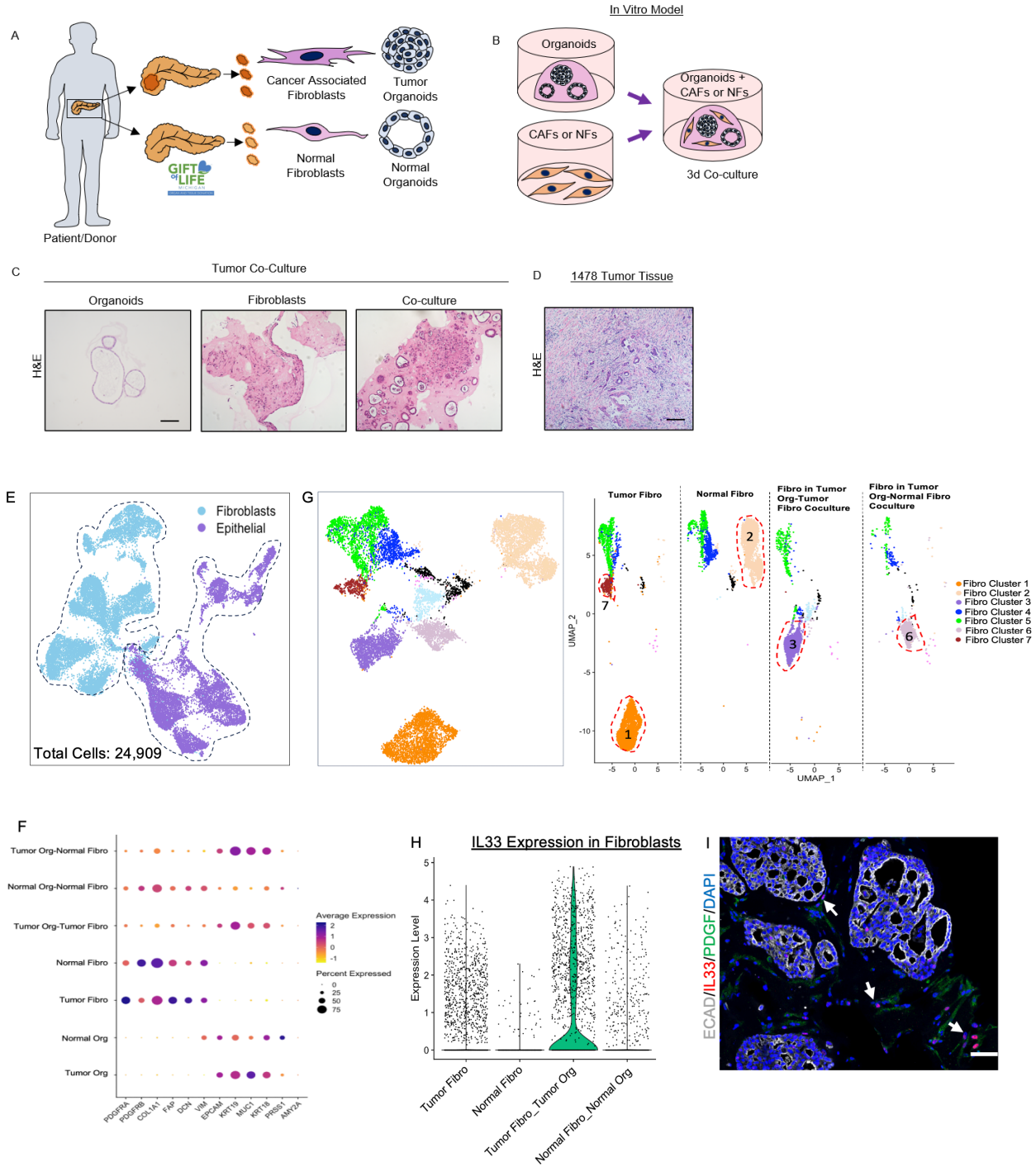


Figure 5.1 Fibroblast-Orgnaoid Co-culture system recapitulates features of primary tumor
(A) Derivation of primary fibroblast and organoid cultures from gift of life donors or PDAC patients (B) Establishement of mono- or Co-culture 3D system. (C) H&E staining of fibroblast and organoid mon- and co-cultures at day 3. Scale bar = 200 μm. (D) H&E stanning of primary tumor. Scale bar = 200 μm. (E) UMAP representation of identified cell population and (F) dot plot of markers used to identity cell types. (G) UMAP of re-clustered fibroblasts from tumor fibroblasts, normal fibroblasts, fibroblast from matching tumor co-culture, and fibroblasts from normal fibroblasts and tumor organoid co-culture. (H) Villon plot of IL33 expression in fibroblasts. (I) In situ hybridization of IL33 (red) with co-immunefluorescence of Ecad (grey), PDGFα/β (green), and DAPI (red). Scale bar = 50 μm.

Figure 5.2

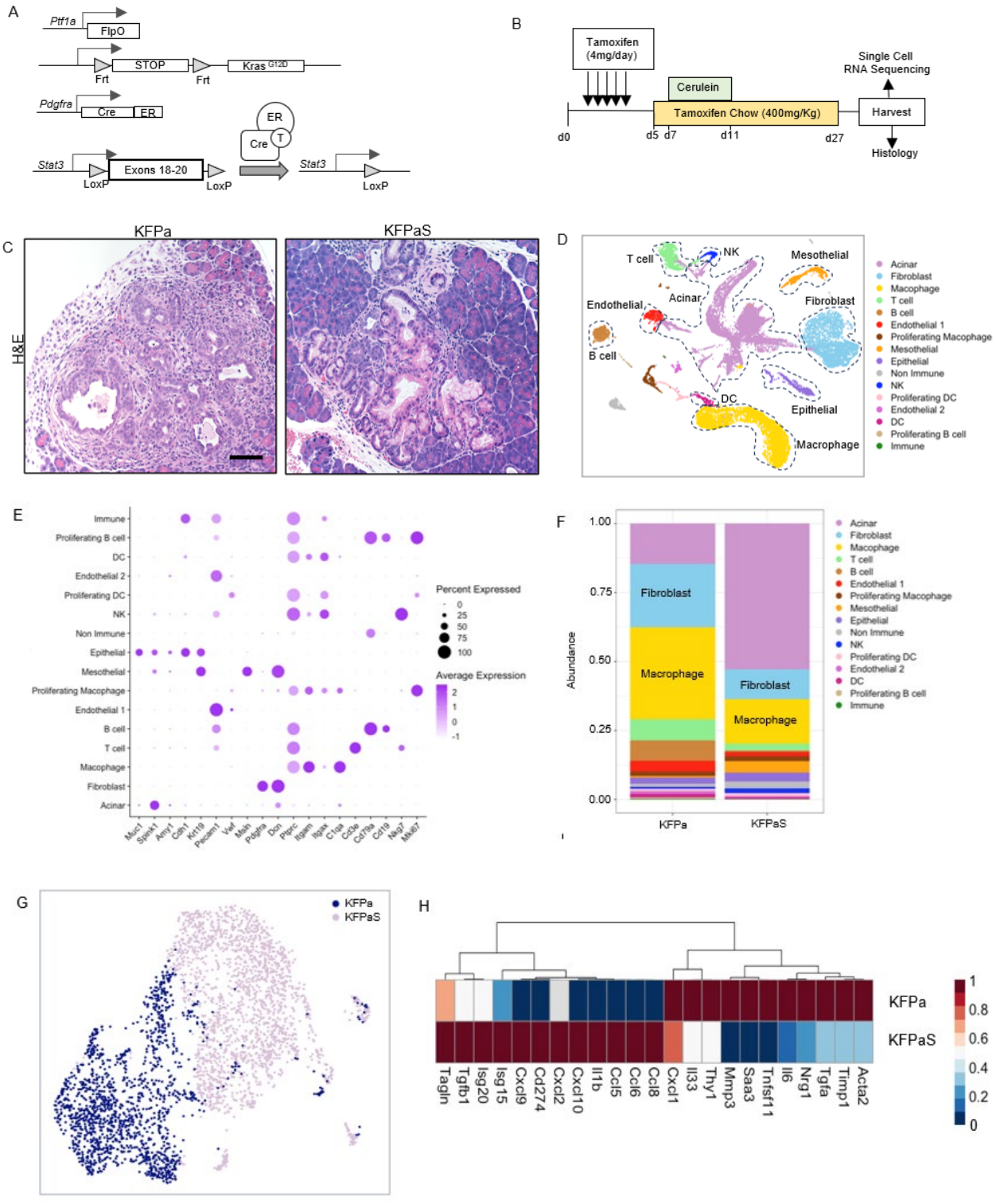

A
Ptf1a
FlpO
STOP
Frt
Frt
Kras G12D
Pdgfra
Cre
ER
Stat3
Exons 18-20
LoxP
LoxP
ER
Cre
T
Stat3
LoxP
B
Tamoxifen (4mg/day)
Cerulein
Tamoxifen Chow (400mg/Kg)
Single Cell RNA Sequencing
Harvest
Histology
d0
d5 d7
d11
d27
C
KFPa
KFPaS
H&E
D
T cell
NK
Mesothelial
Endothelial
Acinar
Fibroblast
B cell
DC
Epithelial
Macrophage
Acinar
Fibroblast
Macophage
T cell
B cell
Endothelial 1
Proliferating Macophage
Mesothelial
Epithelial
Non Immune
NK
Proliferating DC
Endothelial 2
DC
Proliferating B cell
Immune
E
Immune
Proliferating B cell
DC
Endothelial 2
Proliferating DC
NK
Non Immune
Epithelial
Mesothelial
Proliferating Macophage
Endothelial 1
B cell
T cell
Macophage
Fibroblast
Acinar
Muc1
Spink1
Amy1
Cdh1
Krt19
Pecam1
Vwf
Msln
Pdgfra
Dcn
Ptprc
Itgam
Itgax
C1qa
Cd3e
Cd79a
Cd19
Ncr1
Mki67
Percent Expressed
0
25
50
75
100
Average Expression
2
1
0
-1
F
Abundance
1.00
0.75
0.50
0.25
0.00
Fibroblast
Macophage
Fibroblast
Macophage
KFPa
KFPaS
Acinar
Fibroblast
Macophage
T cell
B cell
Endothelial 1
Proliferating Macophage
Mesothelial
Epithelial
Non Immune
NK
Proliferating DC
Endothelial 2
DC
Proliferating B cell
Immune
G
KFPa
KFPaS
H
KFPa
KFPaS
1
0.8
0.6
0.4
0.2
0
Tagln
Tgfb1
Isg20
Isg15
Cxcl9
Cd274
Cxcl2
Cxcl10
Il1b
Ccl5
Ccl6
Ccl8
Cxcl1
Il33
Thy1
Mmp3
Saa3
Tnfsf11
Il6
Nrg1
Tgfa
Timp1
Acta2

Figure 5.2 STAT3 activation in fibroblasts is required for lesion formation.
(A) Genetic makeup of the $Kras^{Frt\text{-}STOP\text{-}Frt\text{-}G12D/+}$;$Ptf1a^{FlipO/+}$;$Pdgfra^{CreER}$;$Stat3^{f/f}$ mouse model. (B) Experimental design. Tamoxifen was given to mice for 5 days to delete Stat3 in $Pdgfra^{+}$ cells. The mice were then put on tamoxifen chow until the end of the experiment. On day 7, mice were administered caerulein for 5 days to induce pancreatitis. Pancreata were harvested on day 27. (C) H&E staining of KFPa and KFPaS pancreas. Scale bar = 200 μm (n=1 mouse). (D) UMAP representation of identified cell population and (E) dot plot of markers used to identity cell types. (F) Histogram of cell type abundance noted in KFC and KFCS groups. (G) UMAP overlay of re-clustered fibroblasts from KFPa and KFPaS groups. (H) Heatmap of curated genes associated with fibroblast secretome. Average gene expression was based relative to highest expressor.

Figure 5.3

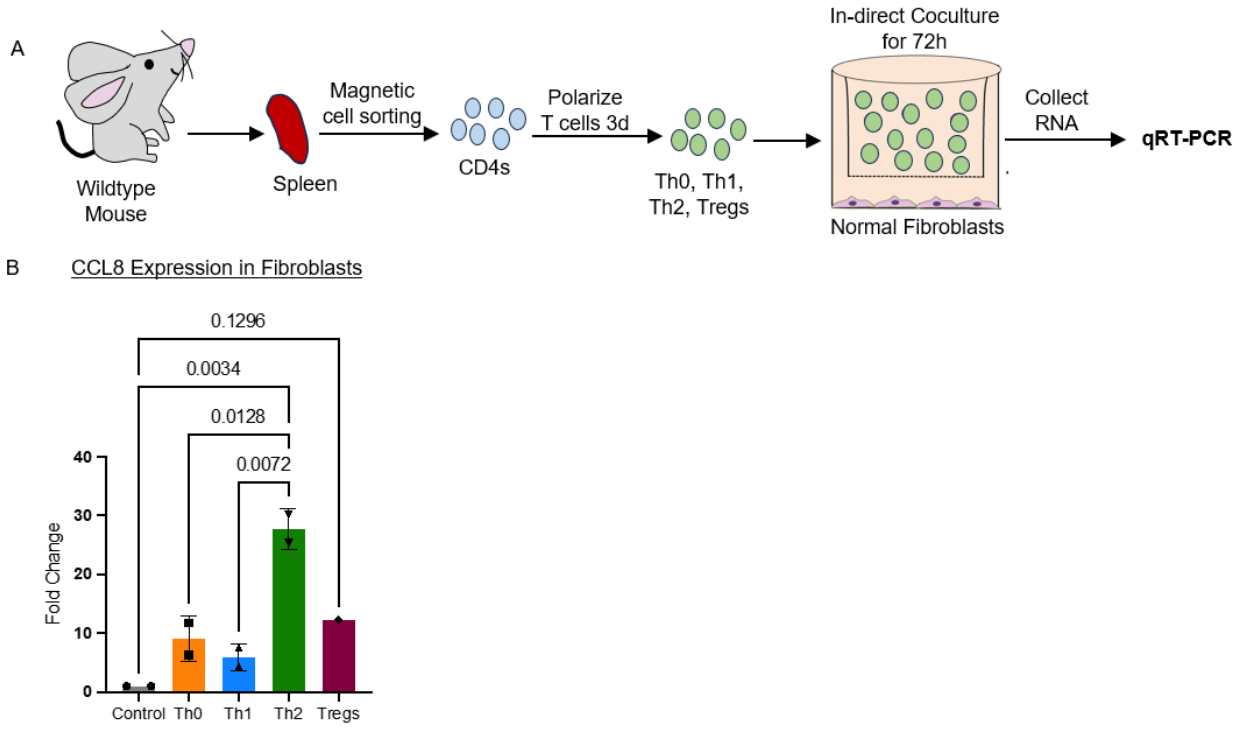


Figure 5.3 Fibroblasts express high *Ccl8* when co-cultured with Th2 T cells. (A) Experimental Design. (B) RT-PCR for *Ccl8* levels in fibroblasts co-cultured with culturing media (Control) Th0, Th1, Th2 or Tregs for 3 days. Data represents mean ± SEM, n=2 replicates. Statistical difference was determined by one-way ANOVA.

Figure 5.4

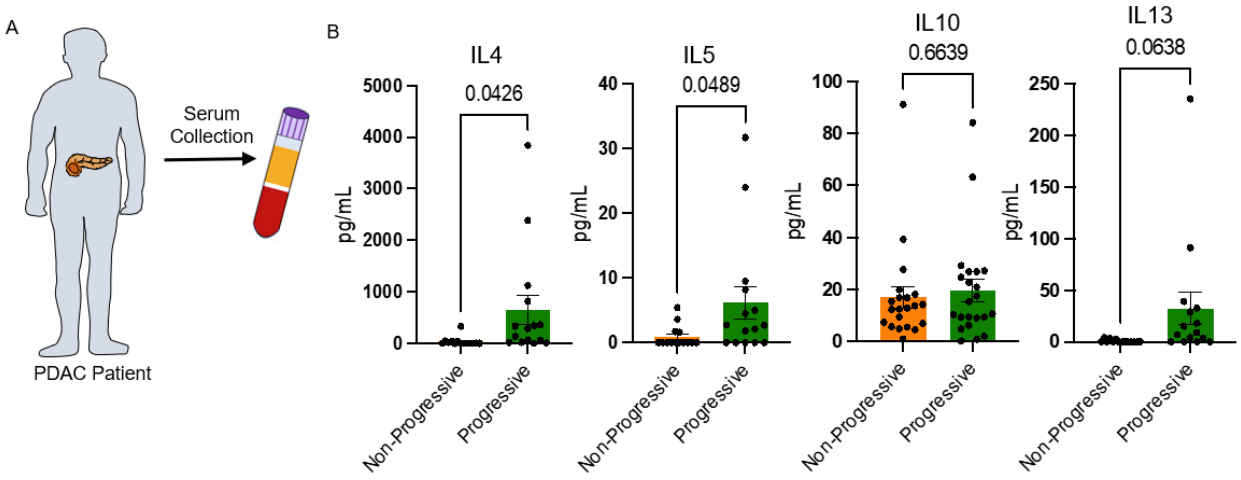


Figure 5.4 Levels of type 2 cytokines in PDAC patient serum (A) Blood was collected from PDAC patients. (B) Levels of serum IL-4, IL-5, IL-10, and IL-13 in non-progressive and progressive patients. Statical analysis was assessed by unpaired student t-test. $P < 0.05$ was considered significant

Bibliography

1. Rawla P, Sunkara T, and Gaduputi V. Epidemiology of Pancreatic Cancer: Global Trends, Etiology and Risk Factors. *World J Oncol.* 2019;10(1):10-27.
2. Paiella S, De Pastena M, D'Onofrio M, Crinò SF, Pan TL, De Robertis R, et al. Palliative therapy in pancreatic cancer-interventional treatment with radiofrequency ablation/irreversible electroporation. *Transl Gastroenterol Hepatol.* 2018;3:80.
3. De Simoni O, Scarpa M, Soldà C, Bergamo F, Lonardi S, Fantin A, et al. Could Total Neoadjuvant Therapy Followed by Surgical Resection Be the New Standard of Care in Pancreatic Cancer? A Systematic Review and Meta-Analysis. *J Clin Med.* 2022;11(3).
4. Becker AE, Hernandez YG, Frucht H, and Lucas AL. Pancreatic ductal adenocarcinoma: risk factors, screening, and early detection. *World J Gastroenterol.* 2014;20(32):11182-98.
5. Guerra C, and Barbacid M. Genetically engineered mouse models of pancreatic adenocarcinoma. *Mol Oncol.* 2013;7(2):232-47.
6. Distler M, Aust D, Weitz J, Pilarsky C, and Grützmann R. Precursor lesions for sporadic pancreatic cancer: PanIN, IPMN, and MCN. *Biomed Res Int.* 2014;2014:474905.
7. Shi C, Klein AP, Goggins M, Maitra A, Canto M, Ali S, et al. Increased Prevalence of Precursor Lesions in Familial Pancreatic Cancer Patients. *Clin Cancer Res.* 2009;15(24):7737-43.
8. Klein WM, Hruban RH, Klein-Szanto AJ, and Wilentz RE. Direct correlation between proliferative activity and dysplasia in pancreatic intraepithelial neoplasia (PanIN): additional evidence for a recently proposed model of progression. *Mod Pathol.* 2002;15(4):441-7.
9. Polani F, Grierson PM, and Lim KH. Stroma-targeting strategies in pancreatic cancer: Past lessons, challenges and prospects. *World J Gastroenterol.* 2021;27(18):2105-21.
10. Helms E, Onate MK, and Sherman MH. Fibroblast Heterogeneity in the Pancreatic Tumor Microenvironment. *Cancer Discov.* 2020;10(5):648-56.
11. Arina A, Idel C, Hyjek EM, Alegre ML, Wang Y, Bindokas VP, et al. Tumor-associated fibroblasts predominantly come from local and not circulating precursors. *Proc Natl Acad Sci U S A.* 2016;113(27):7551-6.
12. Petersen OW, Nielsen HL, Gudjonsson T, Villadsen R, Rank F, Niebuhr E, et al. Epithelial to mesenchymal transition in human breast cancer can provide a nonmalignant stroma. *Am J Pathol.* 2003;162(2):391-402.
13. Iwamoto C, Ohuchida K, Shinkawa T, Okuda S, Otsubo Y, Okumura T, et al. Bone marrow-derived macrophages converted into cancer-associated fibroblast-like cells promote pancreatic cancer progression. *Cancer Lett.* 2021;512:15-27.
14. Brichkina A, Polo P, Sharma SD, Visestamkul N, and Lauth M. A Quick Guide to CAF Subtypes in Pancreatic Cancer. *Cancers (Basel).* 2023;15(9).
15. Öhlund D, Handly-Santana A, Biffi G, Elyada E, Almeida AS, Ponz-Sarvise M, et al. Distinct populations of inflammatory fibroblasts and myofibroblasts in pancreatic cancer. *J Exp Med.* 2017;214(3):579-96.

16. Chen K, Wang Q, Li M, Guo H, Liu W, Wang F, et al. Single-cell RNA-seq reveals dynamic change in tumor microenvironment during pancreatic ductal adenocarcinoma malignant progression. *EBioMedicine.* 2021;66:103315.
17. Biffi G, Oni TE, Spielman B, Hao Y, Elyada E, Park Y, et al. IL1-Induced JAK/STAT Signaling Is Antagonized by TGFβ to Shape CAF Heterogeneity in Pancreatic Ductal Adenocarcinoma. *Cancer Discov.* 2019;9(2):282-301.
18. Huang H, Wang Z, Zhang Y, Pradhan RN, Ganguly D, Chandra R, et al. Mesothelial cell-derived antigen-presenting cancer-associated fibroblasts induce expansion of regulatory T cells in pancreatic cancer. *Cancer Cell.* 2022;40(6):656-73.e7.
19. Tsujikawa T, Kumar S, Borkar RN, Azimi V, Thibault G, Chang YH, et al. Quantitative Multiplex Immunohistochemistry Reveals Myeloid-Inflamed Tumor-Immune Complexity Associated with Poor Prognosis. *Cell Rep.* 2017;19(1):203-17.
20. Diaz-Montero CM, Salem ML, Nishimura MI, Garrett-Mayer E, Cole DJ, and Montero AJ. Increased circulating myeloid-derived suppressor cells correlate with clinical cancer stage, metastatic tumor burden, and doxorubicin-cyclophosphamide chemotherapy. *Cancer Immunol Immunother.* 2009;58(1):49-59.
21. Zhang Y, Velez-Delgado A, Mathew E, Li D, Mendez FM, Flannagan K, et al. Myeloid cells are required for PD-1/PD-L1 checkpoint activation and the establishment of an immunosuppressive environment in pancreatic cancer. *Gut.* 2017;66(1):124-36.
22. Sanford DE, Belt BA, Panni RZ, Mayer A, Deshpande AD, Carpenter D, et al. Inflammatory monocyte mobilization decreases patient survival in pancreatic cancer: a role for targeting the CCL2/CCR2 axis. *Clin Cancer Res.* 2013;19(13):3404-15.
23. Zhu Y, Knolhoff BL, Meyer MA, Nywening TM, West BL, Luo J, et al. CSF1/CSF1R blockade reprograms tumor-infiltrating macrophages and improves response to T-cell checkpoint immunotherapy in pancreatic cancer models. *Cancer Res.* 2014;74(18):5057-69.
24. Siret C, Collignon A, Silvy F, Robert S, Cheyrol T, Andre P, et al. Deciphering the Crosstalk Between Myeloid-Derived Suppressor Cells and Regulatory T Cells in Pancreatic Ductal Adenocarcinoma. *Front Immunol.* 2019;10:3070.
25. Zhang Y, Yan W, Mathew E, Kane KT, Brannon A, Adoumie M, et al. Epithelial-Myeloid cell crosstalk regulates acinar cell plasticity and pancreatic remodeling in mice. *Elife.* 2017;6.
26. Kaneda MM, Cappello P, Nguyen AV, Ralainirina N, Hardamon CR, Foubert P, et al. Macrophage PI3Kgamma Drives Pancreatic Ductal Adenocarcinoma Progression. *Cancer Discov.* 2016;6(8):870-85.
27. DuPage M, and Bluestone JA. Harnessing the plasticity of CD4(+) T cells to treat immune-mediated disease. *Nat Rev Immunol.* 2016;16(3):149-63.
28. Saillard M, Cenerenti M, Romero P, and Jandus C. Impact of Immunotherapy on CD4 T Cell Phenotypes and Function in Cancer. *Vaccines (Basel).* 2021;9(5).
29. Miggelbrink AM, Jackson JD, Lorrey SJ, Srinivasan ES, Waibl-Polania J, Wilkinson DS, and Fecci PE. CD4 T-Cell Exhaustion: Does It Exist and What Are Its Roles in Cancer? *Clin Cancer Res.* 2021;27(21):5742-52.
30. Christie D, and Zhu J. Transcriptional regulatory networks for CD4 T cell differentiation. *Curr Top Microbiol Immunol.* 2014;381:125-72.
31. Golubovskaya V, and Wu L. Different Subsets of T Cells, Memory, Effector Functions, and CAR-T Immunotherapy. *Cancers (Basel).* 2016;8(3).
32. De Monte L, Reni M, Tassi E, Clavenna D, Papa I, Recalde H, et al. Intratumor T helper type 2 cell infiltrate correlates with cancer-associated fibroblast thymic stromal lymphopoietin production and reduced survival in pancreatic cancer. *J Exp Med.* 2011;208(3):469-78.

33. Mucciolo G, Curcio C, Roux C, Li WY, Capello M, Curto R, et al. IL17A critically shapes the transcriptional program of fibroblasts in pancreatic cancer and switches on their protumorigenic functions. *Proc Natl Acad Sci U S A.* 2021;118(6).
34. Zhang Y, Lazarus J, Steele NG, Yan W, Lee HJ, Nwosu ZC, et al. Regulatory T-cell Depletion Alters the Tumor Microenvironment and Accelerates Pancreatic Carcinogenesis. *Cancer Discov.* 2020;10(3):422-39.
35. Masugi Y, Abe T, Ueno A, Fujii-Nishimura Y, Ojima H, Endo Y, et al. Characterization of spatial distribution of tumor-infiltrating CD8(+) T cells refines their prognostic utility for pancreatic cancer survival. *Mod Pathol.* 2019;32(10):1495-507.
36. Carstens JL, Correa de Sampaio P, Yang D, Barua S, Wang H, Rao A, et al. Spatial computation of intratumoral T cells correlates with survival of patients with pancreatic cancer. *Nat Commun.* 2017;8:15095.
37. Fukunaga A, Miyamoto M, Cho Y, Murakami S, Kawarada Y, Oshikiri T, et al. CD8+ tumor-infiltrating lymphocytes together with CD4+ tumor-infiltrating lymphocytes and dendritic cells improve the prognosis of patients with pancreatic adenocarcinoma. *Pancreas.* 2004;28(1):e26-31.
38. Fridman WH, Zitvogel L, Sautès-Fridman C, and Kroemer G. The immune contexture in cancer prognosis and treatment. *Nat Rev Clin Oncol.* 2017;14(12):717-34.
39. Cui W, and Kaech SM. Generation of effector CD8+ T cells and their conversion to memory T cells. *Immunol Rev.* 2010;236:151-66.
40. Seifert L, Plesca I, Müller L, Sommer U, Heiduk M, von Renesse J, et al. LAG-3-Expressing Tumor-Infiltrating T Cells Are Associated with Reduced Disease-Free Survival in Pancreatic Cancer. *Cancers (Basel).* 2021;13(6).
41. Steele NG, Carpenter ES, Kemp SB, Sirihorachai VR, The S, Delrosario L, et al. Multimodal Mapping of the Tumor and Peripheral Blood Immune Landscape in Human Pancreatic Cancer. *Nat Cancer.* 2020;1(11):1097-112.
42. Shen T, Zhou L, Shen H, Shi C, Jia S, Ding GP, and Cao L. Prognostic value of programmed cell death protein 1 expression on CD8+ T lymphocytes in pancreatic cancer. *Sci Rep.* 2017;7(1):7848.
43. Elyada E, Bolisetty M, Laise P, Flynn WF, Courtois ET, Burkhart RA, et al. Cross-Species Single-Cell Analysis of Pancreatic Ductal Adenocarcinoma Reveals Antigen-Presenting Cancer-Associated Fibroblasts. *Cancer Discov.* 2019;9(8):1102-23.
44. Peng J, Sun BF, Chen CY, Zhou JY, Chen YS, Chen H, et al. Single-cell RNA-seq highlights intra-tumoral heterogeneity and malignant progression in pancreatic ductal adenocarcinoma. *Cell Res.* 2019;29(9):725-38.
45. Raghavan S, Winter PS, Navia AW, Williams HL, DenAdel A, Lowder KE, et al. Microenvironment drives cell state, plasticity, and drug response in pancreatic cancer. *Cell.* 2021;184(25):6119-37 e26.
46. Steele NG, Carpenter ES, Kemp SB, Sirihorachai V, The S, Delrosario L, et al. Multimodal Mapping of the Tumor and Peripheral Blood Immune Landscape in Human Pancreatic Cancer. *Nat Cancer.* 2020;1(11):1097-112.
47. Bernard V, Semaan A, Huang J, San Lucas FA, Mulu FC, Stephens BM, et al. Single-Cell Transcriptomics of Pancreatic Cancer Precursors Demonstrates Epithelial and Microenvironmental Heterogeneity as an Early Event in Neoplastic Progression. *Clin Cancer Res.* 2019;25(7):2194-205.
48. Hwang WL, Jagadeesh KA, Guo JA, Hoffman HI, Yadollahpour P, Mohan R, et al. Single-nucleus and spatial transcriptomics of archival pancreatic cancer reveals multi-compartment reprogramming after neoadjuvant treatment. *bioRxiv.* 2020:2020.08.25.267336.

49. Velez-Delgado A, Donahue KL, Brown KL, Du W, Irizarry-Negron V, Menjivar RE, et al. Extrinsic KRAS Signaling Shapes the Pancreatic Microenvironment Through Fibroblast Reprogramming. *Cell Mol Gastroenterol Hepatol.* 2022;13(6):1673-99.
50. Sun L, Wang Q, Chen B, Zhao Y, Shen B, Wang H, et al. Gastric cancer mesenchymal stem cells derived IL-8 induces PD-L1 expression in gastric cancer cells via STAT3/mTOR-c-Myc signal axis. *Cell Death Dis.* 2018;9(9):928.
51. Johnson DE, O'Keefe RA, and Grandis JR. Targeting the IL-6/JAK/STAT3 signalling axis in cancer. *Nat Rev Clin Oncol.* 2018;15(4):234-48.
52. Corcoran RB, Contino G, Deshpande V, Tzatsos A, Conrad C, Benes CH, et al. STAT3 plays a critical role in KRAS-induced pancreatic tumorigenesis. *Cancer Res.* 2011;71(14):5020-9.
53. Darnell JE, Jr. STATs and gene regulation. *Science.* 1997;277(5332):1630-5.
54. Hu X, Li J, Fu M, Zhao X, and Wang W. The JAK/STAT signaling pathway: from bench to clinic. *Signal Transduct Target Ther.* 2021;6(1):402.
55. Scholz A, Heinze S, Detjen KM, Peters M, Welzel M, Hauff P, et al. Activated signal transducer and activator of transcription 3 (STAT3) supports the malignant phenotype of human pancreatic cancer. *Gastroenterology.* 2003;125(3):891-905.
56. Toyonaga T, Nakano K, Nagano M, Zhao G, Yamaguchi K, Kuroki S, et al. Blockade of constitutively activated Janus kinase/signal transducer and activator of transcription-3 pathway inhibits growth of human pancreatic cancer. *Cancer Lett.* 2003;201(1):107-16.
57. Lee JY, and Hennighausen L. The transcription factor Stat3 is dispensable for pancreatic beta-cell development and function. *Biochem Biophys Res Commun.* 2005;334(3):764-8.
58. Lefler JE, MarElia-Bennett CB, Thies KA, Hildreth BE, 3rd, Sharma SM, Pitarresi JR, et al. STAT3 in tumor fibroblasts promotes an immunosuppressive microenvironment in pancreatic cancer. *Life Sci Alliance.* 2022;5(11).
59. Shankar S, Suthakar G, and Srivastava RK. Epigallocatechin-3-gallate inhibits cell cycle and induces apoptosis in pancreatic cancer. *Front Biosci.* 2007;12:5039-51.
60. Carpenter ES, Elhossiny AM, Kadiyala P, Li J, McGue J, Griffith BD, et al. Analysis of donor pancreata defines the transcriptomic signature and microenvironment of early neoplastic lesions. *Cancer Discov.* 2023.
61. Walker AE. The Adult Pancreas in Trauma and Disease. *Acad Forensic Pathol.* 2018;8(2):192-218.
62. Morioka F, Tani N, Ikeda T, Hirokawa T, Ikeda K, Shida A, et al. Morphological and biochemical changes in the pancreas associated with acute systemic hypoxia. *Hum Cell.* 2021;34(2):400-18.
63. Cocariu EA, Mageriu V, Staniceanu F, Bastian A, Socoliuc C, and Zurac S. Correlations Between the Autolytic Changes and Postmortem Interval in Refrigerated Cadavers. *Rom J Intern Med.* 2016;54(2):105-12.
64. Shimizu M, Hayashi T, Saitoh Y, Ohta K, and Itoh H. Postmortem autolysis in the pancreas: multivariate statistical study. The influence of clinicopathological conditions. *Pancreas.* 1990;5(1):91-4.
65. Grant TJ, Hua K, and Singh A. Molecular Pathogenesis of Pancreatic Cancer. *Prog Mol Biol Transl Sci.* 2016;144:241-75.
66. Luchini C, Grillo F, Fassan M, Vanoli A, Capelli P, Paolino G, et al. Malignant epithelial/exocrine tumors of the pancreas. *Pathologica.* 2020;112(3):210-26.
67. Matthaei H, Schulick RD, Hruban RH, and Maitra A. Cystic precursors to invasive pancreatic cancer. *Nat Rev Gastroenterol Hepatol.* 2011;8(3):141-50.
68. Zamboni G, Hirabayashi K, Castelli P, and Lennon AM. Precancerous lesions of the pancreas. *Best Pract Res Clin Gastroenterol.* 2013;27(2):299-322.
69. Assarzadegan N, Babaniamansour S, and Shi J. Updates in the Diagnosis of Intraductal Neoplasms of the Pancreas. *Front Physiol.* 2022;13:856803.

70. Hruban RH, Takaori K, Klimstra DS, Adsay NV, Albores-Saavedra J, Biankin AV, et al. An illustrated consensus on the classification of pancreatic intraepithelial neoplasia and intraductal papillary mucinous neoplasms. *Am J Surg Pathol.* 2004;28(8):977-87.
71. Biankin AV, Kench JG, Biankin SA, Lee CS, Morey AL, Dijkman FP, et al. Pancreatic intraepithelial neoplasia in association with intraductal papillary mucinous neoplasms of the pancreas: implications for disease progression and recurrence. *Am J Surg Pathol.* 2004;28(9):1184-92.
72. Konstantinidis IT, Vinuela EF, Tang LH, Klimstra DS, D'Angelica MI, Dematteo RP, et al. Incidentally discovered pancreatic intraepithelial neoplasia: what is its clinical significance? *Ann Surg Oncol.* 2013;20(11):3643-7.
73. Yu DY, Yu YD, Kim WB, Han HJ, Choi SB, Kim DS, et al. Clinical significance of pancreatic intraepithelial neoplasia in resectable pancreatic cancer on survivals. *Ann Surg Treat Res.* 2018;94(5):247-53.
74. Matsuda Y, Furukawa T, Yachida S, Nishimura M, Seki A, Nonaka K, et al. The Prevalence and Clinicopathological Characteristics of High-Grade Pancreatic Intraepithelial Neoplasia: Autopsy Study Evaluating the Entire Pancreatic Parenchyma. *Pancreas.* 2017;46(5):658-64.
75. Longnecker DS, and Suriawinata AA. Incidence of Pancreatic Intraepithelial Neoplasia in an Autopsy Series. *Pancreas.* 2022;51(4):305-9.
76. Schwartz AM, and Henson DE. Familial and sporadic pancreatic carcinoma, epidemiologic concordance. *Am J Surg Pathol.* 2007;31(4):645-6.
77. Andea A, Sarkar F, and Adsay VN. Clinicopathological correlates of pancreatic intraepithelial neoplasia: a comparative analysis of 82 cases with and 152 cases without pancreatic ductal adenocarcinoma. *Mod Pathol.* 2003;16(10):996-1006.
78. Cubilla AL, and Fitzgerald PJ. Morphological lesions associated with human primary invasive nonendocrine pancreas cancer. *Cancer Res.* 1976;36(7 PT 2):2690-8.
79. Waddell N, Pajic M, Patch AM, Chang DK, Kassahn KS, Bailey P, et al. Whole genomes redefine the mutational landscape of pancreatic cancer. *Nature.* 2015;518(7540):495-501.
80. Biankin AV, Waddell N, Kassahn KS, Gingras MC, Muthuswamy LB, Johns AL, et al. Pancreatic cancer genomes reveal aberrations in axon guidance pathway genes. *Nature.* 2012;491(7424):399-405.
81. Jones S, Zhang X, Parsons DW, Lin JC, Leary RJ, Angenendt P, et al. Core signaling pathways in human pancreatic cancers revealed by global genomic analyses. *Science.* 2008;321(5897):1801-6.
82. Yachida S, Jones S, Bozic I, Antal T, Leary R, Fu B, et al. Distant metastasis occurs late during the genetic evolution of pancreatic cancer. *Nature.* 2010;467(7319):1114-7.
83. Balachandran VP, Luksza M, Zhao JN, Makarov V, Moral JA, Remark R, et al. Identification of unique neoantigen qualities in long-term survivors of pancreatic cancer. *Nature.* 2017;551(7681):512-6.
84. Clark CE, Hingorani SR, Mick R, Combs C, Tuveson DA, and Vonderheide RH. Dynamics of the immune reaction to pancreatic cancer from inception to invasion. *Cancer Res.* 2007;67(19):9518-27.
85. Feldmann G, Beaty R, Hruban RH, and Maitra A. Molecular genetics of pancreatic intraepithelial neoplasia. *J Hepatobiliary Pancreat Surg.* 2007;14(3):224-32.
86. Yanagisawa A, Ohtake K, Ohashi K, Hori M, Kitagawa T, Sugano H, and Kato Y. Frequent c-Ki-ras oncogene activation in mucous cell hyperplasias of pancreas suffering from chronic inflammation. *Cancer Res.* 1993;53(5):953-6.
87. Terhune PG, Phifer DM, Tosteson TD, and Longnecker DS. K-ras mutation in focal proliferative lesions of human pancreas. *Cancer Epidemiol Biomarkers Prev.* 1998;7(6):515-21.

88. Heinmoller E, Dietmaier W, Zirngibl H, Heinmoller P, Scaringe W, Jauch KW, et al. Molecular analysis of microdissected tumors and preneoplastic intraductal lesions in pancreatic carcinoma. *Am J Pathol.* 2000;157(1):83-92.
89. Wilentz RE, Iacobuzio-Donahue CA, Argani P, McCarthy DM, Parsons JL, Yeo CJ, et al. Loss of expression of Dpc4 in pancreatic intraepithelial neoplasia: evidence that DPC4 inactivation occurs late in neoplastic progression. *Cancer Res.* 2000;60(7):2002-6.
90. Collins MA, Yan W, Sebolt-Leopold JS, and Pasca di Magliano M. MAPK signaling is required for dedifferentiation of acinar cells and development of pancreatic intraepithelial neoplasia in mice. *Gastroenterology.* 2014;146(3):822-34.e7.
91. Hingorani SR, Petricoin EF, Maitra A, Rajapakse V, King C, Jacobetz MA, et al. Preinvasive and invasive ductal pancreatic cancer and its early detection in the mouse. *Cancer Cell.* 2003;4(6):437-50.
92. Hingorani SR, Wang L, Multani AS, Combs C, Deramaudt TB, Hruban RH, et al. Trp53R172H and KrasG12D cooperate to promote chromosomal instability and widely metastatic pancreatic ductal adenocarcinoma in mice. *Cancer Cell.* 2005;7(5):469-83.
93. Collins MA, Bednar F, Zhang Y, Brisset JC, Galban S, Galban CJ, et al. Oncogenic Kras is required for both the initiation and maintenance of pancreatic cancer in mice. *J Clin Invest.* 2012;122(2):639-53.
94. Buechler MB, Pradhan RN, Krishnamurty AT, Cox C, Calviello AK, Wang AW, et al. Cross-tissue organization of the fibroblast lineage. *Nature.* 2021;593(7860):575-9.
95. Dominguez CX, Muller S, Keerthivasan S, Koeppen H, Hung J, Gierke S, et al. Single-Cell RNA Sequencing Reveals Stromal Evolution into LRRC15(+) Myofibroblasts as a Determinant of Patient Response to Cancer Immunotherapy. *Cancer Discov.* 2020;10(2):232-53.
96. Helms EJ, Berry MW, Chaw RC, DuFort CC, Sun D, Onate MK, et al. Mesenchymal Lineage Heterogeneity Underlies Nonredundant Functions of Pancreatic Cancer-Associated Fibroblasts. *Cancer Discov.* 2022;12(2):484-501.
97. Hosein AN, Huang H, Wang Z, Parmar K, Du W, Huang J, et al. Cellular heterogeneity during mouse pancreatic ductal adenocarcinoma progression at single-cell resolution. *JCI Insight.* 2019;5(16).
98. Steele NG, Carpenter ES, Kemp SB, Sirihorachai VR, The S, Delrosario L, et al. Multimodal mapping of the tumor and peripheral blood immune landscape in human pancreatic cancer. *Nature Cancer.* 2020;1(11):1097-112.
99. Dann E, Henderson NC, Teichmann SA, Morgan MD, and Marioni JC. Differential abundance testing on single-cell data using k-nearest neighbor graphs. *Nat Biotechnol.* 2022;40(2):245-53.
100. Ramilowski JA, Goldberg T, Harshbarger J, Kloppmann E, Lizio M, Satagopam VP, et al. A draft network of ligand-receptor-mediated multicellular signalling in human. *Nat Commun.* 2015;6:7866.
101. Ardito CM, Gruner BM, Takeuchi KK, Lubeseder-Martellato C, Teichmann N, Mazur PK, et al. EGF receptor is required for KRAS-induced pancreatic tumorigenesis. *Cancer Cell.* 2012;22(3):304-17.
102. Navas C, Hernandez-Porras I, Schuhmacher AJ, Sibilia M, Guerra C, and Barbacid M. EGF receptor signaling is essential for k-ras oncogene-driven pancreatic ductal adenocarcinoma. *Cancer Cell.* 2012;22(3):318-30.
103. Djurec M, Grana O, Lee A, Troule K, Espinet E, Cabras L, et al. Saa3 is a key mediator of the protumorigenic properties of cancer-associated fibroblasts in pancreatic tumors. *Proc Natl Acad Sci U S A.* 2018;115(6):E1147-E56.
104. Hingorani SR. Epithelial and stromal co-evolution and complicity in pancreatic cancer. *Nat Rev Cancer.* 2023;23(2):57-77.

105. Nywening TM, Belt BA, Cullinan DR, Panni RZ, Han BJ, Sanford DE, et al. Targeting both tumour-associated CXCR2(+) neutrophils and CCR2(+) macrophages disrupts myeloid recruitment and improves chemotherapeutic responses in pancreatic ductal adenocarcinoma. *Gut.* 2018;67(6):1112-23.
106. DeNardo DG, and Ruffell B. Macrophages as regulators of tumour immunity and immunotherapy. *Nat Rev Immunol.* 2019;19(6):369-82.
107. Kemp SB, Steele NG, Carpenter ES, Donahue KL, Bushnell GG, Morris AH, et al. Pancreatic cancer is marked by complement-high blood monocytes and tumor-associated macrophages. *Life Sci Alliance.* 2021;4(6).
108. Kemp SB, Carpenter ES, Steele NG, Donahue KL, Nwosu ZC, Pacheco A, et al. Apolipoprotein E Promotes Immune Suppression in Pancreatic Cancer through NF-kappaB-Mediated Production of CXCL1. *Cancer Res.* 2021;81(16):4305-18.
109. Yang X, Lin Y, Shi Y, Li B, Liu W, Yin W, et al. FAP Promotes Immunosuppression by Cancer-Associated Fibroblasts in the Tumor Microenvironment via STAT3-CCL2 Signaling. *Cancer Res.* 2016;76(14):4124-35.
110. Sivakumar S, Abu-Shah E, Ahern DJ, Arbe-Barnes EH, Jainarayanan AK, Mangal N, et al. Activated Regulatory T-Cells, Dysfunctional and Senescent T-Cells Hinder the Immunity in Pancreatic Cancer. *Cancers (Basel).* 2021;13(8).
111. Bresnick AR, Weber DJ, and Zimmer DB. S100 proteins in cancer. *Nat Rev Cancer.* 2015;15(2):96-109.
112. Simeonov KP, Byrns CN, Clark ML, Norgard RJ, Martin B, Stanger BZ, et al. Single-cell lineage tracing of metastatic cancer reveals selection of hybrid EMT states. *Cancer Cell.* 2021;39(8):1150-62 e9.
113. Cui Zhou D, Jayasinghe RG, Chen S, Herndon JM, Iglesia MD, Navale P, et al. Spatially restricted drivers and transitional cell populations cooperate with the microenvironment in untreated and chemo-resistant pancreatic cancer. *Nat Genet.* 2022;54(9):1390-405.
114. Liberzon A, Birger C, Thorvaldsdottir H, Ghandi M, Mesirov JP, and Tamayo P. The Molecular Signatures Database (MSigDB) hallmark gene set collection. *Cell Syst.* 2015;1(6):417-25.
115. Arsenijevic T, Perret J, Van Laethem JL, and Delporte C. Aquaporins Involvement in Pancreas Physiology and in Pancreatic Diseases. *Int J Mol Sci.* 2019;20(20).
116. Balague C, Gambus G, Carrato C, Porchet N, Aubert JP, Kim YS, and Real FX. Altered expression of MUC2, MUC4, and MUC5 mucin genes in pancreas tissues and cancer cell lines. *Gastroenterology.* 1994;106(4):1054-61.
117. Tanaka M, Shibahara J, Fukushima N, Shinozaki A, Umeda M, Ishikawa S, et al. Claudin-18 is an early-stage marker of pancreatic carcinogenesis. *J Histochem Cytochem.* 2011;59(10):942-52.
118. Arumugam T, Brandt W, Ramachandran V, Moore TT, Wang H, May FE, et al. Trefoil factor 1 stimulates both pancreatic cancer and stellate cells and increases metastasis. *Pancreas.* 2011;40(6):815-22.
119. Guppy NJ, El-Bahrawy ME, Kocher HM, Fritsch K, Qureshi YA, Poulsom R, et al. Trefoil factor family peptides in normal and diseased human pancreas. *Pancreas.* 2012;41(6):888-96.
120. Kim GE, Bae HI, Park HU, Kuan SF, Crawley SC, Ho JJ, and Kim YS. Aberrant expression of MUC5AC and MUC6 gastric mucins and sialyl Tn antigen in intraepithelial neoplasms of the pancreas. *Gastroenterology.* 2002;123(4):1052-60.
121. Beinrohr L, Murray-Rust TA, Dyksterhuis L, Zavodszky P, Gal P, Pike RN, and Wijeyewickrema LC. Serpins and the complement system. *Methods Enzymol.* 2011;499:55-75.
122. Suzuki R, Okubo Y, Takagi T, Sugimoto M, Sato Y, Irie H, et al. The Complement C3a-C3a Receptor Axis Regulates Epithelial-to-Mesenchymal Transition by Activating the

ERK Pathway in Pancreatic Ductal Adenocarcinoma. *Anticancer Res.* 2022;42(3):1207-15.
123. Kemp SB, Steele NG, Carpenter ES, Donahue KL, Bushnell GG, Morris AH, et al. Pancreatic cancer is marked by complement-high blood monocytes and tumor-associated macrophages. *Life Sci Alliance.* 2021;4(6):e202000935.
124. Moffitt RA, Marayati R, Flate EL, Volmar KE, Loeza SG, Hoadley KA, et al. Virtual microdissection identifies distinct tumor- and stroma-specific subtypes of pancreatic ductal adenocarcinoma. *Nat Genet.* 2015;47(10):1168-78.
125. Bailey P, Chang DK, Nones K, Johns AL, Patch AM, Gingras MC, et al. Genomic analyses identify molecular subtypes of pancreatic cancer. *Nature.* 2016;531(7592):47-52.
126. Collisson EA, Sadanandam A, Olson P, Gibb WJ, Truitt M, Gu S, et al. Subtypes of pancreatic ductal adenocarcinoma and their differing responses to therapy. *Nat Med.* 2011;17(4):500-3.
127. Juiz N, Elkaoutari A, Bigonnet M, Gayet O, Roques J, Nicolle R, et al. Basal-like and classical cells coexist in pancreatic cancer revealed by single-cell analysis on biopsy-derived pancreatic cancer organoids from the classical subtype. *FASEB J.* 2020;34(9):12214-28.
128. Kanda M, Matthaei H, Wu J, Hong SM, Yu J, Borges M, et al. Presence of somatic mutations in most early-stage pancreatic intraepithelial neoplasia. *Gastroenterology.* 2012;142(4):730-3 e9.
129. Tabula Sapiens C, Jones RC, Karkanias J, Krasnow MA, Pisco AO, Quake SR, et al. The Tabula Sapiens: A multiple-organ, single-cell transcriptomic atlas of humans. *Science.* 2022;376(6594):eabl4896.
130. Enge M, Arda HE, Mignardi M, Beausang J, Bottino R, Kim SK, and Quake SR. Single-Cell Analysis of Human Pancreas Reveals Transcriptional Signatures of Aging and Somatic Mutation Patterns. *Cell.* 2017;171(2):321-30 e14.
131. Olaniru OE, Kadolsky U, Kannambath S, Vaikkinen H, Fung K, Dhami P, and Persaud SJ. Single-cell transcriptomic and spatial landscapes of the developing human pancreas. *Cell Metab.* 2023;35(1):184-99 e5.
132. Lohr M, Kloppel G, Maisonneuve P, Lowenfels AB, and Luttges J. Frequency of K-ras mutations in pancreatic intraductal neoplasias associated with pancreatic ductal adenocarcinoma and chronic pancreatitis: a meta-analysis. *Neoplasia.* 2005;7(1):17-23.
133. Freed-Pastor WA, Lambert LJ, Ely ZA, Pattada NB, Bhutkar A, Eng G, et al. The CD155/TIGIT axis promotes and maintains immune evasion in neoantigen-expressing pancreatic cancer. *Cancer Cell.* 2021;39(10):1342-60 e14.
134. Kopp JL, von Figura G, Mayes E, Liu FF, Dubois CL, Morris JPt, et al. Identification of Sox9-dependent acinar-to-ductal reprogramming as the principal mechanism for initiation of pancreatic ductal adenocarcinoma. *Cancer Cell.* 2012;22(6):737-50.
135. Kopp JL, Dubois CL, Schaeffer DF, Samani A, Taghizadeh F, Cowan RW, et al. Loss of Pten and Activation of Kras Synergistically Induce Formation of Intraductal Papillary Mucinous Neoplasia From Pancreatic Ductal Cells in Mice. *Gastroenterology.* 2018;154(5):1509-23 e5.
136. Bailey JM, Hendley AM, Lafaro KJ, Pruski MA, Jones NC, Alsina J, et al. p53 mutations cooperate with oncogenic Kras to promote adenocarcinoma from pancreatic ductal cells. *Oncogene.* 2016;35(32):4282-8.
137. Strobel O, Rosow DE, Rakhlin EY, Lauwers GY, Trainor AG, Alsina J, et al. Pancreatic duct glands are distinct ductal compartments that react to chronic injury and mediate Shh-induced metaplasia. *Gastroenterology.* 2010;138(3):1166-77.

138. Hruban RH, Adsay NV, Albores-Saavedra J, Compton C, Garrett ES, Goodman SN, et al. Pancreatic intraepithelial neoplasia: a new nomenclature and classification system for pancreatic duct lesions. *Am J Surg Pathol.* 2001;25(5):579-86.
139. Hruban RH, Goggins M, Parsons J, and Kern SE. Progression model for pancreatic cancer. *Clin Cancer Res.* 2000;6(8):2969-72.
140. Lee AYL, Dubois CL, Sarai K, Zarei S, Schaeffer DF, Sander M, and Kopp JL. Cell of origin affects tumour development and phenotype in pancreatic ductal adenocarcinoma. *Gut.* 2019;68(3):487-98.
141. Singh K, Pruski M, Bland R, Younes M, Guha S, Thosani N, et al. Kras mutation rate precisely orchestrates ductal derived pancreatic intraepithelial neoplasia and pancreatic cancer. *Lab Invest.* 2021;101(2):177-92.
142. Rhim AD, Oberstein PE, Thomas DH, Mirek ET, Palermo CF, Sastra SA, et al. Stromal elements act to restrain, rather than support, pancreatic ductal adenocarcinoma. *Cancer Cell.* 2014;25(6):735-47.
143. Francescone R, Barbosa Vendramini-Costa D, Franco-Barraza J, Wagner J, Muir A, Lau AN, et al. Netrin G1 Promotes Pancreatic Tumorigenesis through Cancer-Associated Fibroblast-Driven Nutritional Support and Immunosuppression. *Cancer Discov.* 2021;11(2):446-79.
144. Krishnamurty AT, Shyer JA, Thai M, Gandham V, Buechler MB, Yang YA, et al. LRRC15(+) myofibroblasts dictate the stromal setpoint to suppress tumour immunity. *Nature.* 2022;611(7934):148-54.
145. Hingorani SR. Epithelial and stromal co-evolution and complicity in pancreatic cancer. *Nat Rev Cancer.* 2022.
146. Krendl FJ, Messner F, Bosmuller C, Scheidl S, Cardini B, Resch T, et al. Post-Transplant Malignancies following Pancreas Transplantation: Incidence and Implications on Long-Term Outcome from a Single-Center Perspective. *J Clin Med.* 2021;10(21).
147. Young MD, and Behjati S. SoupX removes ambient RNA contamination from droplet-based single-cell RNA sequencing data. *Gigascience.* 2020;9(12).
148. Hao Y, Hao S, Andersen-Nissen E, Mauck WM, 3rd, Zheng S, Butler A, et al. Integrated analysis of multimodal single-cell data. *Cell.* 2021;184(13):3573-87 e29.
149. Jin S, Guerrero-Juarez CF, Zhang L, Chang I, Ramos R, Kuan CH, et al. Inference and analysis of cell-cell communication using CellChat. *Nat Commun.* 2021;12(1):1088.
150. Yu G, Wang LG, Han Y, and He QY. clusterProfiler: an R package for comparing biological themes among gene clusters. *OMICS.* 2012;16(5):284-7.
151. Aibar S, Gonzalez-Blas CB, Moerman T, Huynh-Thu VA, Imrichova H, Hulselmans G, et al. SCENIC: single-cell regulatory network inference and clustering. *Nat Methods.* 2017;14(11):1083-6.
152. Liberzon A, Subramanian A, Pinchback R, Thorvaldsdottir H, Tamayo P, and Mesirov JP. Molecular signatures database (MSigDB) 3.0. *Bioinformatics.* 2011;27(12):1739-40.
153. Ritchie ME, Phipson B, Wu D, Hu Y, Law CW, Shi W, and Smyth GK. limma powers differential expression analyses for RNA-sequencing and microarray studies. *Nucleic Acids Res.* 2015;43(7):e47.
154. Hanzelmann S, Castelo R, and Guinney J. GSVA: gene set variation analysis for microarray and RNA-seq data. *BMC Bioinformatics.* 2013;14:7.
155. Huo G, Liu W, Zhang S, and Chen P. Efficacy of PD-1/PD-L1 plus CTLA-4 inhibitors in solid tumors based on clinical characteristics: a meta-analysis. *Immunotherapy.* 2023;15(3):189-207.
156. Martinez P, Peters S, Stammers T, and Soria JC. Immunotherapy for the First-Line Treatment of Patients with Metastatic Non-Small Cell Lung Cancer. *Clin Cancer Res.* 2019;25(9):2691-8.

157. Labriola MK, Batich KA, Zhu J, McNamara MA, Harrison MR, Armstrong AJ, et al. Immunotherapy Is Changing First-Line Treatment of Metastatic Renal-Cell Carcinoma. *Clin Genitourin Cancer.* 2019;17(3):e513-e21.
158. Neoptolemos JP, Kleeff J, Michl P, Costello E, Greenhalf W, and Palmer DH. Therapeutic developments in pancreatic cancer: current and future perspectives. *Nat Rev Gastroenterol Hepatol.* 2018;15(6):333-48.
159. Balachandran VP, Beatty GL, and Dougan SK. Broadening the Impact of Immunotherapy to Pancreatic Cancer: Challenges and Opportunities. *Gastroenterology.* 2019;156(7):2056-72.
160. Liou GY, Döppler H, Necela B, Edenfield B, Zhang L, Dawson DW, and Storz P. Mutant KRAS-induced expression of ICAM-1 in pancreatic acinar cells causes attraction of macrophages to expedite the formation of precancerous lesions. *Cancer Discov.* 2015;5(1):52-63.
161. Stromnes IM, Brockenbrough JS, Izeradjene K, Carlson MA, Cuevas C, Simmons RM, et al. Targeted depletion of an MDSC subset unmasks pancreatic ductal adenocarcinoma to adaptive immunity. *Gut.* 2014.
162. Zhu Y, Knolhoff BL, Meyer MA, Nywening TM, West BL, Luo J, et al. CSF1/CSF1R Blockade Reprograms Tumor-Infiltrating Macrophages and Improves Response to T-cell Checkpoint Immunotherapy in Pancreatic Cancer Models. *Cancer Res.* 2014.
163. Zhu Y, Herndon JM, Sojka DK, Kim KW, Knolhoff BL, Zuo C, et al. Tissue-Resident Macrophages in Pancreatic Ductal Adenocarcinoma Originate from Embryonic Hematopoiesis and Promote Tumor Progression. *Immunity.* 2017;47(2):323-38 e6.
164. Mitchem JB, Brennan DJ, Knolhoff BL, Belt BA, Zhu Y, Sanford DE, et al. Targeting tumor-infiltrating macrophages decreases tumor-initiating cells, relieves immunosuppression, and improves chemotherapeutic responses. *Cancer Res.* 2013;73(3):1128-41.
165. Liu X, Hogg GD, Zuo C, Borcherding NC, Baer JM, Lander VE, et al. Context-dependent activation of STING-interferon signaling by CD11b agonists enhances anti-tumor immunity. *Cancer Cell.* 2023;41(6):1073-90 e12.
166. Steele CW, Karim SA, Leach JD, Bailey P, Upstill-Goddard R, Rishi L, et al. CXCR2 Inhibition Profoundly Suppresses Metastases and Augments Immunotherapy in Pancreatic Ductal Adenocarcinoma. *Cancer Cell.* 2016;29(6):832-45.
167. Stromnes IM, Burrack AL, Hulbert A, Bonson P, Black C, Brockenbrough JS, et al. Differential Effects of Depleting versus Programming Tumor-Associated Macrophages on Engineered T Cells in Pancreatic Ductal Adenocarcinoma. *Cancer Immunol Res.* 2019;7(6):977-89.
168. Beatty GL, Winograd R, Evans RA, Long KB, Luque SL, Lee JW, et al. Exclusion of T Cells From Pancreatic Carcinomas in Mice Is Regulated by Ly6C(low) F4/80(+) Extratumoral Macrophages. *Gastroenterology.* 2015;149(1):201-10.
169. Beatty GL, Chiorean EG, Fishman MP, Saboury B, Teitelbaum UR, Sun W, et al. CD40 agonists alter tumor stroma and show efficacy against pancreatic carcinoma in mice and humans. *Science.* 2011;331(6024):1612-6.
170. Bayne LJ, Beatty GL, Jhala N, Clark CE, Rhim AD, Stanger BZ, and Vonderheide RH. Tumor-derived granulocyte-macrophage colony-stimulating factor regulates myeloid inflammation and T cell immunity in pancreatic cancer. *Cancer Cell.* 2012;21(6):822-35.
171. Dixit A, Sarver A, Zettervall J, Huang H, Zheng K, Brekken RA, and Provenzano PP. Targeting TNF-alpha-producing macrophages activates antitumor immunity in pancreatic cancer via IL-33 signaling. *JCI Insight.* 2022;7(22).
172. Pandey V, and Storz P. Targeting the tumor microenvironment in pancreatic ductal adenocarcinoma. *Expert Rev Anticancer Ther.* 2019;19(6):473-82.

173. Bastea LI, Liou GY, Pandey V, Fleming AK, von Roemeling CA, Doeppler H, et al. Pomalidomide Alters Pancreatic Macrophage Populations to Generate an Immune-Responsive Environment at Precancerous and Cancerous Lesions. *Cancer Res.* 2019;79(7):1535-48.
174. Bar-Natan M, Nelson EA, Xiang M, and Frank DA. STAT signaling in the pathogenesis and treatment of myeloid malignancies. *Jakstat.* 2012;1(2):55-64.
175. Wang N, Liang H, and Zen K. Molecular mechanisms that influence the macrophage m1-m2 polarization balance. *Front Immunol.* 2014;5:614.
176. Kujawski M, Kortylewski M, Lee H, Herrmann A, Kay H, and Yu H. Stat3 mediates myeloid cell-dependent tumor angiogenesis in mice. *J Clin Invest.* 2008;118(10):3367-77.
177. Kortylewski M, Kujawski M, Wang T, Wei S, Zhang S, Pilon-Thomas S, et al. Inhibiting Stat3 signaling in the hematopoietic system elicits multicomponent antitumor immunity. *Nat Med.* 2005;11(12):1314-21.
178. Irey EA, Lassiter CM, Brady NJ, Chuntova P, Wang Y, Knutson TP, et al. JAK/STAT inhibition in macrophages promotes therapeutic resistance by inducing expression of protumorigenic factors. *Proc Natl Acad Sci U S A.* 2019;116(25):12442-51.
179. Deng L, Zhou JF, Sellers RS, Li JF, Nguyen AV, Wang Y, et al. A novel mouse model of inflammatory bowel disease links mammalian target of rapamycin-dependent hyperproliferation of colonic epithelium to inflammation-associated tumorigenesis. *Am J Pathol.* 2010;176(2):952-67.
180. Peisl S, Mellenthin C, Vignot L, Gonelle-Gispert C, Bühler L, and Egger B. Therapeutic targeting of STAT3 pathways in pancreatic adenocarcinoma: A systematic review of clinical and preclinical literature. *PLoS One.* 2021;16(6):e0252397.
181. Menjivar RE, Nwosu ZC, Du W, Donahue KL, Hong HS, Espinoza C, et al. Arginase 1 is a key driver of immune suppression in pancreatic cancer. *Elife.* 2023;12.
182. Carpenter ES, Elhossiny AM, Kadiyala P, Li J, McGue J, Griffith BD, et al. Analysis of Donor Pancreata Defines the Transcriptomic Signature and Microenvironment of Early Neoplastic Lesions. *Cancer Discov.* 2023;13(6):1324-45.
183. Du W, Menjivar RE, Donahue KL, Kadiyala P, Velez-Delgado A, Brown KL, et al. WNT signaling in the tumor microenvironment promotes immunosuppression in murine pancreatic cancer. *J Exp Med.* 2023;220(1).
184. Storz P. Acinar cell plasticity and development of pancreatic ductal adenocarcinoma. *Nat Rev Gastroenterol Hepatol.* 2017;14(5):296-304.
185. Stone ML, and Beatty GL. Cellular determinants and therapeutic implications of inflammation in pancreatic cancer. *Pharmacol Ther.* 2019;201:202-13.
186. Overbeek KA, Cahen DL, Canto MI, and Bruno MJ. Surveillance for neoplasia in the pancreas. *Best Pract Res Clin Gastroenterol.* 2016;30(6):971-86.
187. Sica A, and Mantovani A. Macrophage plasticity and polarization: in vivo veritas. *J Clin Invest.* 2012;122(3):787-95.
188. Yan D, Wang HW, Bowman RL, and Joyce JA. STAT3 and STAT6 Signaling Pathways Synergize to Promote Cathepsin Secretion from Macrophages via IRE1α Activation. *Cell Rep.* 2016;16(11):2914-27.
189. Zhou J, Qu Z, Sun F, Han L, Li L, Yan S, et al. Myeloid STAT3 Promotes Lung Tumorigenesis by Transforming Tumor Immunosurveillance into Tumor-Promoting Inflammation. *Cancer Immunol Res.* 2017;5(3):257-68.
190. Pathria P, Gotthardt D, Prchal-Murphy M, Putz EM, Holcmann M, Schlederer M, et al. Myeloid STAT3 promotes formation of colitis-associated colorectal cancer in mice. *Oncoimmunology.* 2015;4(4):e998529.
191. Yu H, Pardoll D, and Jove R. STATs in cancer inflammation and immunity: a leading role for STAT3. *Nat Rev Cancer.* 2009;9(11):798-809.

192. Royal RE, Levy C, Turner K, Mathur A, Hughes M, Kammula US, et al. Phase 2 trial of single agent Ipilimumab (anti-CTLA-4) for locally advanced or metastatic pancreatic adenocarcinoma. *J Immunother.* 2010;33(8):828-33.
193. Brahmer JR, Tykodi SS, Chow LQ, Hwu WJ, Topalian SL, Hwu P, et al. Safety and activity of anti-PD-L1 antibody in patients with advanced cancer. *N Engl J Med.* 2012;366(26):2455-65.
194. Zhang Y, Yan W, Mathew E, Bednar F, Wan S, Collins MA, et al. CD4+ T lymphocyte ablation prevents pancreatic carcinogenesis in mice. *Cancer Immunol Res.* 2014;2(5):423-35.
195. Schizas D, Charalampakis N, Kole C, Economopoulou P, Koustas E, Gkotsis E, et al. Immunotherapy for pancreatic cancer: A 2020 update. *Cancer Treat Rev.* 2020;86:102016.
196. Blando J, Sharma A, Higa MG, Zhao H, Vence L, Yadav SS, et al. Comparison of immune infiltrates in melanoma and pancreatic cancer highlights VISTA as a potential target in pancreatic cancer. *Proc Natl Acad Sci U S A.* 2019;116(5):1692-7.
197. Li J, Tan J, Martino MM, and Lui KO. Regulatory T-Cells: Potential Regulator of Tissue Repair and Regeneration. *Front Immunol.* 2018;9:585.
198. Tang Y, Xu X, Guo S, Zhang C, Tang Y, Tian Y, et al. An increased abundance of tumor-infiltrating regulatory T cells is correlated with the progression and prognosis of pancreatic ductal adenocarcinoma. *PLoS One.* 2014;9(3):e91551.
199. Tassi E, Gavazzi F, Albarello L, Senyukov V, Longhi R, Dellabona P, et al. Carcinoembryonic antigen-specific but not antiviral CD4+ T cell immunity is impaired in pancreatic carcinoma patients. *J Immunol.* 2008;181(9):6595-603.
200. DeNardo DG, Barreto JB, Andreu P, Vasquez L, Tawfik D, Kolhatkar N, and Coussens LM. CD4(+) T cells regulate pulmonary metastasis of mammary carcinomas by enhancing protumor properties of macrophages. *Cancer Cell.* 2009;16(2):91-102.
201. Dey P, Li J, Zhang J, Chaurasiya S, Strom A, Wang H, et al. Oncogenic KRAS-Driven Metabolic Reprogramming in Pancreatic Cancer Cells Utilizes Cytokines from the Tumor Microenvironment. *Cancer Discov.* 2020;10(4):608-25.
202. Carrière C, Young AL, Gunn JR, Longnecker DS, and Korc M. Acute pancreatitis markedly accelerates pancreatic cancer progression in mice expressing oncogenic Kras. *Biochem Biophys Res Commun.* 2009;382(3):561-5.
203. Sherman MH, and Beatty GL. Tumor Microenvironment in Pancreatic Cancer Pathogenesis and Therapeutic Resistance. *Annu Rev Pathol.* 2023;18:123-48.
204. Glaubitz J, Wilden A, Golchert J, Homuth G, Völker U, Bröker BM, et al. In mouse chronic pancreatitis CD25(+)FOXP3(+) regulatory T cells control pancreatic fibrosis by suppression of the type 2 immune response. *Nat Commun.* 2022;13(1):4502.
205. Kobayashi M, Kweon MN, Kuwata H, Schreiber RD, Kiyono H, Takeda K, and Akira S. Toll-like receptor-dependent production of IL-12p40 causes chronic enterocolitis in myeloid cell-specific Stat3-deficient mice. *J Clin Invest.* 2003;111(9):1297-308.
206. Prokopchuk O, Liu Y, Henne-Bruns D, and Kornmann M. Interleukin-4 enhances proliferation of human pancreatic cancer cells: evidence for autocrine and paracrine actions. *Br J Cancer.* 2005;92(5):921-8.